UNIVERSITY OF CALIFORNIA, SAN DIEGO

Tidal interactions with topography: the effects of latitude and tidal constitution on nearfield mixing

A dissertation submitted in partial satisfaction of the
requirements for the degree
Doctor of Philosophy

in

Oceanography

by

Ruth Claire Musgrave

Committee in charge:

Jennifer MacKinnon, Co-Chair
Robert Pinkel, Co-Chair
Peter Franks
Matthew Mazloff
Geno Pawlak
William R. Young

2015

The dissertation of Ruth Claire Musgrave is approved, and it is acceptable in quality and form for publication on microfilm and electronically:

_____

_____

_____

_____

_____
Co-Chair

_____
Co-Chair

University of California, San Diego

2015

TABLE OF CONTENTS

LIST OF FIGURES

LIST OF TABLES

LIST OF SUPPLEMENTARY MATERIAL

ACKNOWLEDGEMENTS

First and foremost I would like to thank my advisors, Jen and Rob, for their amazing guidance and help during my Ph.D. They have taught me how to be a scientist, spending countless hours with me talking about my research, and providing invaluable feedback on my work. Their encouragement, support and excellent advising throughout my graduate career has enabled me to complete this dissertation, and I cannot thank them enough.

I could not have asked for more in my committee, and gratefully acknowledge their input into this dissertation. Matthew Mazloff, for the late night email responses with gems of MITgcm knowledge - they have saved me countless times; Peter Franks, for broadening my scientific knowledge by including me in his weekly lab discussions, and encouraging me so wholeheartedly; Bill Young, for his unending patience teaching me theory; and Geno Pawlak, for his interest and constructive input into my work.

I have had the privilege of interacting with some truly wonderful scientists over the course of my studies. In particular, Myrl Hendershott has been unendingly supportive, and is truly a font of scientific wisdom. Jonathan Nash at OSU has been a source of encouragement and fun throughout my Ph.D., and his contribution to the cruise upon which much of this dissertation is based was invaluable. He is an excellent collaborator, and I am lucky to have had his interest and input.

I want to take this opportunity to thank the teachers and mentors who helped me along my way. Matthew Bailes for giving me a job as an undergraduate that meant I could stop working the physically challenging hotel/coffee shop/pub combination, and instead be intellectually challenged by a Linux workstation. Louis Moresi for guiding me into geosciences, and keeping me employed in academia while I studied for my Honours part time. Simon Clarke and Michael Reeder for getting me into atmospheric science, and inspiring a love of rotating fluid mechanics. Each one of these people has made a substantial contribution to my career, and I wouldn't be here without them.

I am honored to be one of the incoming P.O. class of 2009. Roy Barkan, Sam Billheimer, Magdalena Carranza, Andrew Delman, Kai Hally-Rosendahl, Bonnie

Ludka, Nick Pizzo, Caitlin Whalen and Uriel Zajaczkovski, these guys are the best. I have learned so much from them, about science and everything else.

Thanks to my patient office mates over the years. Roy Barkan, Martha Schnoau, Catherine Jones and Myla. With the exception of Myla, who is excused on account of being a dog, they have been first to hand to bemoan the various injustices of graduate school with me, and figure out whether I am being stupid, or if I am stuck on a genuinely difficult problem. Thanks to them, they have made this process so much easier.

A particular thanks to my co-chief-scientist, Amy Waterhouse. It was Amy who suggested that we should write the ship funds proposal, the data from which has ended up constituting two thirds of this dissertation. Amy's experience, enthusiasm and ability to bring people together was a huge factor in making the cruise so successful.

One of the most enjoyable aspects of my graduate studies has been going to sea. Mike Goldin, Tyler Huyghen, Tony Aja, Drew Lucas, Jonathan Ladner, San Nguyen and Amy Waterhouse are awesome ship mates. I hope to spend many more days at sea with them.

Thanks to UC Ship Funds for giving Amy and I the opportunity to design our own experiment and go to sea. As junior scientists, this was a hugely valuable experience. Thanks also to the various people from whom we scrounged instrumentation: Shaun Johnston, Uwe Send and Janet Sprintall. Our experiment would not have been the same without their generosity. Thank you to Paul Chua, who worked long hours designing and preparing the moorings and instruments for us, and was responsible for the smooth-running of our at-sea operations.

Thanks to my parents and grandmother, who are a source of constant support to me. From the earliest age they have encouraged me to explore the world around me, and work hard to achieve my best.

Finally, a special thanks to Uri. He has been the highlight of my time here, and his love and support means everything to me.

Chapter 2, in full, has been submitted for publication of the material as it may appear in the Journal of Physical Oceanography, 2015, Musgrave, R C; MacKinnon, J A; Pinkel, R; Waterhouse, A F; Nash, J. The dissertation author was the primary investigator and author of this paper.

Chapter 3 is currently being prepared for submission for publication of the material to the Journal of Physical Oceanography, Musgrave, R C; MacKinnon, J A; Pinkel, R; Waterhouse, A F; Nash, J; Kelly, S. The dissertation author was the primary investigator and author of this paper.

Chapter 4, in full, has been submitted for publication of the material as it may appear in the Journal of Fluid Mechanics, 2015, Musgrave, R C; Pinkel, R; MacKinnon, J A; Mazloff, M; Young, W R. The dissertation author was the primary investigator and author of this paper.

VITA

2005	Bachelor of Science (Physics), Melbourne University, Melbourne, Australia
2010	Honours (Applied Mathematics - Atmospheric Science), Monash University, Melbourne, Australia
2015	Doctor of Philosophy (Oceanography), University of California, San Diego

PUBLICATIONS

R. C. Musgrave; J. MacKinnon; R. Pinkel; A. Waterhouse; J. Nash; S. Kelly. *The influence of trapped internal tides on tidally driven turbulence at the Mendocino Ridge. In prep. for Journal of Physical Oceanography.*

R. C. Musgrave; R. Pinkel; J. MacKinnon; M. Mazloff; W. R. Young. *Stratified tidal flow over a tall Gaussian ridge above and below the turning latitude. Under review for Journal of Fluid Mechanics.*

R. C. Musgrave; J. MacKinnon; R. Pinkel; A. Waterhouse; J. Nash. *Tidally driven processes leading to nearfield turbulence in a channel at the crest of the Mendocino Escarpment. Under review for Journal of Physical Oceanography.*

M. Alford, Thomas Peacock, J. MacKinnon, J. Nash, M. Buijsman, L. Centuroni, S. Chao, M. H. Chang, D. Farmer, O. Fringer, K.H. Fu, P. Gallacher, H. Graber, K. Helfrich, S Jachec, C Jackson, J. Klymak, D. S. Ko, S. Jan, T. M. Johnston, S. Legg, I. H, Lee, R. C. Lien, M. J. Mercier J. N. Moum, **R. Musgrave**, J. H. Park, A. I. Pickering, R. Pinkel, L. Rainville, S. R. Ramp, D. L. Rudnick, S. Sarkar, A. Scotti, H. L. Simmons, L. C. St. Laurent, K. Venayagamoorthy, Y. H. Wang, J. Wang, Y. J. Yang, T. Paluszkiewicz, T. Y. Tang. *The formation and fate of internal waves in the South China Sea.* Nature, 521, 65-69, 2015.

M. J. Reeder; T. Spengler; **R. C. Musgrave**. *Rossby Waves, Extreme Fronts, and Wildfires in Southeastern Australia.* Geophysical Research Letters, 42, 2015-2023, 2015.

J. D. Nash; E. L. Shroyer; S. M. Kelly; M. E. Inall; T. F. Duda; M. D. Levine; N. L. Jones; **R. C. Musgrave**. *Are any coastal internal tides predictable?* Oceanography 25(2):80-95. 2012.

Matthew H. Alford; Jennifer A. MacKinnon; Jonathan D. Nash; Harper Simmons; Andy Pickering; Jody M. Klymak; Robert Pinkel; Oliver Sun; Luc Rainville; **Ruth Musgrave**; Tamara Beitzel; Ke-Hsien Fu; Chung-Wei Lu. *Energy flux and dissipation in Luzon Strait: Two tales of two ridges.* Journal of Physical Oceanography 41(11):2211-2222. 2011.

Kilborn, V. A.; Koribalski, B. S.; Forbes, D. A.; Barnes, D. G.; **Musgrave, R. C.** *A wide-field H1 study of the NGC 1566 group*, Monthly Notices of the Royal Astronomical Society, 356:77-88. 2005.

ABSTRACT OF THE DISSERTATION

Tidal interactions with topography: the effects of latitude and tidal constitution on nearfield mixing

by

Ruth Claire Musgrave

Doctor of Philosophy in Oceanography

University of California, San Diego, 2015

Professor Jennifer MacKinnon, Co-Chair
Professor Robert Pinkel, Co-Chair

We describe and interpret in situ observations of tidally driven turbulence that were obtained in the vicinity of a small channel that transects the crest of the Mendocino Ridge in the north-eastern Pacific. Flows are funneled through the channel and have tidal excursion lengths comparable to the width of the ridge crest. Once per day, energetic turbulence is observed in the channel, with overturns spanning almost half of the full water depth. A high resolution, nonhydrostatic, 2.5-dimensional simulation is used to interpret the observations in terms of the advection of a breaking tidal lee wave past the site location, and subsequent development of a hydraulic jump. During this phase of the tide the strong transports

were associated with full depth flows, however, during the weaker beat of the tide transports were shallow and surface-confined, generating negligible turbulence. A regional numerical model of the area finds that the subinertial K1 (diurnal) tidal constituent generates topographically trapped waves which propagate anticyclonically around the ridge, and are associated with enhanced near-topographic K1 transports. The interaction of the trapped waves with the M2 (semidiurnal) surface tide produces a baroclinic tidal flow that is alternately surface confined and full depth. Consistent with observations, full depth flows are associated with the generation of a large amplitude tidal lee wave on the northward face of the ridge, while surface confined flows are largely nonturbulent. The regional model demonstrates that nearfield dissipation over the entire ridge is diurnally modulated, despite the larger amplitude of the M2 tidal constituent, indicating that the trapped wave modulates near-field dissipation and mixing at this location.

In the final section, we study the interaction of the barotropic tide with a tall, two-dimensional ridge both analytically and numerically at latitudes where the tide is subinertial, and contrast it to when the tide is superinertial. When the tide is subinertial the energy density associated with the response grows with latitude as both the oscillatory along-ridge flow and near ridge isopycnal displacement become large. Nonlinear processes lead to the formation of along-ridge jets, which become faster at high latitudes. Mixing occurs mainly through hydraulic jumps on the flanks of the topography in both cases, though a superinertial tide may additionally generate mixing above topography arising from the convective breaking of radiating waves.

Chapter 1

Introduction

The barotropic tide is the most familiar of the ocean's movements, driving the daily advance and retreat of coastal water levels around the globe. It arises as the oceanic response to the tidal stresses generated by the sun and the moon, taking the form of Kelvin waves: free modes of individual basins which propagate on their peripheries. Tidal Kelvin waves are the dominant source of sea surface height variability in the ocean, with amplitudes on the order of one meter close to coasts.

Combining TOPEX/Poseidon and Jason satellite data with an inverse model, *Egbert and Ray* (2003) determined that the barotropic tide has a total energy of around 460 EJ (exajoules (EJ): 10^{18} J), and dissipates at a rate of 3.5 TW. The implication is that the entire ocean's tidal energy is renewed approximately every 36 h. The oceans are the main source of tidal dissipation in the earth-moon-sun system, with the combined dissipations by atmospheric and solid earth tides contributing only an additional 0.1 TW (*Platzman*, 1991; *Ray et al.*, 1996). Independent estimates of tidal dissipation have been made by observations of its astronomical influence, increasing the Earth's length of day, and the distance between the Earth and moon as the earth-moon system loses energy (*Christodoulidis et al.*, 1988).

The globally averaged energy pathway for tidal dissipation is quantitatively well constrained. Of the 3.5 TW of tidal energy that dissipates in the ocean, 2.5 TW is estimated to dissipate in the shallow seas through bed friction, with

the remaining 1 TW dissipating in the deep ocean (*Egbert and Ray*, 2003). For comparison, solar radiation imparts energy to the surface of the earth at a rate of 2×10^5 TW, however, the net power input into the ocean by buoyancy forcing is negligible, and may even be negative. Instead, it is the mechanical forcing of the winds and tide that drives the ocean circulation (*Wunsch and Ferrari*, 2004). Of the 1 TW of deep ocean tidal dissipation, 0.75 TW is associated with the M2 tidal constituent, of which only 13% is thought to dissipate through bed friction, with the remainder being converted into baroclinic internal tides (*Green and Nycander*, 2013). The transfer of energy to internal tides that can move energy away from their generation site further complicates attempts to map energy dissipation, and, in this regard, dissipation in the deep ocean is fundamentally different from that in shallow seas.

The dissipation of kinetic energy gives rise to a turbulent diffusivity (κ), which can be estimated from the dissipation rate using the steady state turbulent kinetic energy equation under a series of assumptions (*Ivey et al.*, 2008). The turbulent diffusivity driven by the dissipation of wind and tidally driven internal waves is the mechanism by which abyssal waters, injected into the deep ocean at high latitudes, are mixed upwards and set the ocean's stratification. *Munk* (1966) balanced the sinking at high latitudes with an imagined uniform diffusive upwelling over the rest of the ocean, and found that $\kappa = 1 \times 10^{-4}\,\mathrm{m^2\,s^{-1}}$ was required to maintain observed stratification profiles. A recent compilation of global measurements has confirmed this average value below the main thermocline, though diffusivities are enhanced over rough topography, and, on average reduced above the thermocline (*Waterhouse et al.*, 2014). The enhanced diffusivities over rough topography are particularly important in setting the deep stratification, and the rate at which deep waters are returned to the surface.

Recent developments in global climate models have illustrated the sensitivity of the ocean's circulation to the magnitude and distribution of mixing. In comparing a traditional constant diffusivity global model to one in which diffusivities were parameterized and, therefore, variable, *Jayne* (2009) found that the strength of the deep Meridional Overturning Circulation was significantly strength-

ened by parameterized diffusivities. *Melet et al.* (2013) showed that the vertical distribution of diffusivity influenced the ocean state. As such, physically based parameterizations of tidally driven mixing are an important component of climate models, determining our ability to predict ocean circulation under changing climate conditions. Though attempts have been made to parameterize some aspects of tidally driven mixing (e.g. *Jayne and St Laurent* (2001) and *Klymak et al.* (2010a)), our understanding, and therefore representation of the mechanisms that lead to the dissipation of tidal energy remains incomplete.

1.1 Some routes to the dissipation of tidal energy in the ocean

1.1.1 Internal tide generation

In the deep ocean, most of the dissipation of energy from the barotropic tide occurs by conversion to baroclinic motions, which may dissipate in place or radiate away and dissipate elsewhere. In this section we give a brief overview of internal tides, the baroclinic motions upon which the barotropic tide projects.

1.1.1.1 Radiating internal tides

Radiating internal tides are generated at topography where the tidal frequency is greater than the local Coriolis frequency. They satisfy the dispersion relation for internal waves,

$$\frac{m^2}{k^2} = \frac{N^2 - \omega^2}{\omega^2 - f^2} \tag{1.1}$$

where N is the Brunt-Väisälä frequency, ω is the frequency of the wave, f is the Coriolis frequency, and (k, m) is the vector wavenumber. Some key properties of internal waves can be deduced from the dispersion relation: 1. They propagate both vertically and horizontally through the water at an angle with respect to the horizontal that increases with frequency; 2. Their frequencies are constrained between $f < \omega < N$; and 3. Their phase velocity is perpendicular to their group

velocity in the vertical plane. In some locations, such as Hawaii, satellite altimetry has successfully tracked beams of internal tide energy radiating outwards for many thousands of kilometers (*Ray and Mitchum*, 1997; *Zhao and Alford*, 2009). Internal tides that survive this far from their source are mode one: a pair of internal wave rays propagating in phase to form a coherent vertical structure that is able to efficiently transport energy with minimal dissipation. When transiting the ocean these waves may be subject to nonlinear interactions such as Parametric Subharmonic Instability (PSI), causing them to transform to other frequencies and scales and, in doing so, fill out the rest of the internal wave spectrum (*Hibiya et al.*, 2002; *MacKinnon and Winters*, 2005). Wave energy that is transferred to small enough scales can break, leading to elevated turbulent diffusivities in the open ocean. The ultimate fate of low mode internal tides, however, remains unknown, and questions regarding the most important processes of internal tide dissipation are outstanding. Mechanisms may include shoaling at continental shelves (*Kelly et al.*, 2013), as well as interaction with both topography and the mesoscale leading to scattering to higher modes (*Johnston and Merrifield*, 2003; *Sheen et al.*, 2015).

The generation of internal tides at topography is a complex problem in part because of the number of nondimensional parameters involved. One of the most important parameters is the nondimensional tidal excursion length, l_{exc}, which is the ratio between the tidal excursion length, u_0/ω, and a characteristic length-scale of the bathymetry, L. Also important is the ratio of the topographic slope to the internal waves slope, ϵ, which determines whether or not the topography is subcritical ($\epsilon < 1$) or supercritical ($\epsilon > 1$). One class of analytic solutions are for "weak" topography, with heights much smaller than the depth of the ocean. These solutions are applicable when wave characteristics are much shallower than the topographic slope ($\epsilon \ll 1$), and simplify the problem by applying the bottom boundary condition at $z = 0$, rather than on the topography itself (*Bell*, 1975; *Llewellyn Smith and Young*, 2002; *Khatiwala*, 2003). For topography satisfying these constraints, *Bell* (1975) showed that two regimes of internal tide generation exist: for small excursion lengths (the "acoustic limit"), internal tides are generated at the forcing frequency, whilst for large excursion lengths (the "lee wave

limit"), internal waves are generated at forcing and harmonic frequencies. For tidal conversion by tall, steep topography, a Green's function approach has been found useful, and progress has been made in the acoustic limit for near and super-critical ridges (*Llewellyn Smith and Young*, 2003; *Pétrélis et al.*, 2006; *Balmforth and Peacock*, 2009). Close to topography, internal tide beams follow internal wave characteristics that can be the site of elevated turbulent dissipation rates through steepening and breaking in the beam (*Cole et al.*, 2009).

1.1.1.2 Trapped internal tides

In contrast to radiating tides, which have a low frequency limit set by f, trapped tides can be generated at all frequencies below $N\sin(\alpha)$, where α is the topographic slope. They are particularly important when the tidal forcing is subinertial. First considered by *Rhines* (1970), their properties are distinct from their freely radiating counterparts. In the limit of vertical topography ($\alpha \to 90°$) they become internal Kelvin waves, trapped to topography by rotation, but with a dispersion relation unaffected by it. As the topography becomes less steep, the topographic trapping becomes greater and flows become more bottom constrained (*Rhines*, 1970). For isolated topography such as a seamount, trapped waves can be thought of as the eigenmodes of the bathymetry and stratification, and are associated with specific eigenfrequencies and wavelengths. When one of the eigenfrequencies is close to an ambient frequency in the ocean, such as a tidal constituent, the relevant eigenmode is resonantly excited (*Chapman*, 1989).

Though trapped tides cannot directly contribute to mixing in the open ocean, they may still generate significant mixing close to topography. Recent work by *Müller* (2013) indicated that 30% of the dissipation of the diurnal barotropic tide occurs above the turning latitude, defined as the latitude where the local Coriolis frequency matches the tidal frequency, presumably through the generation and dissipation of trapped tides. The dissipative properties of trapped tides were noted in a study by *Codiga and Eriksen* (1997), who showed the dissipative timescale of trapped waves at the Cobb Seamount to be of only two days. Mixing associated with trapped waves may be especially important in high latitude regions such as

the Arctic and Antarctic, where upward heat transport from depth can affect the rate of sea-ice melt, or the basal erosion of glaciers.

1.1.2 Nearfield turbulence and mixing

In addition to generating internal waves, tidal interaction with topography frequently involves energetic turbulence in the nearfield, arising from phenomena, including turbulent boundary layers, breaking waves and internal hydraulic jumps (*Klymak et al.*, 2008; *Nakamura et al.*, 2010; *van Haren et al.*, 2015). These phenomena are both strongly nonlinear and time dependent, and lack full analytic descriptions. Nonlinearity in the nearfield can be generated by large excursion length flows, which, in a nondimensionalization of the governing equations, results in the dominance of the nonlinear over the time-dependent term. This motivates the use of the quasi-steady approximation when looking at such flows, which assumes that they are instantaneously in balance and not accelerating. Observations and modeling indicate that this approach is reasonable as many of these time dependent phenomena appear qualitatively familiar from steady flows. As such, we outline some basic properties of steady stratified flows over obstacles next.

Steady stratified flow over two-dimensional obstacles has been extensively studied in relation to atmospheric flow over mountain ranges, which can generate downslope windstorms and hydraulic jumps in the lee (*Peltier*, 1979). An important parameter is the topographic Froude number, $Fr = u_0/Nh$, where h is the height of the obstacle, and u_0 and N are as defined previously. In a laboratory study, *Baines and Hoinka* (1985) showed that for large values of the Froude number, flows resembled linear lee waves - internal waves with intrinsic frequencies set by the flow speed and scale of topography, and whose phase speed is matched to the speed of the oncoming flow (*Gill*, 1982). However, decreasing the Froude number led to the development of blocked layers of fluid both upstream and downstream, as well as the steepening and breaking of the lee waves. In a series of numerical simulations, *Klymak et al.* (2010b) considered steady flow over obstacles in the deep ocean at small Froude number, which are distinguished from similar atmospheric flows by the presence of a rigid upper boundary, and found that the

vertical structure of flows at the crest of the ridge was well predicted by the consideration of arrested lee wave modes. These modes have a scale that is set by the topography and the speed of the flow over the obstacle, with faster flows trapping lower modes (associated with higher phase speeds). The influence of small Froude number in these simulations is to thicken and accelerate the lowest lobe of the trapped wave, and *Winters and Armi* (2012) showed that this jet is hydraulically controlled, generating turbulence and mixing in a hydraulic jump downstream.

The approximation of tidally driven flows as quasi-steady has yielded significant understanding of the processes leading to nearfield turbulence, however, it inherently neglects the connection between the time-dependent generation of internal tides and the steady phenomena to which turbulence are being attributed. To draw the link between the two, the linear solution of *Bell* (1975) is useful as it explicitly illustrates the transition from time-dependent internal tides to steady linear lee waves with increasing excursion length. Though the solution is linear, the expected effect of nonlinearity is to steepen the radiating waves, eventually causing them to break.

When excursion lengths are small, nearfield turbulence can still occur if the topographic slope matches the slope of the internal tide (*Gayen and Sarkar*, 2011). In this case, nonlinearities arise through the resonant response of the flow to the topography, and turbulence occurs in the boundary layer. Near-critical turbulence can be so energetic that some studies have suggested that this process shapes the continental slopes (*Cacchione et al.*, 2002).

In summary, we see that tidally driven flows generate a range of phenomena that can lead to nearfield mixing, including breaking internal tides, hydraulic jumps, critical slope turbulence and lee waves. Understanding and parameterizing these phenomena is significantly challenged by their intrinsic nonlinearity, and remains an important problem.

We address the issue of tidally driven turbulence at large excursion lengths in this dissertation, the goals which are twofold: 1. To extend our understanding of tidally driven mixing over idealized two-dimensional bathymetry when the tide is subinertial; and 2. To explore some of the specific processes that occur at the

Mendocino Ridge, where both a trapped and radiating internal tide are generated. The interplay between the trapped and radiating tides at the Mendocino Ridge has broad relevance to the rest of the ocean, as at latitudes between 30° and 75° (47% of the Earth's surface) only the semidiurnal tide radiates, whilst the diurnal tide is trapped to the generating topography. We show that this interaction has important implications for regional energy budgets, and deserves both observational and theoretical attention.

1.2 Outline of the Dissertation

1.2.1 The Mendocino Ridge

In the first two chapters of this dissertation we focus on the Mendocino Ridge in the north-eastern Pacific. This site is particularly interesting as two tidal constituents, K1 (diurnal) and M2 (semidiurnal), are present in the barotropic tide, but the K1 constituent is subinertial while the M2 constituent is superinertial. *Althaus et al.* (2003) identified this ridge as an important M2 internal tide generator for the region, while *Egbert and Ray* (2003) found elevated dissipation of the K1 tidal constituent close to the coast. Our work supports both of these findings, and develops a detailed understanding of the mechanisms that lead to tidally driven turbulence and mixing at this location.

1.2.1.1 Processes in a channel through the ridge

In the first chapter, we examine ship-based and moored observations from the vicinity of a small channel incising the crest of the Mendocino Ridge, where tidal flows exceed 1 $\mathrm{m\,s^{-1}}$ during some phases of the tide. A strong diurnal inequality characterizes observations at this location, and during the strongest beat of the daily tide, energetic turbulence gives rise to dissipation rates of up to 60 $\mathrm{W\,m^{-2}}$. Using a high resolution, nonhydrostatic, two-dimensional numerical model, we interpret our observed timeseries in terms of large breaking tidal lee waves and hydraulic jumps. We use the theory described by *Bell* (1975) to understand the tidal

lee waves formed by these long excursion length flows as a sum of wave responses at both fundamental and harmonic frequencies.

1.2.1.2 The influence of a trapped tide on regional energetics

In the first chapter we focussed on the strong beat of the tide, when cross-ridge flows form an accelerated jet that resolves in a hydraulic jump on the ridge flanks. In this chapter, we understand the weak beat of the daily tide, where northward transport at the crest of the ridge is confined to the surface and flows at depth are almost quiescent. During this phase of the tide we observe no turbulence or mixing as tidal transport appears not to directly interact with the ridge. We use a three-dimensional tidal model to investigate the regional dynamics that set up the baroclinic structure of the tide, and find that the subinertial K1 tidal constituent generates a trapped internal tide which interacts with the surface tide at the crest of the ridge such that near-bottom flows are alternately enhanced and suppressed. A comparison of energetics in *K1-only*, *M2-only* and *K1+M2* simulations demonstrates that the combination of constituents increases the overall dissipation rate and barotropic-baroclinic conversion by the ridge, compared to the sum of the individual constituent simulations.

1.2.2 The influence of latitude on tidal forcing at a 2D ridge

In the final chapter we move away from observations and realistic modeling toward an idealized study of tidal flow over a tall, two-dimensional Gaussian bump. We extend the linear analytic solution of *Llewellyn Smith and Young* (2003) for superinertial tidal flow over a knife-edge ridge to subinertial tides, and find that the energy density of near ridge flows increases with latitude when the tide is subinertial. We validate our predictions using a series of numerical simulations at a range of latitudes, and explore nonlinear features unreachable using linear theory. We find that nonlinearities generate rectified, along-ridge flows with magnitudes that increase with latitude, and that near-topographic mixing arises

predominantly through hydraulic jumps at high latitudes, while at low latitudes the direct breaking of radiating waves is also a contributor.

Chapter 2

Tidally driven processes leading to nearfield turbulence in a channel at the crest of the Mendocino Escarpment

In situ observations of tidally driven turbulence were obtained in the vicinity of a small channel that transects the crest of the Mendocino Ridge. Flows are funneled through the channel and have tidal excursion lengths comparable to the width of the ridge crest. Once per day energetic turbulence is observed in the channel, with overturns spanning almost half of the full water depth. A high resolution, nonhydrostatic, 2.5-dimensional simulation is used to interpret the observations in terms of the advection of a breaking tidal lee wave past the site location, and subsequent development of a hydraulic jump. Modeled dissipation rates show that turbulence is strongest on the flanks of the ridge, and that local dissipation accounts for 28% of the energy converted from the barotropic tide into baroclinic motion. The importance of small scale bathymetry for the spatial distribution of tidally driven turbulence is demonstrated by the comparison of time series obtained in the channel to time series obtained a few kilometers away over the adjacent ridge, which exhibit comparable flow speeds, but an order of

magnitude smaller depth integrated dissipation rates.

2.1 Introduction

The direct generation of turbulence by the interaction of the barotropic tide with topography provides an energy pathway linking the ocean's largest scales to its smallest. This "nearfield" turbulence drives mixing and water mass modification close to topography in the deep ocean, and has far reaching influence over regional and basin scale circulations (*Hasumi and Suginohara*, 1999; *Simmons et al.*, 2004; *Osafune and Yasuda*, 2013; *Melet et al.*, 2013). Understanding of the magnitude and distribution of this mixing is challenging because of the wide range of oceanic conditions under which it occurs, and the different turbulence generating phenomena that may be present.

In this paper we examine the specific processes that link the barotropic tide to nearfield turbulence in and around a channel transecting the crest of the Mendocino Ridge in the eastern Pacific. We use both in situ observations and a numerical model to build a detailed view of the phenomenology present at this site. Intense turbulence has been observed close to topography via the generation of tidal lee waves and hydraulic jumps at deep ocean sites such as Hawaii (*Klymak et al.*, 2008) and Luzon Strait (*Alford et al.*, 2011), as well as shallower locations such as the Kuril Straits (*Nakamura et al.*, 2010). We observe and discuss these phenomena at the Mendocino Ridge, and are able to clearly identify turbulence associated with radiating internal waves in our observations.

An important parameter describing both the nature of the response and the extent to which it is nonlinear is the nondimensional tidal excursion length,

$$l_{exc} = \frac{U_c}{\omega L} \tag{2.1}$$

where U_c is the peak tidal speed, ω is the tidal frequency, and L is a characteristic topographic width (defined in Section 2a). In this paper we follow *Klymak et al.* (2010a), defining U_c at the crest of the ridge, as for tall topography this is the speed that has most relevance to near-crest dynamics. Where excursion lengths are much greater than 1, tidal lee waves are often approximated as quasi-steady

(*Farmer and Smith*, 1980). However, at the Mendocino Ridge, $l_{exc} \approx 1$, and we use the framework outlined by *Bell* (1975) for oscillatory stratified flow over small topography that extends from infinitesimal excursion length, $l_{exc} \to 0$, (the "acoustic" limit) to arbitrarily long excursion length, $l_{exc} \to \infty$ (the "lee wave" limit). In the acoustic limit, an internal tide is generated at the fundamental frequency, whilst in the lee wave limit, Bell's solution reverts to that of a classic steady lee wave (*Gill*, 1982). For intermediate, finite excursion length flows, these limits are explicitly connected by the generation of an internal wave response at both the forced and harmonic frequencies, and it is the time dependent superposition of this multi-frequency response that generates tidal lee waves. As for classic steady lee waves, Bell's solution is only strictly valid for small topography with shallow slopes. Nevertheless, the conceptual model remains relevant: tidal lee waves arise from the constructive interference of both fundamental and higher harmonic wave patterns during some phases of the tide. Close to topography this superposition forms structures that resemble internal tide beams, whose lines of constant phase have slopes that are steeper than that associated with the fundamental frequency response due to the influence of higher harmonics. Nonlinearity causes the constituent frequencies in the tidal lee wave to interact, steepening isopycnals and leading to turbulence. One of the goals of this paper is to draw attention to this conceptual framework for understanding tidal lee waves, as it is additionally useful at locations where the barotropic tide itself may involve more than one frequency, each of which generates a baroclinic response at their fundamental and harmonic frequencies. The result is a complex but predictable tidal lee wave response.

We distinguish between turbulence arising from the steepening and breaking of radiating "Bell-like" tidal lee waves described above, and turbulence associated with flow separation, which we attribute to transient hydraulic jumps. These form on the lee side of the topography downstream of a fast, cross-ridge jet which is hydraulically controlled at the ridge crest. Following *Winters and Armi* (2013), we define the layer Froude number of the jet as the ratio of the mean speed in the jet ($\bar{U}$), to the speed of interfacial waves along the jet:

$$Fr_l = \frac{\bar{U}}{Nl}, \tag{2.2}$$

where N is the Brunt-Väisälä frequency, and l is the layer thickness. Though lee waves and hydraulic jumps tend to occur together, and are consequently often discussed together, we find it useful to distinguish them in this way as the bottom accelerated jet that forms over tall, steep topography generates turbulence even when the radiating wave component of the response is very small, for example when the tide is subinertial.

Distinct from the layer Froude number, is the topographic Froude number,

$$Fr = \frac{U_c}{Nh}, \tag{2.3}$$

which determines the ratio of the vertical displacement of a fluid parcel, $\delta = U_c/N$, to the height of the bathymetry, h. Fluid parcels deeper than δ below the ridge crest are blocked on one side of the topography when $Fr < 1$ (*Farmer and Smith*, 1980).

Starting with *Farmer and Smith* (1980), much of the phenomenology of tidal lee waves has been described in terms of trapped modes, with large amplitude tidal currents trapping increasingly faster (lower mode) waves. This quasi-steady approach is particularly useful for understanding the vertical structure of the flow at the crest (*Klymak et al.*, 2010b), but provides little guidance on the time-dependence of the flow, in particular how internal tide generation (at the forced frequency) is linked to the much higher (intrinsic) frequency lee waves. Our discussion of these processes in terms of Bell's theory is intended to complement this modal description, in a framework that enables a more general understanding of the time-dependent wave dynamics of the response.

Analytical and numerical work to date has focused on nearfield turbulence over two-dimensional bathymetry (*Legg and Klymak*, 2008; *Klymak et al.*, 2010a; *Rapaka et al.*, 2013), and the influence of small scale three-dimensionality remains relatively unexplored. An outstanding question is to what extent parameterizations such as that proposed by *Klymak et al.* (2010a) are applicable when the bathymetry is three-dimensional. Though we do not address this question fully in this study, we are able to use a 12-day moored timeseries from the center of the channel to estimate a power law relation between tidal velocity and dissipation rate. In a separate paper (*Musgrave et al.* (2015a), hereafter M15b) we explore issues relating

to three-dimensional bathymetry more thoroughly with the aid of a regional tidal model of the area. We find that the presence of a subinertial tidal constituent at the Mendocino Ridge generates an energetic topographically trapped internal tide. This bottom trapped wave contributes to large daily inequalities in tidal transport through the channel, as well as inhibiting the formation of tidal lee waves during the weaker of the daily tides due to its baroclinic structure.

The remainder of the paper is split into five parts. In Section 2 we detail the site location, observations, analysis methods and numerical model setup. In Section 3 we present results from the observations and model and assess how well the model reproduces the data. We interpret the observations in the channel with the aid of the model in Section 4, and clearly distinguish between the two different turbulence generating phenomena in the channel: tidal lee waves and hydraulic jumps. In Section 5 we relate tidally averaged dissipation rates to tidal velocity from a 12 day moored time series at the center of the channel. Finally, in Section 6 we present a summary of our results.

2.2 Experimental details

2.2.1 Site location

The study area is situated around 30 km from the North American coast in the eastern Pacific, at a latitude of 40°N. Ship-based observations were obtained in and around a small channel transecting the crest of the Gorda Escarpment, where the Mendocino Ridge joins the continental shelf (Figure 2.1a). *Althaus et al.* (2003) (hereafter AL03) analyze a series of measurements in a longitudinal line over the ridge in the open ocean to the west of our site. They identify the ridge as a significant internal tide source in the north-east Pacific, generating a total semidiurnal tidal flux (north and south) of up to 7 kW m^{-1}, an observation that is supported by the moored timeseries of *Alford* (2010) located much closer to our site. AL03 also identify heightened dissipation in a layer up to 500 m thick close to the crest of the ridge, suggesting the presence of turbulent near-ridge phenomena.

The Mendocino Ridge is a large scale bathymetric feature, rising around 1000 m and 2000 m from the abyssal plains to the north and south, respectively, and extending over 2000 km westward into the Pacific at a depth greater than 1000 m for most of its length. On scales such as these, the ridge may reasonably be considered to be two-dimensional. However, the phenomena giving rise to near-field turbulence occur on scales of order a few kilometers and consequently are influenced by "small scale" bathymetric features such as the channels, canyons and hills present along the crest and flanks of the ridge. With this in mind, the experiment was designed to compare turbulent processes in the channel, and over the ridge flanking the west side of the channel. Though we present all of the data from these observations in this paper, the regional dynamics that lead to the differences between flows in each location are dealt with in M15b.

Our study site focusses on a channel with a width of around 4 km, a crest depth of approximately 500 m. It represents a localized drop in the height of the ridge crest of about 200 m (Figure 2.1b). Crosses represent regions of slope that are near-critical, with slopes within ± 0.01 of the semidiurnal (M2) characteristic at a constant stratification of 3 cph, appropriate for these depths. In the immediate vicinity of the crest, the slopes to the north and south are steep and supercritical to M2 internal tides. However the southern slope shallows to a near critical slope around 5 km away from the crest.

Barotropic flows at the location of the mooring were estimated using the TPXO West Coast USA tidal model (*Egbert and Erofeeva*, 2002), hereafter referred to as TPXO, which uses satellite altimetric data to constrain solutions to the Laplace Tidal Equations on a $1/30^\circ$ bathymetric grid (about 3 km at this latitude). A time-series for predicted across-ridge flows at the mooring during the period of observations (Figure 2.1c) shows that, like much of the eastern Pacific, this site is subject to a mixed tide, with diurnal (K1) and semidiurnal (M2) constituents dominating and having amplitudes of 0.38 and 0.62 m, respectively. We use the peak cross-ridge velocity predicted by TPXO at the mooring site during the observation period of $U_c = 0.4\,\mathrm{m\,s^{-1}}$, to estimate the tidal excursion length at the crest as $U_c/\omega_{M_2} \approx 3\,\mathrm{km}$. The relevant topographic length-scale is deter-

mined by the ridge width at a depth $\delta = U_c/N$ below the crest - below this depth fluid is blocked and does not pass over the ridge. In this case we estimate the topographic length scale to be around 4 km, giving a predicted non-dimensional excursion length for this channel of $l_{exc} \approx 1$, indicative of the importance of non-linearity at this location. As the observed flow speeds were more than double the TPXO predictions, this excursion distance is a lower bound on the observations discussed here.

For this ridge we estimate $Fr \approx 0.1$, meaning that the bulk of the upstream water at a given phase of the tide is blocked and does not surmount the crest. Whilst topographic Froude numbers this small are typical under oceanic conditions, such large excursion lengths and tidal transports as those measured at this location are less common, and it is the combination of these factors that makes these observations unique.

2.2.2 Observations

Measurements were obtained in November 2012 using a combination of ship based and moored instruments. A subsurface mooring was placed close to the center of the channel (marked 'M' in Figure 2.1b) from 15-27 November 2012. The mooring comprised 16 temperature loggers (SBE56s) and two pressure/temperature/conductivity loggers (SBE37s) sampling at 1 Hz and 0.01 Hz respectively. Most temperature loggers were spaced approximately 20 m apart and spanned the central region of the mooring, however two additional temperature loggers were placed just above the anchor and just below the subsurface float, and were separated from the rest of the vertical array by 40 m and 30 m respectively. The SBE37s were located at the subsurface float (at a nominal depth of 100 m) and just above the anchor (at a depth of 460 m), and provided an indication of how far the mooring was knocked down by the strong currents as well as the salinity-temperature properties of the water mass. The upper SBE37 recorded depths of up to 270 m during periods of strong flow (i.e. 170 m deeper than when the mooring was upright), and in subsequent sections we infer the depths of the intermediate temperature loggers assuming that the mooring cable between the

two SBE37s was straight. In addition, a 75 kHz down looking long range Acoustic Doppler Current Profiler (ADCP) was installed in the upper float, and a down looking 500 kHz ADCP at 410 m depth. Unfortunately the 500 kHz ADCP failed shortly after deployment.

Dissipation rates at the mooring are estimated from the 1 Hz temperature loggers using the method described in *Zhang and Moum* (2010). Spectra of temperature gradients computed from 120 s segments are fitted to Bachelor spectra in the inertial-convective subrange to establish the dissipation rate of thermal variance, χ, which is related to the turbulent diffusivity of heat (K_T) by the Osborne-Cox relation (*Osborn and Cox*, 1972). Under the assumptions that turbulent diffusivities of heat and momentum are equal ($K_T = K_\nu$), and that there is a local balance between turbulent kinetic energy, shear production and buoyancy, the turbulent dissipation rate may be solved for. Densities at each of the temperature loggers were inferred from a look-up table of salinities and temperatures generated from combined Conductivity-Temperature-Depth (CTD) station data and SBE37 mooring data. Salinity-temperature (S-T) relations indicate that the water mass properties around the mooring were fairly homogeneous over the duration of the measurements, and the S-T relation was monotonic. The largest variance in salinities for a given temperature class were associated with warmer surface waters, and we estimate a maximum error in our inferred densities of $\pm 0.12\,\mathrm{kg\,m^{-3}}$.

With the mooring in place, four CTD-LADCP stations were undertaken ranging in duration from 20-30 hs. Two 300 kHz Lowered Acoustic Doppler Profilers (LADCPs) were fixed to the CTD cage, one oriented looking upwards, the other oriented looking down, providing 8 m binned velocity data to within a few meters of the bottom. Data were processed using the LDEO_IX software (*Visbeck*, 2002), and are presented as along- and cross-channel components (a 17° clockwise rotation of the coordinates). Two channel stations (C1 and C2) were 2 and 3 km to the north of the mooring along the centerline of the channel at the 700 and 800 m isobath, respectively. The two ridge stations (R1 and R2) were on the ridge crest of the west flank of the channel (350 m depth), and just north of it at 450 m depth. These stations are marked in Figure 2.1b. The CTD-LADCP package was

nominally lowered to between 5-10 m from the bottom, but currents occasionally in excess of $1.2\,\mathrm{m\,s^{-1}}$ made accurate depth positioning of the package difficult, inhibiting our ability to profile close to the bottom during some phases of the tide.

Turbulent dissipation rates on station were calculated from density inversions in CTD profiles by computation of the Thorpe scale of the overturn. The Thorpe scale is then related to the Ozmidov scale to estimate the turbulent dissipation rate (*Thorpe*, 1977; *Dillon*, 1982). Spurious overturns were removed using the tests described in *Galbraith and Kelley* (1995) and *Gargett and Garner* (2008).

To help establish the lengthscales and timing of ridge-top flows before finalizing the station locations, 10 cross-ridge transects of velocity were obtained over a 13 h period using the 75 kHz shipboard acoustic doppler current profiler (SADCP). The ship steamed repeatedly along the black lines marked in Figure 2.1 in a zig-zag pattern at 7 kn ($3.6\,\mathrm{m\,s^{-1}}$), passing down the center of the channel every 1.5 h, and transecting the eastern and western adjacent ridges every 3 h. Each transect took around 0.5 h to complete, resulting in negligible temporal evolution in each of these snapshots. The bottom depth ranged between 300 and 800 m, and the high density of scatterers in this coastal location meant that the SADCP provided a detailed view of the flow over the ridge as the tide progressed. Data were processed and gridded into 1 min bins using the University of Hawaii Data Acquisition System, and as with the LADCP data are presented in subsequent sections rotated into along and cross channel components. Sidelobe interference typical of acoustic instruments contaminates the lower $\sim$100 m of SADCP velocity data and is excluded from the analysis.

2.2.3 Numerical model

To help provide context for the observations, we used the Massachusetts Institute of Technology general circulation model (MITgcm; *Marshall et al.* (1997)) to run a high resolution, 2.5-dimensional simulation along the center of the channel. The model is "2.5" -dimensional due to the inclusion of Coriolis terms in the horizontal momentum equations, which enables Coriolis rotation of the flow without allowing any gradients in the along-ridge dimension. The relatively small

scale of this simulation makes an f-plane approximation appropriate, and we used a value of the Coriolis frequency, f, corresponding to 40° N. We ran the model in nonhydrostatic mode, with a central grid resolution of $dx = dz = 15\,\mathrm{m}$, telescoping outside the domain of interest to $dx = 350\,\mathrm{m}$ close to the lateral boundaries (Figure 2.2b). The simulation had a total of 5.3×10^5 grid points, and was run for 108 simulation hours. The domain was 1300 m deep and 530 km long, large enough that internal waves generated by the topography did not reflect back from the boundaries into the domain of interest during the simulation time. $70 \times 90\,\mathrm{m}$ gridded multi-beam bathymetry extracted from the NOAA database (http://maps.ngdc.noaa.gov/viewers/multibeam/) was used to create a bathymetric profile along the center of the channel (Figure 2.2a). Comparisons between this bathymetry and ship-based measurements were excellent (not shown). The bathymetric profile was padded with flat bathymetry away from the crest, and smoothed to aid numerical stability.

Model forcing was derived by fitting a five frequency (M2, K1 and harmonics 3×K1, 2×M2, 5×K1) harmonic fit for amplitude and phase to the observed transports from stations C1 and C2. The fitted amplitudes were 161 and $147\,\mathrm{m^2\,s^{-1}}$ for the M2 and K1 constituents, respectively: a significantly larger relative contribution of the K1 constituent compared to that predicted by TPXO for this location (see Section 2a). All other constituents had amplitudes less than $20\,\mathrm{m^2\,s^{-1}}$. The reconstructed time-series matched the phase of the observed transport well (Figure 2.2c), but under-predicted the large peaks in northward flow in the observations by almost $200\,\mathrm{m^2\,s^{-1}}$. However, due to the peaked nature of the observed transport, this only resulted in significant errors in forcing for around 3 h during peak flow in station C1. Transport errors during station C2 were significantly less. To allow the model to spin up, the reconstructed forcing time-series was shifted by 50 h so that the time corresponding to the start of station C1 occurred 50 h after initialization. Model forcing was imposed by the addition of a body force to each of the horizontal momentum equations such that the flow in the deeper region to the north of the channel was rectilinear with the desired transports and frequencies (*Di Lorenzo et al.*, 2006). Coriolis effects generated a barotropic rotation in the shallow region

to the south. Inflow/outflow boundary conditions at the lateral boundaries were set to be consistent with barotropic flow induced by the body force in the absence of the ridge.

The model's initial stratification was set to an exponential profile fitted to the C1 station mean stratification, and extrapolated to the depth of the simulated domain (Figure 2.2d). The absence of a restratifying process in the model meant that the density profile gradually diffused over the course of the simulation, and the explicit vertical diffusivity was made small to minimize this effect.

We experimented with two turbulence closure schemes: constant background viscosities and horizontal/vertical diffusivities (viscosity: $\nu = 1 \times 10^{-2}\,\mathrm{m}^2\ \mathrm{s}^{-1}$; horizontal diffusivity: $\kappa_H = 2 \times 10^{-2}\,\mathrm{m}^2\ \mathrm{s}^{-1}$; vertical diffusivity: $\kappa_z = 6 \times 10^{-4}\,\mathrm{m}^2\ \mathrm{s}^{-1}$); and reduced background viscosities and diffusivities combined with an implementation of the Smagorinsky turbulence closure scheme, which dynamically increases viscosity where strain rates are high ($\nu = 2 \times 10^{-3}\,\mathrm{m}^2\ \mathrm{s}^{-1}$, $\kappa_H = 2 \times 10^{-3}\,\mathrm{m}^2\ \mathrm{s}^{-1}$ and $\kappa_z = 6 \times 10^{-4}\,\mathrm{m}^2\ \mathrm{s}^{-1}$). Smagorinsky coefficients of $C_s^2 = 0.02, 0.03$ and 0.04 are trialled. For all simulations, numerical accuracy was evaluated both by the appearance of grid scale noise and the residual closure of a post-simulation computed kinetic energy budget. All simulations reproduced the gross features of the flow, but the simulation with $C_s^2 = 0.03$ and relatively smaller background viscosity and lateral diffusivity is presented here because it is both numerically smooth and captures the steepness of isopycnals before the onset of breaking. The MITgcm employs a second order centered advection scheme for momentum, and we used a one-step seventh order monotonicity preserving advection scheme for temperature (*Daru and Tenaud*, 2004).

2.3 Results

2.3.1 The spatial evolution of flow through the channel: flow snapshots

Figure 2.3 shows a series of along- and cross-channel velocity snapshots acquired using the SADCP as the ship transected the center of the channel 10 times over a period of roughly 13 hours on 14th November 2012. The transects show the development of two northward tides in the along- and cross-channel flows (where the coordinates are rotated clockwise 17° from geographic). The first northward tide initiates in panel a, with a beam-like feature extending from the southern flank of the ridge, generating northward currents at depths shallower than 400 m on the northern flank. As the tide progresses, (panels a to c) the along-channel flow becomes increasingly bottom intensified, with flows in excess of $1.2\,\mathrm{m\,s^{-1}}$ forming a jet whose separation point on the lee side of the slope continues to deepen until slack tide (panel c), attaining a maximum depth of 700 m at around kilometer 5, where it jumps up to 400 m. This bottom intensified jet and downstream separation are consistent with other observations and numerical studies of these phenomena (*Klymak et al.*, 2010b; *Abe and Nakamura*, 2012; *Klymak et al.*, 2012). In panels b and c, weaker northward flow is also present close to the surface in a structure that exhibits oscillations on scales of order 1 km (panel c, shallower than 200 m and between 3-5 km). Once the tide reverses the jet breaks up and weak southward flow is established.

The second northward tide (panels h - j) is markedly different from the first, with all of the along-channel transport accommodated in the upper layer, and persistent weak southward flows at depth. The lack of interaction of the along-channel transport with channel crest means that no bottom intensified jet is generated, and anticipates our finding of negligible turbulent dissipation during this phase of the tide. The total along channel transport in this second northward tide is around 30 % of the transport observed in the first, and represents the strong diurnal inequality that characterized observations during this field experiment. Insets in

Figure 2.3 show the TPXO-predicted barotropic transport for this location, which, whilst matching the phase of observed transports reasonably well, do not show a significant peak-to-peak change in the amplitudes of the northward tides. M15b show that diurnal trapped internal tides are responsible for both the large observed daily inequality and the distinctive surface confined nature of the weak northward tide.

Cross-channel flows (lower panels, Figure 2.3) have magnitudes of around 50 % of the along-channel flows, and are predominantly eastward in the region of strong shear on the forward face of the lee wave. Sections across the adjacent ridge crest (not shown) exhibit smaller transports, but qualitatively similar features, including the formation of tidal lee waves during alternate (strong) northward tides.

2.3.2 12-day tidal evolution at the center of the channel

Figure 2.4 shows the 12 day time-series of a) along- and b), cross-channel velocities at the mooring in the center of the channel, with isopycnals overlaid. A strong diurnal inequality distinguishes the first part of the time-series where very large northward and southward tides ($> 1\,\mathrm{m\,s^{-1}}$) alternate once per day with much weaker tides ($< 0.3\,\mathrm{m\,s^{-1}}$). The inequality persists for much of the first part of the record before gradually becoming weaker as the timings of peak flows associated with the dominant K1 and M2 components shift in relation to one another. Intermittent regions of missing data at shallow depths indicate times when the upper float of the mooring was knocked down by strong currents. Periods of overlap between the mooring and station time-series are indicated above panel a), and are discussed in Section 32.3.3. Depth averaged velocities at the mooring (not shown) indicate that currents are approximately rectilinear and oriented at an angle of about -20° with respect to the channel axis, with along-and cross-channel flows approximately in phase but cross channel-flows having a magnitude of around half of that of along-channel flows.

The depth-time evolution of turbulent dissipation rates inferred from the 1 Hz temperature loggers show distinctive sloping patterns associated with tide

reversals (Figure 2.4c). During the first part of the record where the diurnal inequality is large, both tide reversals during the stronger daily tides progress downwards from the surface with time, and are associated with high isopycnal strain and inferred dissipation rates (e.g. from 15-20 November). Here we loosely define regions of high strain as where isopycnal separations are larger than in an average profile. In addition to the turbulence in the sloping features, enhanced dissipation is present near the bottom in a $\sim$150 m thick turbulent layer of dense water that reaches the mooring during peak tidal flows. Later in the time-series neap tides mean that flow speeds are smaller, and turbulence is generally reduced. The time evolution of depth integrated dissipation rate (black) and mean along-channel velocity (blue) is shown in Figure 2.4d. Depth integrated dissipation rates have peaks associated with the slanted high dissipation rate structures which occur twice per day with values of around 10 W m^{-2}. Peak dissipation rates lag peak tidal flows by around 3 h.

2.3.3 Velocity, density and turbulent dissipation rates at the stations

2.3.3.1 Channel time series

Since SADCP transects showed jet separation on the north-facing flank at around 700 m depth (Figure 2.3c), channel stations were chosen to be just downstream of separation (C1) and at separation (C2). Time series of along- and cross-channel flow, and turbulent dissipation rate are qualitatively similar at each station (Figure 2.5b, c, d): flows are asymmetric in time with distinct patterns of enhanced turbulence associated with certain flow features. Consistent with simultaneous moored measurements (Figure 2.5g, h, i), a strong diurnal inequality causes alternate tides to be much weaker, with the weak tides (e.g. 14-22 h, 16 November) being relatively non-turbulent. Strong northward tides are bottom intensified, with peak flow speeds reaching up to 1.2 m s^{-1} at depth, and weaker surface flows above 200 m, features that can also be seen in the SADCP snapshots of the flow (e.g. Figure 2.3c). The different character of the weak compared to the

strong northward tides is also apparent in these station time-series, with the weak northward flows surface confined, and having very small velocities below 350 m. Transports at each station peak at around $500\,\mathrm{m^2\,s^{-1}}$ and are approximately equal at both C1 and C2, indicating little lateral flow convergence between the stations.

At both stations, strong southward (on-ridge) flow is associated with raised isopycnals and few overturns, whilst strong northward (off-ridge) flows are highly turbulent. The transition between strong southward and northward tides is particularly striking, progressing from the surface to depth over the course of around 7 h, and, as in the mooring time-series, is associated with significant isopycnal strain and turbulence. Each strong northward tide has two distinct patterns of turbulence associated with it: the first follows the sharp transition from southward to northward flow, progressing downwards in time (e.g. 02-08 h, 15 & 17 November 2012); the second occurs later in the cycle as the strong northward tide relaxes (08-12 h, 15, 16 & 17 November 2012). The largest overturns were measured at station C2, just after peak flow at around 350 m depth (Figure 2.5d). Depth integrated dissipation rates are shown in panel e, and show maximum values of up to $10\,\mathrm{W\,m^{-2}}$ at C1, and $100\,\mathrm{W\,m^{-2}}$ at C2 occurring around 3 h after each northward peak flow. The larger values at station C2 reflect a change in our location with respect to the region of largest breaking. Dissipation rates vary over each tidal period by two orders of magnitude, with high dissipation rates present throughout the strong northward tide.

Concurrent time-series of velocity, inferred density and dissipation rate at the mooring show that tide reversals initiate at approximately the same time as at the CTD stations, but progress downwards over the entire water column over a shorter period of time (Figure 2.5g, h, i). In contrast with the station time-series, depth integrated dissipation rates at the mooring have two peaks, each of which is associated with a tide reversal (panel j, black line). The first peak lags strong southward flow and is associated with turbulent phenomena formed on the southern flank of the ridge, while the second peak lags strong northward flow, and is associated with the turbulent phenomena observed on the northern flank at the CTD stations C1 and C2. Turbulent dissipation rates are also elevated in

the dense water that is advected onto the ridge crest during peak northward flows (Figure 2.5, 05-12 h, 15, 16 & 17 November 2012). Southward flows tends to be less turbulent, as the weaker tide that precedes the strong southward flow does not generate turbulence on the northern flank.

2.3.3.2 Ridge time series

Poor weather during these stations made sampling difficult, and after 10 h on 19 November conditions were too rough to continue to take measurements with the CTD/LADCP. Data from this time was obtained solely with the SADCP as the ship remained on station. Gaps appear where air bubbles became trapped in the ADCP cavities under the hull. Qualitative flow features are similar to both the mooring and channel stations, with south to north tide reversals starting at the surface and progressing downwards in time, and weak northward tides being surface confined (Figure 2.6). Peak flow speeds at the crest (R1) are approximately $0.6\,\mathrm{m\,s^{-1}}$, and are associated with peaks in the depth integrated dissipation rate of close to $1\,\mathrm{W\,m^{-2}}$. Downstream at the deeper R2 station, flows have smaller peak speeds of $\sim 0.45\,\mathrm{m\,s^{-1}}$, but similar transports of $\sim 210\,\mathrm{m^2\,s^{-1}}$, indicating no lateral flow convergence or divergence between the two stations (similar to in the channel). The largest turbulent dissipation rates occur just after peak northward flow at Station R1, on the crest of the ridge, where a region of high strain above a strong northward bottom current passes through the station, starting at the surface and progressing downwards in time (11-15 h, 18 November 2012).

2.3.4 Model assessment

Station time-series extracted from the model at Stations C1 and C2 and the mooring location after 50 h of simulation time (Figure 2.5a, f) demonstrate good quantitative agreement with observations, particularly during phases of the tide with large transports. Key features are reproduced such as the tide reversal beginning at the surface and extending downwards in time before splitting into a bottom intensified and surface jet with vigorous turbulence between. During the weak phase of the tide the differences between the modeled and observed

flows are more obvious, as it is during this phase of the tide that the baroclinic structure of the subinertial trapped wave is important, and this is not well captured in this 2.5-dimensional model (M15b). Differences also arise in the duration of flow reversals: simulated flow reversals tend to be too short (5 h), compared to observed reversals (7 h). It is possible that these discrepancies arise from the narrowband forcing in the model compared to the much more broadband tidal forcing in the real ocean. In general, simulated and observed flows are in closer agreement at station C2 than C1 due to a slightly shallower flow separation in the model than the observations. The discrepancy in flow separation perhaps arises from the relatively smaller transports in the model compared to observations. Despite these differences, overall agreement is sufficiently good that the simulation may be used to interpret features in the time-series with confidence.

A post-simulation evaluation of the kinetic energy budget of the model was made for the analysis period. The model exhibits good closure of the budget, with the time-mean residual error more than 5x smaller than the smallest term in the budget: the kinetic energy dissipation rate. The residual error arises from three sources: discretization errors in the post-simulation calculation of the terms of the budget; errors arising from the time-derivative of the kinetic energy which is computed over 10 minute output time-steps, rather than the 1 s model timestep; and errors associated with the numerics, primarily the 2nd-order accurate momentum advection scheme, and 7th-order accurate tracer scheme used by the model, which manifest as numerical diffusion. Though the model is 2.5-dimensional, and relies upon a somewhat ad hoc choice of turbulence parameters, the diagnosed turbulent dissipation rates are the same order of magnitude as the observations over most of the analyzed period (Figure 2.5, and Section 4b). Differences arise during peak flow, when the model forcing does not match the transport to observations, and also during the weak tide, when the model generates a small turbulent tidal lee wave which we do not see in the observations due to the presence of trapped topographic waves.

2.4 Tidal lee waves and hydraulic jumps

2.4.1 The structure of turbulence and flow in the nearfield

In the subsequent discussion we refer to frequencies D1, D2, D3 and D4 as having roughly 1, 2, 3 and 4 cpd, respectively, where D2 includes both the M2 tidal constituent and the second harmonic of K1, D3 is the third harmonic of K1, and D4 includes the second harmonic of M2 and the fourth harmonic of K1.

Eight snapshots of the modeled flow as it develops over 24 h are shown in Figure 2.7. Time is referenced to model time at 74 h, and the period under discussion corresponds to the time Station C2 was occupied. An animation of this period is included in the supplementary material, the upper panel showing velocity (colored) and density (contoured), and the lower panel showing the evolving model time-series at Station C2 (Figure 2.5a). The analysis period starts with a southward tide at 0 h, which forms a strongly bottom intensified jet of anomalously dense water over the southern flank of the ridge crest (Figure 2.7a, also mooring time-series in Figure 2.5 at 00 h on 15 November). The baroclinic structure of the flow during this phase of the tide is broadly consistent with that of a tidal lee wave: a sloping feature having an alternating southward/northward baroclinic structure (i.e. with the depth mean removed). However, the steep isopycnals and strongly accelerated near crest flow indicate that non-linearity is an important part of the dynamics.

The characteristic curves for wave frequencies at D2, D3, D4 and the steady lee wave are shown in Figure 2.7a, b (in increasing steepness). They are calculated from the dispersion relation for internal waves (*Gill*, 1982):

$$\text{characteristic slope} = \frac{k}{m} = \frac{\omega^2 - f^2}{N(z)^2 - \omega^2}, \tag{2.4}$$

where ω is the specified wave frequency, f is the Coriolis frequency, and k and m are the horizontal and vertical wavenumbers of the wave. The steepest curves in Figure 2.7 correspond to steady lee waves, whose frequency is set by the rate at which fluid parcels encounter the ridge crest (*Klymak et al.*, 2010b):

$$\omega_{lee} = U_c k_{topo}. \tag{2.5}$$

k_{topo} is the characteristic wavenumber of the topography at a depth of $\delta = N/U_0$ below the crest, which we have estimated to be 4 km. U_c is the peak tidal speed at the ridge crest, which takes values of $0.65\,\mathrm{m\,s^{-1}}$ for northward flow, and $0.56\,\mathrm{m\,s^{-1}}$ for southward flow (Figure 2.2), giving intrinsic wave periods of 1.7 h on the northern flank, and 2.0 h on the southern flank during peak flow.

As the slope of the tidal lee wave changes with the phase of the tide, it demonstrates poor alignment with any single wave characteristic most of the time. Closest agreement occurs during peak northward flow in Figure 2.7c, when the tidal lee wave is well approximated by the steady response, however we do not see such good agreement on the southern flank during peak southward flow. *Bell* (1975) demonstrates that advection by the barotropic tide causes long excursion length tidal flows to generate internal waves at both fundamental and higher harmonic frequencies, and that it is the superposition of these waves that results in the tidal lee wave: a beam-like feature whose slope changes as the tide progresses and the composite frequencies change their relative phase.

In this simulation there are two dominant frequencies in the background tide (M2 and K1), each of which generates a response at its fundamental and harmonic frequencies (the K1 baroclinic response at this latitude is evanescent and fundamentally different from that at M2). It is the constructive superposition and subsequent dispersion of each of these frequency components that determines the time dependent dynamics of the tidal lee wave. At slack tide the beam-like baroclinic structure of the tidal lee wave is most clear (Figure 2.7b, also 2.7d), before it is advected northward across the ridge crest (Figure 2.7c). Similar features can be found in the SADCP transects (Figure 2.3a, b). Isopycnals in the beam exhibit vertical displacements that are comparable to the horizontal width of the beam, and non-linear steepening causes them to become convectively unstable (Figure 2.7b).

Advection of the tidal lee wave past stations C1 and C2 forms the observed turbulent flow reversals, progressing from the surface to depth as a northward barotropic flow is established. Elevated turbulent dissipation rates of up to $0.03\,\mathrm{Wm^{-3}}$ arising from convective overturning in this structure are identifiable in

the station timeseries between 02-08 h on 15 November 2012 at station C1, and between 02-08 h on 17 November 2012 at station C2 (Figure 2.5d). At the mooring in the center of the channel each tide reversal forms a slanted turbulent structure in the time-series that starts at the surface and extends downwards in time (Figure 2.4c). Unlike the CTD stations on the northern flank which only capture the tidal lee wave formed on the southern flank, the mooring captures turbulence associated with both northward and southward radiating tidal lee waves. Depth integrated dissipation rates show maxima around 3 h after peak tidal flow (Figure 2.4d). Though the mooring was approximately at the center of the channel, south to north tide reversals are not the same as north to south. A comparison of panels a and c in Figure 2.7 shows that differences in both the slopes on the northern and southern flanks of the ridge, and the magnitudes of the northwards and southwards transports influence the structure of the tidal lee wave at peak flow. The lee wave formed on the northern flank of the ridge is steeper than that on the south due to both steeper topography, and relatively stronger northward flows.

As the surface tide becomes northward the tidal lee wave formed on the southern flank advects to the north of the crest. Concurrently, the frequency constituents forming the lee wave disperse and the dominant feature that radiates into the far field has a slope that corresponds much more closely to an M2 ray path (Figure 2.7d, between 25-35 km and shallower than 800 m). Comparison of Figure 2.7d and b shows downward phase propagation (northward flow progresses from the top to the bottom of the beam, also see the supplementary animation), consistent with upward energy radiation by the radiating components of the baroclinic response.

A tidal lee wave forms on the northern flank of the ridge during northward flow where the large barotropic transport and steep bathymetric slope cause the lee wave to have a maximum steepness close to the the steady lee wave limit (green dashed line, panel c). By panel d, the frequency constituents making up the lee wave have begun to disperse owing to their different phase speeds, and the slope is visibly reduced. In the timeseries from station C2, the turbulence arising from the southward radiating beam is characterized by its occurrence above the fast

bottom jet, between 08-13 h on 16 November 2012, and 08-12 h on 17 November 2012 (Figure 2.5 b). As was the case during southward tide, these isopycnals steepen and break as the tide progresses, becoming turbulent by panel d of Figure 2.7.

The lowest part of the tidal lee wave forms a strongly accelerated jet around 200 m thick at the crest of the ridge (Figure 2.7c). The jet separates downstream of the ridge crest at ∼600 m in panel c, shallowing to ∼500 m by panel d. The region around the separated jet is the site of significant turbulence, formed by the transition of the jet from super-critical to sub-critical in a hydraulic jump. Following *Winters and Armi* (2013), an assessment of the layer Froude number of the jet can be made by analogy to a discretely layered fluid, wherein the layer is supercritical if the phase speed of interfacial waves is less than the speed of the fluid in the layer. Using approximate values from the SADCP transects (Figure 2.3) for layer thickness ($l = 250\,\mathrm{m}$), and mooring for a mean layer speed ($\bar{U} = 1.2\,\mathrm{ms}^{-1}$) and mean layer stratification ($N = 3\,\mathrm{cph}$), we estimate the crest layer Froude number (Fr_l) of the jet to be ~ 0.9, supporting the idea that the jet is hydraulically controlled. The turbulence that arises in the hydraulic jump downstream is distinct from that in the tidal lee wave, occurring as a direct result of the hydraulic control of the jet at the crest of the topography, rather than from the non-linear steepening of the tidal lee wave. In contrast with the flows associated with the southward radiating beam, flows downstream of the separation point have positive vertical shear resulting in the generation of clockwise rotating vortices, or forward breaking. This turbulence is identifiable in the station data at depths below 500 m, where it persists for up to 6 h past peak northward from 10-14 h on 15 November at station C1, and at C2 from 12-18 h on 16 November (Figure 2.5d).

The key features described in this section are summarized in Figure 2.8, which shows the baroclinic across-ridge velocity just after peak flow (a time between panels c and d in Figure 2.7). With the depth mean velocity removed the baroclinic structure of the response is clear, and shows a steep internal wave beam corresponding to a southward radiating tidal lee wave on the northern flank of the ridge. Energy radiating northwards along an M2 characteristic started in a similar

steep tidal lee wave on the southern flank, whose frequency constituents have since dispersed or dissipated, leaving only the M2 characteristic clearly visible. We indicate the top of the hydraulically controlled layer with a bold contour in Figure 2.8, and assess the Froude number by calculating the mean velocity and stratification in the layer. The jet is subcritical upstream of the crest (A: $Fr_l = 0.8$), critical at B ($Fr_l = 1.0$), and supercritical downstream (C: $Fr_l = 1.5$; D: $Fr_l = 2.1$). There is some ambiguity in the definition of the jet, but the general result of a subcritical to supercritical transition is robust even if we use different criteria (e.g. defining the jet where speed is greater than $1/e$ of the peak jet velocity, or where the speed is greater than the depth mean speed). The hydraulically controlled northward bottom jet is associated with a hydraulic jump and dissipation where it separates from topography.

Time-series of depth integrated dissipation rates from stations C1 and C2 indicate that peak dissipation rates are associated with breaking and turbulence above the strong bottom current just after peak flow (Figure 2.5e). This turbulence arises both from the hydraulic jump and the direct breaking of the southward radiating tidal lee wave. At the mooring, however, peak dissipation rates are associated with passage of breaking tidal lee waves (slanted structures in timeseries, Figure 2.4c), as the turbulence associated with the hydraulic jump, though observed at the mooring, has decayed since its inception on the flanks.

Simulated flow during the weak beat of the tide exhibits poorer agreement with the observations, as it is during this time that three-dimensional effects dominate the characteristics of the flow (Figure 2.7e - h). This phase of the tide is dealt with more completely in M15b, and we do not discuss it further here.

2.4.2 Modeled time-mean spatial structure of turbulent dissipation rate at the ridge crest

Whilst the generation of turbulence by the hydraulic jump occurs just after peak tidal flow on the flanks of the ridge, turbulence generation by the breaking tidal lee wave occurs higher in the water column, reaching almost to the surface at station C2 (Figure 2.5b). Observed time mean dissipation rates over 24 h at

stations C1 and C2 are 0.64 and 2.8 $\mathrm{W\,m^{-2}}$, whilst concurrent dissipation rates at the mooring are 1.8 and 2.6 $\mathrm{W\,m^{-2}}$. A comparison of C1 and C2 normalized by the simultaneous dissipation rates at the mooring indicate that there is around 3x more dissipation at C2 compared to C1, even when the change in the dissipation measured at the mooring during each of the stations is accounted for. Stations C1 and C2 are approximately 1 km apart, indicating strong gradients in time-averaged dissipation rate close to the ridge crest.

Maps of time-averaged model dissipation rates (averaging over 5 h intervals just after peak flow) are presented in Figure 2.9, and show reasonable agreement with observations in both their spatial distribution and order of magnitude. Elevated dissipation rates are present throughout the water column around the ridge crest. At shallow depths the turbulence is driven by breaking in the tidal lee wave, whilst at depth on the flanks of the ridge the turbulence arises mainly from transient internal hydraulic jumps downstream of jet separation. Depth integrated time averaged dissipation rates show peaks on the flanks of the ridge, approximately at the location of station C2, where both processes contribute to the total turbulent dissipation. Depth integrated dissipation rates averaged over the full 24 h (not shown) have two peaks, one on each flank, with reduced depth integrated dissipation rates at the crest. Integrating the 24 h-mean dissipation rate within ± 10 km of the ridge crest gives a total, tidally averaged dissipation rate over the ridge of $6\,\mathrm{kW\,m^{-1}}$. For comparison, AL03 estimate a dissipation rate of $0.1\,\mathrm{kW\,m^{-1}}$ for the section of ridge that they examined in the open ocean (see Figure 2.1c), an order of magnitude smaller than that measured at our coastal channel site. The relative energetics of the two sites will be discussed in Section 4d.

2.4.3 Frequency constituents at the crest

Theory (*Bell*, 1975) and model output discussed in Section 4a suggest that harmonics of the forced frequencies are important for the development of the ridge-top flow, determining the structure of the tidal lee wave. To quantify this using the observations we examine power spectra of inferred vertical velocities at the 1 Hz temperature loggers on the mooring (Figure 2.10). The computation of spectra on

an isopycnal, rather than in a fixed depth coordinate system reduces the impact of fine structure contamination arising from the vertical advection of a stepped temperature profile past the sensors (*Phillips*, 1971). The mean densities observed by each sensor over the course of the deployment were used to form a set of reference isopycnals, whose vertical displacement was computed for all times. Small density inversions were occasionally present between sensors, and these were removed before calculating isopycnal depth by linearly interpolating over adjacent sensors. The vertical velocity is the time derivative of isopycnal depth, under the assumption that the contribution to the time derivative from the horizontal advection of features past the sensors was relatively small. The drifting of isopycnals into and out of the range of the mooring meant that some of the highest and lowest displacement records contain too many gaps to be used to compute spectra. However a nearly continuous record was obtained for isopycnals at intermediate depths, and it is these that are used to compute the spectra shown in Figure 2.10.

Spectra were computed for each isopycnal in 5 overlapping 4 day records which were then averaged to produce a single frequency spectrum. Pairs of adjacent isopycnals were averaged together to form seven spectra associated with a range of mean isopycnal depths observed at the mooring. Peaks are present at all depths at 1-4 cpd but are increasingly significant away from the surface, with harmonics at 3 and 4 cpd dominating the spectrum. Though some of this variance is likely to have arisen from the kinematic effect of advecting the wavefield past a fixed sensor, the strong signal indicates a contribution from free waves at these frequencies. The depth structure of each of these frequencies is explicitly shown in Figure 2.10b. The subinertial D1 constituent contributes to the velocity and displacement variance at depth, but decays rapidly away from the bottom consistent with a bottom trapped, subinertial response (M15b). Superinertial frequencies D2, D3 and D4 have variance distributed throughout the water column, consistent with a radiating response. Distinct peaks are present in D3 below 250 m, and D4 above 300 m. Displacement spectra (not shown) are redder, as the Fourier amplitudes of displacement and vertical velocity are related by frequency. However, prominent harmonics are still present, with most displacement energy in D1 and D3 at depth

(Figure 2.10c). Modeled spectra (not shown) have qualitatively similar features, with significant peaks at D3 and D4.

2.4.4 The radiated wave field: energetics and frequency constituents

To assess the amount of energy at harmonics of the forced frequencies in the far field we evaluate the flux of baroclinic wave energy at the forced and harmonic frequencies at -20 km (south) and 20 km (north) in the model, during the final 25 h of the simulation. Baroclinic flux is defined as

$$F = \frac{1}{T}\int_0^T \int_0^h p'u' \,\mathrm{d}z \,\mathrm{d}t, \tag{2.6}$$

where u is the along-channel velocity, p is the pressure, T is the period of the tidal constituent, and h is the depth ocean. Primes indicate that the depth mean and time mean components of the fields have been removed (c.f. *Nash et al.* (2005)). In an Eulerian time-series such as that obtained by a mooring, or CTD station, the generation of kinematic harmonics from the advection of a wavefield past a fixed sensor are extremely difficult to correct for, however in a model it is possible to estimate the influence of this advection on the computed fluxes. As such, we compute wave fluxes measured both in an Eulerian frame (equivalent to a fixed mooring), and a Lagrangian frame, advected by the background tide and consequently capturing only the dynamic effects arising from freely propagating internal waves. The harmonic components of the timeseries in each frame of reference are computed by a least squares fit for amplitude and phase to a sum of sinusoids at frequencies corresponding to D1, D2, D3, D4 and D5.

Despite strong advective velocities (0.2-0.3 $\mathrm{m\,s^{-1}}$) there is negligible difference between the fluxes computed in either frame of reference, indicating that the generation of spurious harmonics in the timeseries is small. As a result we present only the fluxes calculated in an Eulerian frame (Figure 2.11). Harmonics (D3, D4 and D5) account for up to 30 % of the generated flux to the north of the ridge, and 10 % of the flux to the south. Given the high dissipation rates close to the ridge crest these harmonic flux fractions represent a lower bound on harmonic generation

and energy content very close to the crest. Total fluxes in each frame are similar, with a net northward flux of $13\,\mathrm{kW\,m^{-1}}$, and southward flux of $2.6\,\mathrm{kW\,m^{-1}}$. AL03 measured a northward flux of $7\,\mathrm{kW\,m^{-1}}$ much further west along the ridge, in the open ocean (see Figure 2.1a). *Llewellyn Smith and Young* (2003) show that internal tide flux generation by a tall, knife edge ridge depends on the square of the tidal amplitude (amongst other things), as such the relatively smaller northward flux at an open ocean location can be understood from the smaller tidal amplitudes (between 0.05-0.1 $\mathrm{m\,s^{-1}}$) away from the coast. Nevertheless, our fluxes support the conclusions of AL03 that the Mendocino Ridge is an important source of internal tide energy in the north-eastern Pacific.

From our model results we infer a near-ridge dissipation rate of $6\,\mathrm{kW\,m^{-1}}$, and a total outgoing flux of $15.6\,\mathrm{kW\,m^{-1}}$. If we assume steady state dynamics, the conversion of energy from barotropic to baroclinic motions, C is given by (*Kang and Fringer*, 2012):

$$C - \nabla \cdot \mathbf{F} = \epsilon \tag{2.7}$$

where ϵ is the dissipation rate of baroclinic energy. As such, we infer a total near-ridge conversion of $21.6\,\mathrm{kW\,m^{-1}}$. *St Laurent et al.* (2002) define the local dissipation efficiency, q, as the fraction of energy extracted from the barotropic tide that is dissipated locally, and from our simulation we infer

$$q = \frac{\text{local dissipation}}{\text{conversion}} \times 100\% = 28\,\% \tag{2.8}$$

In contrast, at the deep ocean site of AL03 they infer a near-ridge dissipation rate of $0.1\,\mathrm{kW\,m^{-1}}$ and a total outgoing flux of $7\,\mathrm{kW\,m^{-1}}$, giving $q = 1\,\%$. The significant difference in these values at the two locations along the ridge indicates the importance of regional factors in determining local energy budgets. At our coastal location, not only is the barotropic tide stronger than in the deep ocean, but the trapped subinertial tidal constituent strongly affect the dynamics of our observed flow. As this constituent cannot radiate it contributes to nearfield mixing without contributing to the flux, giving a much higher local dissipation efficiency than at a location where there are no trapped tides, or where the trapped component may be much less energetic. It is these types of process which complicate attempts

to parameterize nearfield tidal dissipation, and this will be discussed in the next section.

2.5 A general relation between turbulent dissipation rate and tidal flow speed

One of the earliest attempts to parametrize tidal dissipation in the ocean was by *Taylor* (1919), who assumed the energy was dissipated in a turbulent bottom boundary layer which exerts a quadratic bottom drag on the flow. In this case the dissipation of tidal energy is proportional to the cube of the barotropic tidal speed, with a fixed drag coefficient. This type of bed friction accounts for most of the dissipation of the barotropic tide in shallow seas, however it accounts for only about 10% of the dissipation in the deep ocean (*Green and Nycander*, 2013). Abyssal dissipation of the barotropic tide is strongly enhanced over regions of rough topography (*Egbert and Ray*, 2000), and is thought be driven both by internal wave generation and the type of near-topographic turbulence described in this paper. *Klymak et al.* (2010a) provide a parametrization for the amount of energy dissipated directly to turbulence close to tall topography wherein, like *Taylor* (1919),

$$D \propto U_0^3 \tag{2.9}$$

where D is the total near-topographic dissipation rate averaged over one tidal cycle, and U_0 is the tidal amplitude of the tide in the deep ocean away from topography. Unlike *Taylor* (1919), the "friction coefficient" in this abyssal parametrization is variable, depending on parameters including bathymetric height, stratification and tidal frequency. Motivated by this prediction, we use our 12 day time-series from the mooring to assess the relationship between flow speed (U_c) and depth integrated dissipation rate (ε) at the center of the channel. We are unable to unambiguously determine U_0 for this site as much of the barotropic transport is associated with trapped waves, rather than an open ocean tide. Cross-correlating hourly averages of depth mean flow speed and dissipation rate shows a peak in correlation when the dissipation time-series lags the flow speed by 3 h, as such we lag the dissipation

rate time series before performing the fits. We then perform a linear least squares fit of the average depth mean flow speeds and dissipation rates at the center of the channel over 24 h periods as the tide progresses from spring to neap (blue line, Figure 2.12). Due to the knock-down of the mooring during periods of strong current, flow speeds were calculated as depth means below 250 m. Depth integrated dissipation rates are computed from all instruments, though computing a depth mean below 250 m makes no noticeable difference to the fits shown. The fit is performed using the logarithm of the dissipation rates and flow speeds to a linear model with the slope as a free parameter. For 24 h averages, we find that the dissipation rate is proportional to U_c^2, with 60 % of the variance being explained by the model. We note that this R^2 is only just significant at the 95% level with a sample size of 11 points. Comparing the 24 h peak, rather than mean, flow speeds causes the slope to be reduced to $U_c^{1.6}$, with the variance explained increasing to 80% (black line, Figure 2.12).

Several factors make the application of *Klymak et al.* (2010a) to this data set uncertain, perhaps the most important relating to the spatial distribution of time averaged turbulence at the crest of the ridge. If, in a time average, the measured dissipation rate at the mooring is not linearly proportional to the total near-field dissipation rate then it is plausible to expect a systematic bias in the comparison of dissipation rate vs. flow speed. Modeled dissipation rates show that the depth integrated dissipation rate is not constant across the ridge (Figure 2.9), and it seems likely that the spatial distribution of the turbulence may change as the tidal amplitude varies through the spring-neap cycle. Additional uncertainty arises because the observations involve two dominant frequencies while the parametrization was formulated for a single frequency tide. The inherent nonlinearity of the response suggests that the dissipation should not be the sum of the dissipation of each constituent separately, and as such we have considered the tidal peak and average flow speeds of all constituents together in order to form these fits. Finally, these observations were obtained in a channel, where three-dimensional bathymetry strongly influences the flow. One such influence is the generation of trapped topographic waves by the subinertial (K1) tidal component, which are responsible for bottom

enhanced K1 transports close to the ridge (M15b). Such phenomena are beyond the scope of a parameterization such as that proposed by *Klymak et al.* (2010a).

2.6 Summary

We observe energetic, time-dependent turbulence in a channel at the crest of the Mendocino Ridge, which we interpret with the aid of a high resolution, 2.5-dimensional numerical model. This site is of interest due to the combination of small topographic Froude number with large excursion length, and a strong diurnal inequality which modulates near-field turbulence.

The constructive superposition of trapped and radiating internal waves at both the forcing frequencies (K1 and M2) and their harmonics create tidal lee waves: large amplitude beam-like features that form during strong flow phases of the tide and are advected past the mooring and CTD stations as each strong tide relaxes, giving rise to striking flow patterns in the time-series. From model output we identify two distinct processes which generate turbulence in close vicinity of the ridge crest. The first is via steepening and convective instability within the beam of the tidal lee wave which generates turbulence above a bottom intensified, hydraulically controlled jet. The second is from the formation of a hydraulic jump like feature on the lee side past the jet separation point. These processes are identified in the observed time-series, where overturns associated with each process occur at different phases of the tide and in conjunction with different velocity structures.

Observations presented here demonstrate the importance of the alternating constructive and destructive super-positions of the K1 and M2 baroclinic responses on determining the timing and intensity of near-ridge turbulence. Higher harmonics of the forcing frequencies contain significant energy, and the modeled flow explicitly illustrates their influence, steepening the near-ridge internal tide beam beyond what would be expected for a single fundamental frequency wave. Long excursion length flows such as these generate phenomena that lie somewhere between the acoustic and steady lee wave limits of *Bell* (1975), and are not fully

described by either extreme.

24 h averages of flow speed and dissipation rate at the center of the channel have a power law relation whose exponent is less than that proposed in parameterizations for superinertial tidal mixing near topography (*Klymak et al.*, 2010a). Bias present in estimating the spatial and temporal mean dissipation rates by a single time-series at the center of the channel may influence this result, as well as the effects of three-dimensional bathymetry and a multifrequency tide (including a subinertial trapped component).

A comparison of station data collected in the channel to that collected at the ridge crest adjoining the channel demonstrates that similar processes generate turbulence at both locations. However, subinertial trapped waves generate strong, bottom intensified flows that pass through the channel and generate more turbulence than over the ridge. In contrast to observations reported by AL03 further west along the ridge, the local dissipation efficiency at the shallower channel site discussed in this paper is large, with 28% of the energy extracted from the barotropic tide dissipated in the nearfield. In the vicinity of the channel we find that peak depth integrated dissipation rates in the channel are 100× greater than those over the ridge, suggesting that this small channel may play a disproportionately large role in regional energy budgets. It is plausible that other such "small scale" features may be of primary importance in quantifying the magnitude and distribution of dissipation and mixing arising from the interaction of the surface tide with a feature such as the Mendocino Ridge.

2.7 Acknowledgements

Ship time was provided through the UC Ship Funds program. Shaun Johnston, Uwe Send and Janet Sprintall generously loaned instrumentation. At sea help with SADCP data processing was provided by Jules Hummon. The authors thank Capt. Dave Murline and the crew on the R/V Melville for their technical competence and proactive help at sea. Field work was greatly aided by the hard work of Paul Chua and 10 UNOLS volunteers, who worked cheerfully and tirelessly

under occasionally difficult sea conditions to obtain this dataset. RCM thanks Bill Young for insightful conversations in relation to this work. RCM is funded by the Office of Naval Research. We thank Louis Gostiaux and two anonymous reviewers for their comments which have improved this work.

Chapter 2, in full, has been submitted for publication of the material as it may appear in the Journal of Physical Oceanography, 2015, Musgrave, R C; MacKinnon, J A; Pinkel, R; Waterhouse, A F; Nash, J. The dissertation author was the primary investigator and author of this paper.

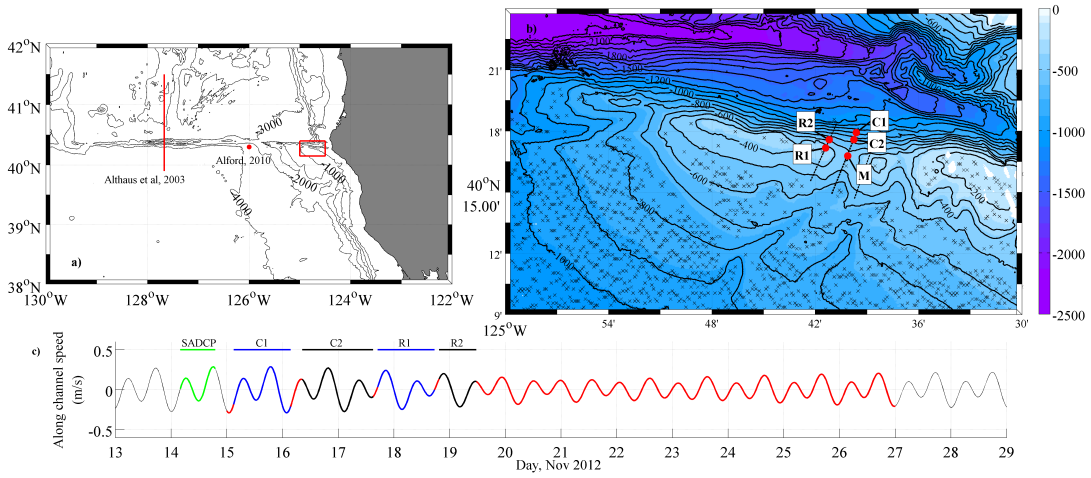

Figure 2.1: a) Regional map showing the Mendocino Ridge and continental shelf of the west coast USA, and locations of previous studies in the area. b) Stations C1, C2, R1 and R2 were LADCP/CTD stations in the channel (C) and ridge (R). A subsurface mooring was in place at M. Crosses represent regions of M2 near-critical slope at depths shallower than 800 m. c) Timeseries shows TPXO predicted along-channel component of the barotropic flow during observations. Red line is the period mooring was in place; green line indicates time of SADCP transects; alternating blue and black lines are times of station time series C1, C2, R1 and R2.

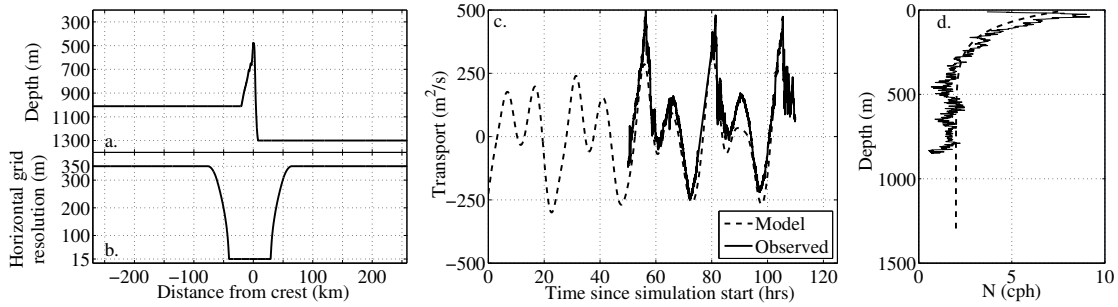

Figure 2.2: a) Model bathymetry b) Horizontal grid resolution c) Model volume transports (dashed line) compared to observations (solid line) through stations C1 and C2. d) Model stratification (dashed line) compared to mean stratification (solid line) at station C1.

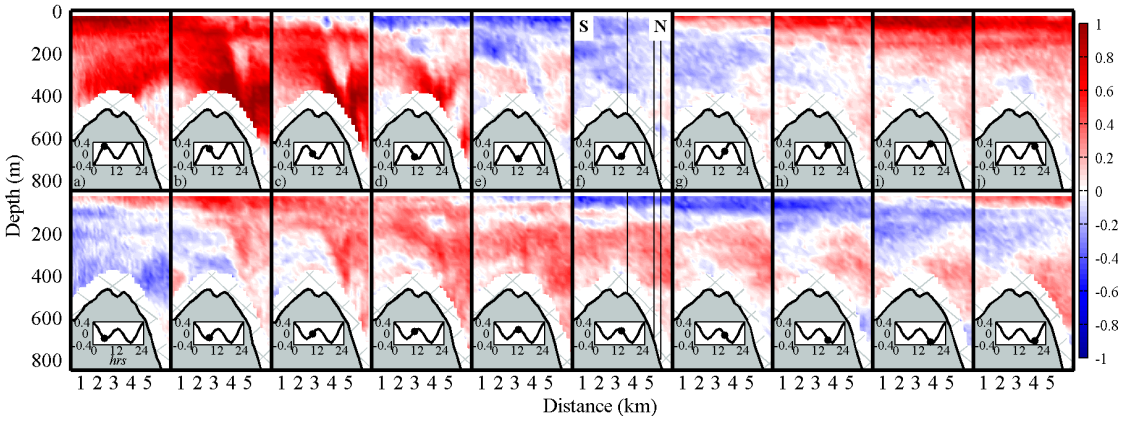

Figure 2.3: SADCP snapshots of velocity rotated into (upper panel) along- and (lower panel) cross-channel components through the center of the channel as the tide progresses over around 13 hours. Insets show TPXO predicted barotropic speeds ($\mathrm{m\,s^{-1}}$), with dots indicating the time of the snapshot. Vertical lines in panels f show locations of mooring (M), and CTD-LADCP stations C1 and C2. Note the different nature of adjacent northward tides in panels b and i.

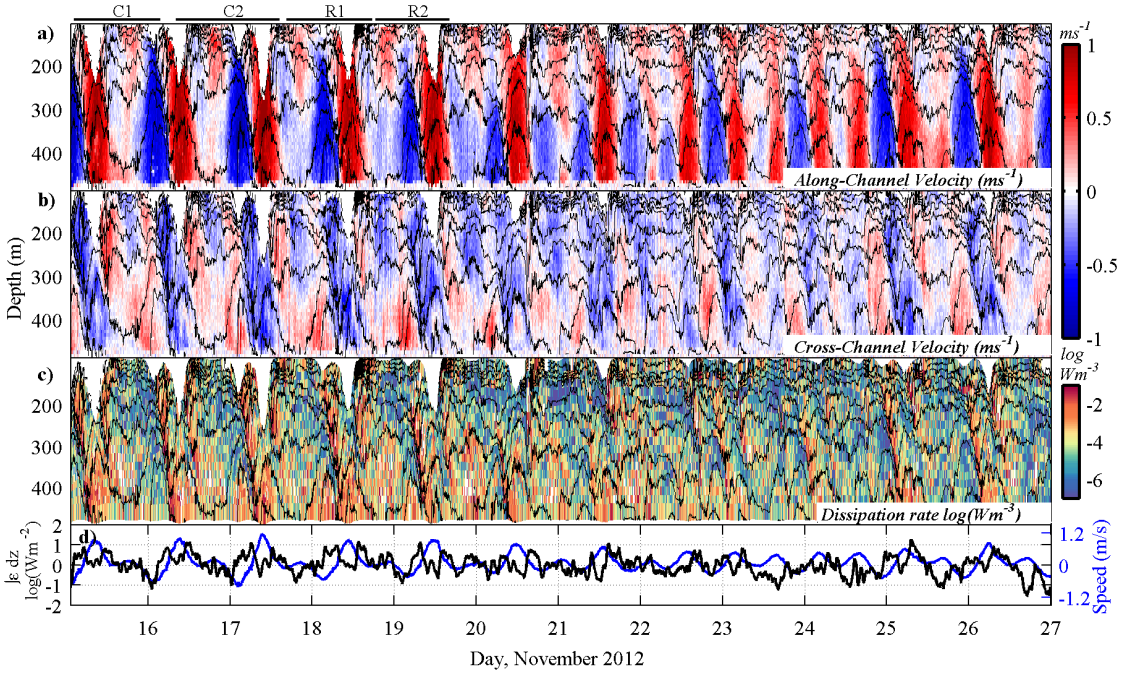

Figure 2.4: Mooring timeseries: Upper three panels are a) along-channel velocity, b) cross-channel velocity, c) turbulent kinetic energy dissipation rate (ε) (color), isopycnals contoured. Lowest panel is d), depth integrated dissipation rate (black) and depth mean along-channel speed (blue).

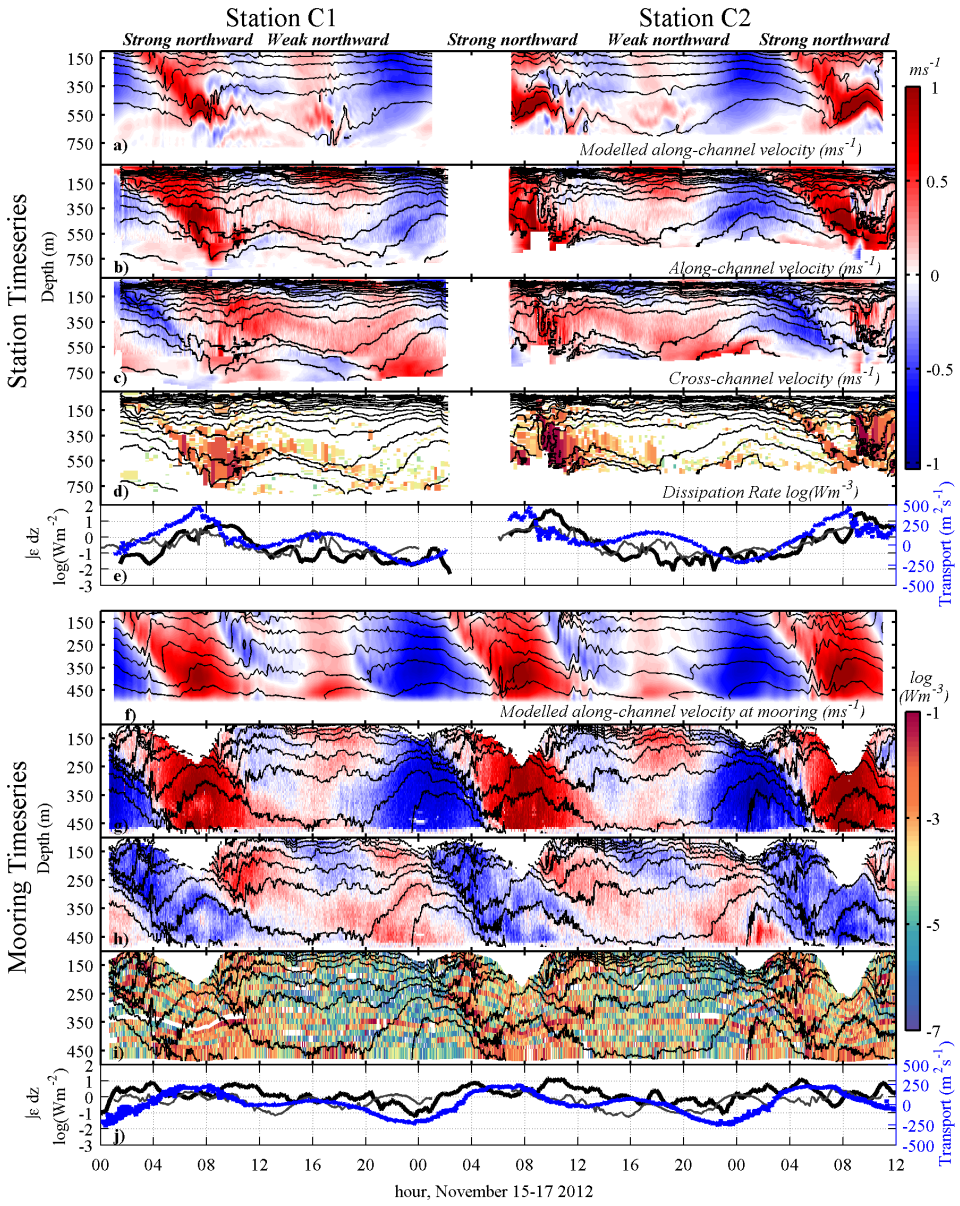

Figure 2.5: Upper panels are station timeseries: a) Modelled along-channel velocity (color) and isopycnals (contoured); b) and c) observed along- and cross-channel velocity (color) and isopycnals (contoured); d) turbulent dissipation rates (ε) (colored) and isopycnals (contoured); e) depth integrated turbulent dissipation rates (black) and velocities (blue). Modeled depth integrated dissipation rates are thin dark grey lines. Lower panels are as for upper, but at the mooring.

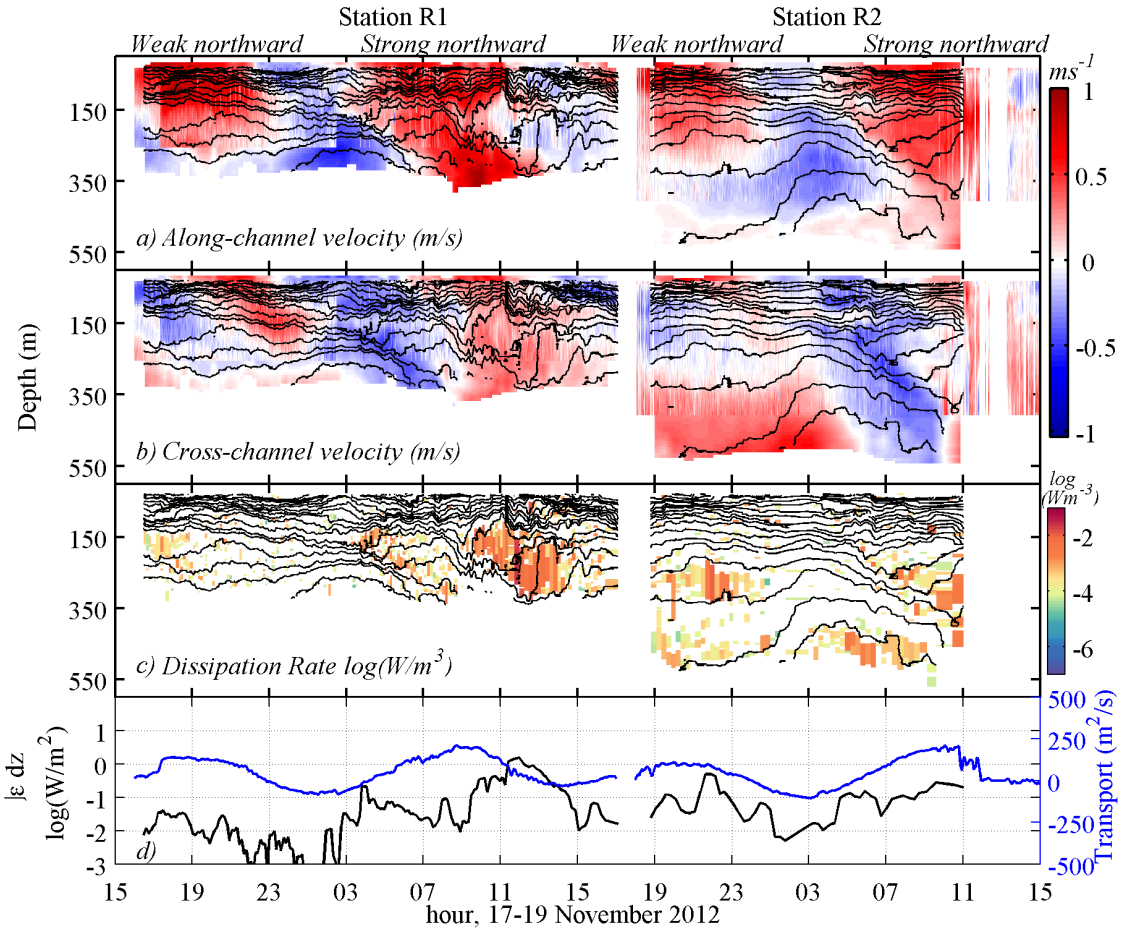

Figure 2.6: Station time series from R1 and R2. a) Along channel velocity (color) and isopycnals (contoured), b) cross channel velocity (color) and isopycnals (contoured), c) turbulent dissipation rate (ε) and isopycnals (contoured), and d) depth integrated dissipation rate (black) and velocity (blue).

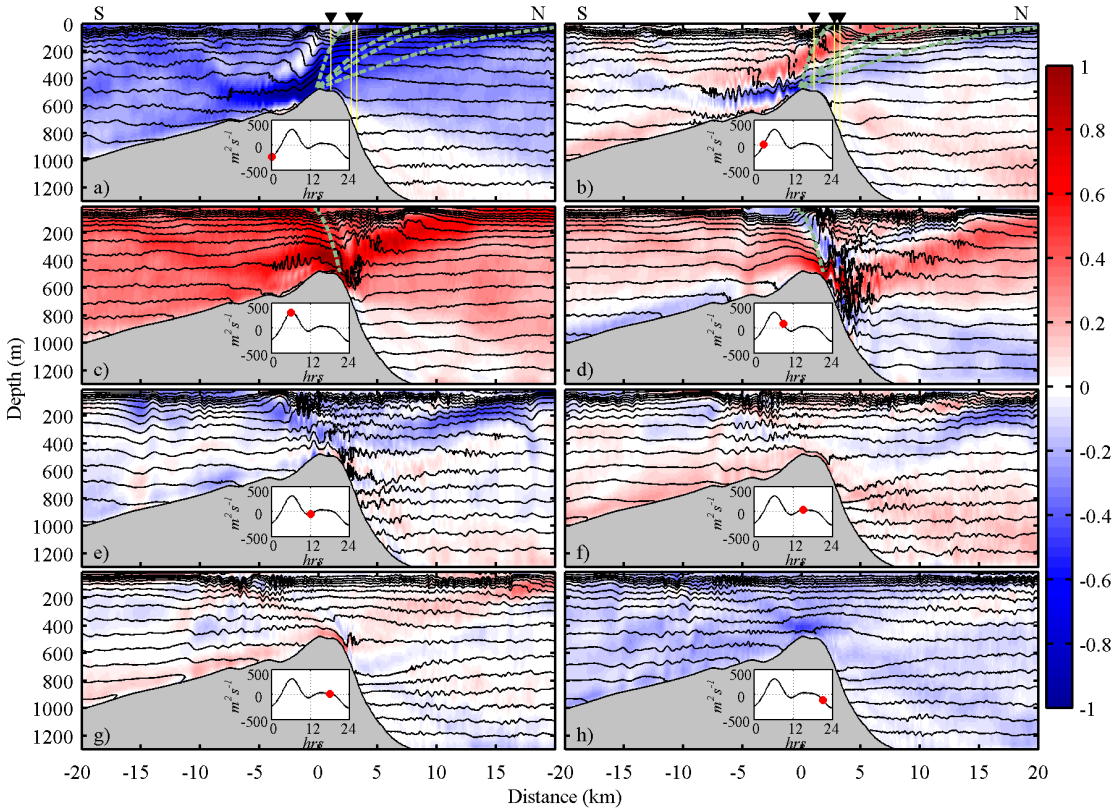

Figure 2.7: Snapshots of simulated velocity (color) and isopycnals (contours) over 24 hr. Mooring and station locations C1 and C2 are indicated above panels a and b by small black triangles. Insets show modeled transport time-series ($m^2 s^{-1}$), and red dots indicate the time of each snapshot after hour 74 of the simulation. Characteristics for the D2, D3, D4 and the steady lee wave response are shown in panels a and b (in increasing steepness).

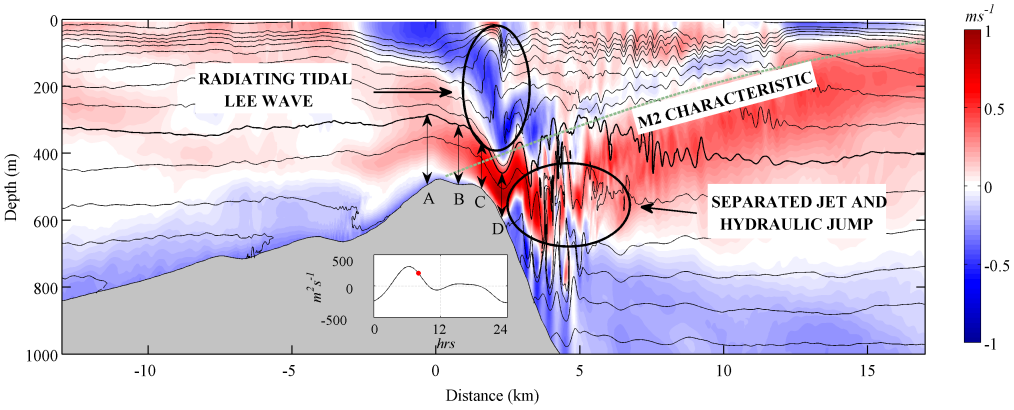

Figure 2.8: The generation of tidal lee waves, internal tides, and hydraulic jumps at the ridge crest. Color is baroclinic across-ridge velocity (with the depth mean northward flow removed), black contours are isopycnals. Thicker isopycnal defines hydraulically controlled layer, with layer Froude numbers A: $Fr_l = 0.8$; B: $Fr_l = 1.0$; C: $Fr_l = 1.5$; D: $Fr_l = 2.1$ indicating a subcritical to supercritical transition at the crest.

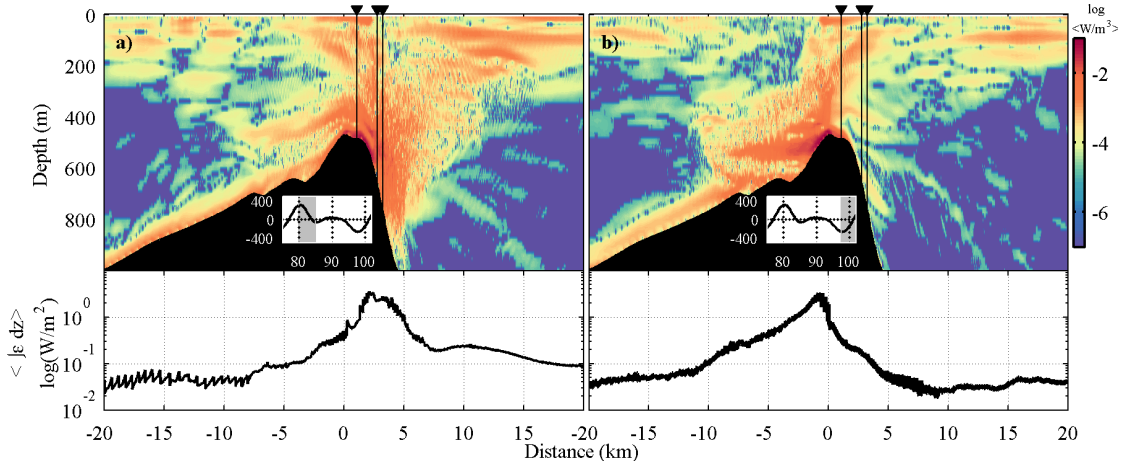

Figure 2.9: Maps of 5hr averages of modeled dissipation rate at the ridge crest just after peak a) northward, and b) southward flow. Insets show barotropic transport time-series (ms^{-1} vs model hour), shaded region indicates averaging interval. Triangles and black lines indicate locations of mooring, station C1 and station C2.

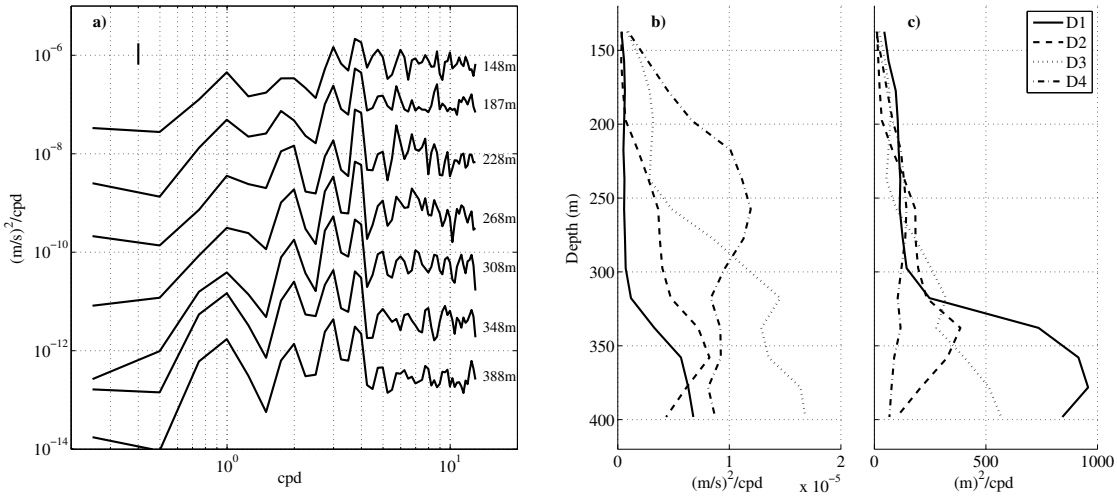

Figure 2.10: a) Power spectra of vertical velocities on isopycnals inferred from thermistor records on mooring in center channel. Spectra are offset by 0.08 $(m/s)^2/cpd$ for each depth, with mean isopycnal depths shown. 95% confidence level in upper left corner. b) Amplitudes of diurnal (D1), semi-diurnal (D2) and harmonics (D3 and D4) as a function of mean isopycnal depth. c) as b) but for displacements rather than vertical velocities.

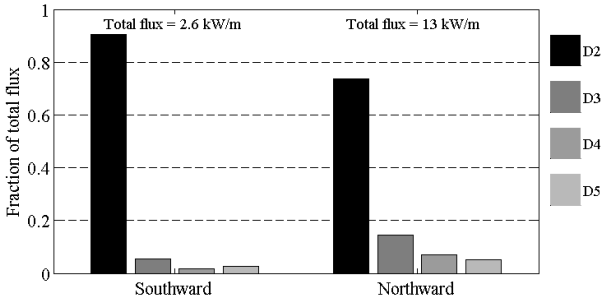

Figure 2.11: Modeled fluxes at D2 and harmonic frequencies at x = -20 km (southward) and x = 20 km (northward).

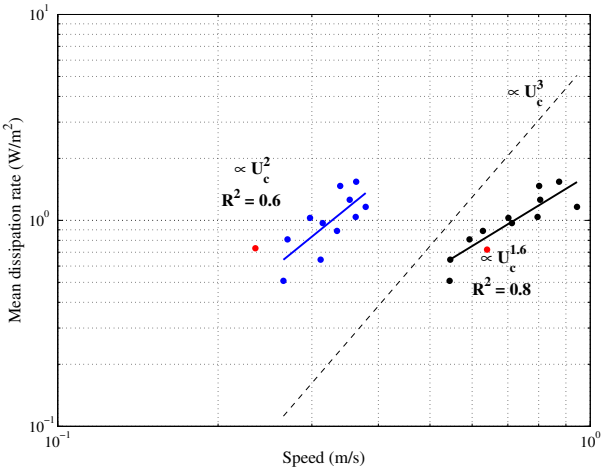

Figure 2.12: 24hr mean (blue) and peak speed (black) vs 24hr mean depth integrated dissipation rate lagged by 3hr. Fitted slopes show a power law relation of 2 and 1.6. Dashed line shows $D \propto U_c^3$. Modeled mean dissipation rate and speeds at channel shown in red.

Chapter 3

The influence of diurnal trapped tides on near-ridge top turbulence at the Mendocino Ridge: Observations and Modeling.

Shipboard measurements of velocity and density were obtained in the vicinity of a small channel in the Mendocino Ridge. Measured daily inequalities in transport are much greater than those predicted by TPXO7.2, with the strongest transport associated with full depth flows, and the weakest with shallow, surface-confined flows. A regional numerical model of the area finds that the subinertial K1 (diurnal) tidal constituent generates topographically trapped waves which propagate anticyclonically around the ridge, and are associated with enhanced near-topographic K1 transports. The interaction of the trapped waves with the M2 (semidiurnal) surface tide produces a baroclinic tidal flow that is alternately surface confined and full depth. Full depth flows are associated with the generation of a large amplitude tidal lee wave on the northward face of the ridge, while surface confined flows are largely nonturbulent. The regional model demonstrates that nearfield dissipation over the entire ridge is diurnally modulated, despite the larger amplitude of the M2 tidal constituent, consistent with field observations.

Thus, it is the trapped wave that modulates near-field dissipation and mixing at this location. The effect of the trapped wave on regional energetics is to increase the fraction of converted barotropic-baroclinic energy that dissipates locally.

3.1 Introduction

The interaction of the barotropic tide with topography gives rise to a range of phenomena, including the generation of an internal tide which propagates large distances across the ocean, transferring energy out of the surface tide where it is generated and dissipating it where it breaks or shoals. Where the tide has a frequency lower than the local Coriolis frequency, internal tides are unable to radiate and instead may take the form of topographically trapped waves, leading to locally enhanced subinertial tidal transports (*Huthnance*, 1974; *Chapman*, 1989; *Padman et al.*, 1992). The generation of turbulence and mixing by internal tides, trapped or otherwise, is important on regional and global scales, as it modifies water masses and influences the stratification of the deep ocean. Close to topography turbulence has been observed to arise from breaking tidal lee waves and hydraulic jumps, as the stratified ocean accelerates over obstacles (*Klymak et al.*, 2008; *Nakamura et al.*, 2010). However the fraction of energy that dissipates via processes such as these in the nearfield, compared to the total barotropic-baroclinic conversion is widely variable, ranging from 15% at Hawaii, (*Carter et al.*, 2008), to 40% at the Luzon Strait (*Alford et al.*, 2015) and up to 70% in the high latitude Bering Sea (*Tanaka et al.*, 2013). *Müller* (2013) found that 30% of the energy in the global diurnal barotropic tide dissipates above 30° where it is subinertial and cannot radiate, suggesting that high latitude locations may generally be more dissipative in the nearfield than low latitudes. Understanding the processes that lead to this regional variability in tidal mixing is an important problem as these small scale phenomena cannot be resolved in global climate models, and as such their effects must be parameterized (*Green and Nycander*, 2013).

The nearfield dissipation characteristics of subinertial and superinertial baroclinic tides were considered in a numerical study by *Tanaka et al.* (2013)

in the Bering Sea. At this location K1 is subinertial and M2 is superinertial. They found that dissipation associated with the K1 constituent was localized near the shelf-break, whilst dissipation associated with M2 also occurred high in the water column above the shelf-break and was associated with the freely radiating internal tide. Idealized two-dimensional simulations of tidal flow over a Gaussian ridge support this result, showing that mixing in subinertial tidal flows arises through hydraulic jumps on the flanks of topography, while mixing in superinertial tidal flows also occurs through breaking tidal lee waves aloft (*Musgrave et al.*, 2015c). However, the inherent nonlinearity of phenomena that lead to turbulence suggests that the presence of more than one tidal constituent may influence the magnitudes and spatial structure of nearfield turbulence in a way that is not simply a superposition of the dissipation associated with individual constituents.

In an earlier study we considered the processes leading to turbulence at the Mendocino Ridge where, as in the Bering Sea, the subinertial diurnal (K1) constituent generates a trapped internal tide, and the superinertial semidiurnal (M2) constituent generates a freely radiating tide (*Musgrave et al.* (2015b), hereafter M15). In and around a relatively small channel incising the crest of the ridge we found that tidally driven lee waves and hydraulic jumps formed on the flanks of the ridge downstream of the channel, leading to peaks in depth integrated dissipation rates of up to $60\,\mathrm{Wm}^{-2}$. Motivation for the present work arose from the observation that tidal lee waves only formed once per day after the strongest of the daily peaks, despite the presence of two daily peaks. During the weaker beat of the tide, tidal transport was accommodated in a surface layer, with largely quiescent flow at depth close to topography - a vertical structure that is not predicted for single frequency tidal flows at any latitude. Here, we study the dynamics that leads to the dramatically different characters of adjacent peak tides by running a regional tidal model for the area, and studying the interaction of the tidal constituents at the ridge crest. We find that this interaction has a profound influence on the processes leading to turbulence, with implications for the regional tidal energy budget.

The remainder of this paper is divided into 4 parts. In Sections 2 and 3 we describe the observations, and regional model used to interpret the observations,

respectively. In Section 4 we discuss the dynamics of the tidal flows through the channel, and over the ridge, and in Section 5 we summarize our findings.

3.2 Observations

In November 2012, a series of ship-based measurements of velocity and density were obtained in the vicinity of a small channel incising the crest of the Mendocino Ridge in the eastern Pacific. The site is located where the ridge intersects the North American continental shelf at a latitude of around 40° (Figure 3.1). Observations are described in detail in M15, and here we provide a summary with an emphasis on the measurements that motivate the rest of the paper. Four 24-30 hr stations were performed, two stations to the north of the channel (C1 and C2), and two shallower stations atop the ridge crest on the west flank of the channel (R1 and R2). At each location, the ship held station while a Conductivity-Temperature-Depth (CTD) and Lowered Acoustic Doppler Current Profiler (LADCP) package was repeatedly yo-yoed the full depth of the water column. In this manner continuous depth-timeseries of velocity and density were obtained. Isopycnals and along-channel velocities (rotated clockwise 17° from north) are shown in color in the insets in Figure 3.1b)i. (R1 and R2) and ii. (C1 and C2). The diurnal inequality is especially clear in the channel where alternate northward tides are either surface confined or extend to full depth. A similar pattern occurs over the adjacent ridge, though peak transports and dissipation rates are smaller (not shown). Measured turbulent dissipation rates in the channel peak by two orders of magnitude just after the full depth flows, but have no peak during the surface confined flows (not shown).

A mooring was in place for 10 days at the center of the channel, and the along-channel velocities (color) and isopycnals (contoured) are shown in Figure 3.2b. As for the stations on the flanks of the ridge, the diurnal inequality in the channel is strong, and its signature is emphasized in the depth integrated along-channel transports shown in blue in Figure 3.2c. During the strong beat of the tide, transports reach up to $500\,\mathrm{m^2 s^{-1}}$, corresponding to a depth averaged velocity of

$1\,\mathrm{ms}^{-1}$. Tidal transports at this location predicted by the TPXO West Coast USA tidal model (*Egbert and Erofeeva*, 2002), hereafter referred to as TPXO, are shown in the same panel in black, and demonstrate good agreement with the phase of the flows but poor agreement with the amplitude, especially during the strong beat of the tide. TPXO uses satellite altimetry to constrain solutions to the shallow water Laplace Tidal Equations on a $1/30^\circ$ bathymetric grid (about 3 km at this latitude).

Depth integrated dissipation rates were estimated from the timeseries of 1 Hz temperature loggers spaced approximately every 20 m along the mooring following the method outlined in *Zhang and Moum* (2010). These are shown in blue in Figure 3.2d, where peaks in dissipation rates occur just after the largest southward and northward flows of the day, and are associated with the advection past the mooring of tidal lee waves and hydraulic jumps that form on the southern and northern flanks of the ridge. These phenomena were explored in detail in M15 with the aid of a high resolution, two-dimensional, nonhydrostatic model. During the weak beat of the tide, transports through the channel are much smaller, and depth-timeseries from the stations and mooring illustrate a distinctly different nature to the baroclinic flow (Figure 3.2b). While the strong beat of the tide is associated with full depth, bottom intensified flows, the transport during weak northward flows is accommodated almost entirely at the surface, with weak, almost reversed flows close to the crest of the ridge. A naive two-dimensional analysis based only on the barotropic transport would suggest that lee waves should form even during the weak beat of the tide, simply having a shorter vertical scale corresponding to the trapping of slower (higher) vertical modes at the ridge crest (*Farmer and Smith*, 1980). However, during this phase of the tide, no tidal lee waves or hydraulic jumps form, and it is clear that the flow does not simply correspond to a weaker version of strong northward flows. Understanding the baroclinic structure of this weak beat of the tide is one of the main research questions that we address in this paper, and answering it involves an understanding of the regional scale flows in the vicinity of the ridge crest.

3.3 Numerical Simulations

To try to understand the distinct characters of adjacent northward tides, we used the hydrostatic MITgcm (evolved from *Marshall et al.* (1997)) to run three different regional tide simulations for the vicinity of the observations using the barotropic flows predicted by TPXO. In the first simulation we forced the model with only the K1 constituent of the tide (the *K1-only* run); in the second we forced only with the M2 constituent (the *M2-only* run); and in the third we used both the K1 and M2 tidal constituents to generate the model forcing (the *K1+M2* run). We used a realistic stratification, and the domain was approximately 200 × 200 km large with the outer 30 km of ocean boundary constituting the forcing/sponging region. Within this region, the model was forced by nudging the variables towards the TPXO predicted barotropic values using expressions such as

$$\mathcal{G}_u = \frac{1}{\tau}(u_{ij} - u_{TPXO}), \tag{3.1}$$

where $\mathcal{G}_u$ is the forcing applied to the x-momentum equation, u_{ij} is the horizontal velocity at that grid point, u_{TPXO} is the TPXO predicted value, and τ is a timescale that takes a value of 4 hr at the inner boundary, and 10 min at the outer boundary. In this manner the flow is sponged increasingly strongly as baroclinic signals propagate outwards, without sudden rapid damping that could generate reflections back into the domain. Grid resolution in the domain interior is 300 m in the horizontal, and 20 m above 2000 m depth in the vertical, telescoping to 46 m at depth. Model bathymetry is taken from 70×90 m gridded multi-beam bathymetry extracted from the NOAA database (http://maps.ngdc.noaa.gov/viewers/multibeam/). The full model domain is shown in Figure 3.1a, with the detailed bathymetry of the near-channel region shown in Figure 3.1b. The *M2-only* and *K1-only* simulations were spun up for nine and four periods respectively before any analysis was performed. The *K1+M2* simulation was run for the period from 10 November 2012 to 25 November 2012, with the forcing linearly ramped up from zero over the first day to reduce transient effects. The first five days are considered to be a part of the model spin up, and are excluded from all analysis.

Subgrid scale mixing was parametrized using the scheme described by *Klymak and Legg* (2010), which calculates an enhanced viscosity and diffusivity by Thorpe sorting in regions of static instability. Background diffusivities and viscosities are chosen to maintain model stability and suppress noise. We use istropic diffusivities of $\kappa_H = \kappa_z = 1 \times 10^{-4}\mathrm{m^2s^{-1}}$, and anisotropic viscosities of $\nu_H = 5 \times 10^{-1}\mathrm{m^2s^{-1}}$ and $\nu_z = 1 \times 10^{-3}\mathrm{m^2s^{-1}}$.

A comparison of the K1 tidal ellipses from the *K1+M2* simulation and TPXO are shown in red and blue in Figure 3.1a. K1 ellipses were extracted from the simulated velocity timeseries after the model had spun up by a harmonic fit to the K1 frequency. Near to the boundaries, the simulation closely reproduces TPXO tidal ellipses, however in the vicinity of the ridge crest, significant discrepancies between the simulated and TPXO-predicted tides are present. A comparison of M2 tidal ellipses shows similar agreement away from and discrepancies close to the ridge crest (not shown). Two key differences between TPXO and the simulation presented here are the inclusion of stratification and a significantly higher resolution bathymetry, both of which may strongly influence tidal flows in the topographically complex region of the channel.

The along-channel tidal transport at the center of the channel predicted for the K1 and M2 constituents in TPXO and the simulation are shown as black and red lines in Figure 3.2c. While the phases approximately match, the magnitude of the transport is between two and four time greater in the regional simulation than in TPXO, and more closely agrees with observations. In addition, the timing of the strongest beat of the tide is shifted by 12 h in the regional simulation compared to TPXO, which also agrees with the observed inequality. Large transports close to bathymetry associated with subinertial tidal constituents have been observed in places like the Yermak Plateau (*Padman et al.*, 1992), and Fieberling Guyot (*Kunze and Toole*, 1997) and are attributed to topographically trapped waves. Despite this improvement, the transports are still significantly less than observed ($200\,\mathrm{m^2s^{-1}}$ rather than $500\,\mathrm{m^2s^{-1}}$).

The simulated depth-time series from the center of the channel is shown in Figure 3.2a. Timings of the strongest beat of the daily tide agree well with

observations, however the vertical structure of the weaker beat of the tide does is not well reproduced until later in the timeseries. For example, we find that the baroclinic structure of observed flows between 22 h 18-19 November is well matched by simulated flows between 19-20 November (green dashed lines in panels a and b), suggesting an error in the phase of the constituents in our simulation. After around 19 November, the amplitude of the diurnal inequality in the simulation is large and the weaker northward flow is surface confined, capturing the key features of our observations that we want to explain.

In summary we find that the simulation provides an improvement in the predicted transports through the ridge, and is able to reproduce the observed baroclinic flow structures. However, discrepancies between the model and observations remain in the relative phase of the K1 and M2 constituents, and the magnitude of the along-channel transports. Several factors may be responsible for these discrepancies, including non-tidal diurnal variability in the real ocean (such as a diurnal sea breeze), or errors in the magnitude and phase of the TPXO boundary conditions. Non-tidal diurnal variability would combine with the K1 tide to generate a diurnal signal with a different phase and amplitude, and could well explain our observed differences. Notwithstanding these differences, we consider that the processes that lead to the strong inequalities and surface confined northward tides during the latter part of the simulation to be of relevance to understanding our observations at this location.

3.4 Results & Discussion

3.4.1 The baroclinic harmonic constituents: radiating M2 and trapped K1 tides

At this latitude we expect that the M2 constituent will generate freely propagating internal tides, whilst the subinertial K1 constituent will have a response that is topographically trapped and unable to radiate into the open ocean. The precise nature of the trapped subinertial response depends sensitively on the strat-

ification and bathymetry. If the eigenmodes of the topography have frequencies that are close to K1 then a resonance between the topographic modes and the tidal forcing can excite waves that propagate along bathymetric gradients (*Chapman*, 1989). In the absence of a resonance, the subinertial baroclinic response is evanescent away from bathymetry, but may be more energetic than the superinertial constituent close to bathymetry (*Musgrave et al.*, 2015c).

A three-dimensional view of the trapped waves as they propagate along the steep bathymetry to the north of the ridge is shown in Figure 3.3. Isopycnal displacements associated with the K1 constituent were computed by harmonic reconstruction, and are contoured in red (downward isopycnal displacement) and blue (upward displacement). For step-like, vertical bathymetry, the trapped waves formally become internal Kelvin waves (*Rhines*, 1970), and have a vertically modal structure between the top and bottom of the step. In a similar manner to open ocean superinertial internal waves, the superposition of the modes forms beams: coherent sloping structures trapped close to the bathymetry. As time progresses, phase moves down in the upward radiating beams, and up in the downward radiating beams. Phase progression is easily observed in the animation of one period of the trapped wave evolution, which is included in the supplementary material.

On the southern flank of the ridge the bathymetry is less steep, and the trapped waves are strongly bottom trapped, their dynamics is closely related to stratified topographic Rossby waves.

3.4.2 Diurnal trapped waves and their influence on turbulence in the channel

The observed daily inequality in the strength of the transport through the channel arises from a simple sum of tidal constituents at the K1 and M2 frequencies. At roughly alternate 12 h intervals, the two constituents will either constructively or destructively superpose (leading to the strong and weak daily beats of the tide, respectively). However, it is the baroclinic structure of the flows associated with these constituents that determines the formation of tidal lee waves and their associated turbulence.

We compute reconstructions of the K1 and M2 harmonic components in along-channel sections at 12 h separated intervals corresponding to northward flows on 19 November 2012 (Figure 3.4), when the modeled transports have a similar vertical structure as our observations (i.e. strong daily inequalities). The first northward flow (panel a) corresponds to the strong beat of the tide, when both the K1 and M2 constituents have a northward transport. The baroclinic structure of the K1 constituent shows a northward flow that is strongly bottom enhanced, whilst the M2 component is less constrained in the vertical. The full flow (which is a sum of not only the K1 and M2 constituents, but also all other frequencies) exhibits full depth northward speeds, and preludes the generation of a large amplitude tidal lee wave and large parametrized mixing in the model. 12 h later the K1 tidal constituent is associated with a southward flow, whilst the M2 constituent is northward. As the K1 constituent is bottom trapped the resulting full field has a transport that is entirely accommodated in a surface layer which does not directly interact with the ridge crest. As a result no lee wave is generated during this beat of the tide, and there is very little turbulence.

Though it is a nonlinear process, the generation of turbulence in the channel can be simply understood in terms of a linear superposition of distinct baroclinic flows associated with the superinertial and subinertial tidal constituents. As the tidal constituents do not have frequencies that are exact multiples of one another, we expect that their relative phases will drift on a slow timescale, and this can be seen in the mooring timeseries (Figure 3.2b). At the beginning of the time-series the daily inequality is large as the constituents are in phase, and lee waves are alternately enhanced and suppressed in the channel. However, near the end the inequality is much reduced, and the baroclinic structure of flows through the channel is much more similar in adjacent tides.

3.4.3 Diurnal trapped waves and regional energetics

3.4.3.1 Dissipation rates over the ridge crest

Timeseries of the simulated volume integrated dissipation rates and area averaged barotropic tidal speeds for the vicinity of the ridge ($100 < x < 145\,\text{km}$, and $100 < y < 130\,\text{km}$) are shown in Figure 3.5. Strikingly, despite the semidiurnal nature of the barotropic tide the volume integrated dissipation rate is diurnally modulated, varying by an order of magnitude each day. In the first part of the timeseries peak dissipation rates occur just after peak southward flow, which is the largest of the daily peaks. As the relative phases of K1 and M2 progress, the largest tidal speeds are associated with northward flow, and the dissipation peak shifts to lag peak northward flow.

Observed timeseries from stations over the ridge on the western flank of the channel (R1 and R2, Figure 3.1 b i.) show similar features to the timeseries in the channel, with alternate northward flows being surface confined and not generating tidal lee waves. Combined with these model results, we conclude that the specific interaction of the trapped wave with the surface tide described for the channel flows is relevant over the whole ridge. The generation of tidal lee waves and nearfield turbulence is entirely determined by relative phase of the the diurnal trapped wave and the M2 tide

3.4.3.2 Flux, conversion and dissipation

To assess the energetics of the internal wave field we follow *Kang and Fringer* (2012) to compute the baroclinic-barotropic conversion, C, and the flux associated with the K1 and M2 constituents, $\mathbf{F}_{K1}$ and $\mathbf{F}_{M2}$, respectively. Conversion is the exchange term between the barotropic and baroclinic energy equations, quantifying the rate at which barotropic energy is transferred to baroclinic motion:

$$C = \frac{g}{T}\int_0^T \rho' W \,\mathrm{d}t. \tag{3.2}$$

T is the averaging period (an integer multiple of the tidal period), g is the gravitational acceleration and the density has been partitioned as $\rho = \rho_0 + \overline{\rho}(z) + \rho'(\mathbf{x}, t)$

so that ρ' is the density anomaly with respect to a stably stratified background state. W is the barotropic vertical velocity, which is defined

$$W = -\nabla_H \cdot [(d+z)\mathbf{U}_H], \tag{3.3}$$

where ∇_H indicates the horizontal gradient operator, d is the depth of the ocean, and $\mathbf{U}_H$ is the barotropic horizontal velocity. Fluxes are calculated as

$$\mathbf{F} = \frac{1}{T}\int_{-d}^{\eta}\int_{0}^{T} p'\mathbf{u}'\,\mathrm{d}t\,\mathrm{d}z, \tag{3.4}$$

where primes indicate that depth mean (barotropic) components have been removed (see, e.g. *Nash et al.* (2005)). Over non-flat topography, the baroclinic flux computed in this way includes small contributions from the surface tide due to isopycnal heave (*Kelly et al.*, 2010). To compute the fluxes associated with each tidal constituent, we first perform a harmonic fit to the K1 and M2 tidal frequencies, and reconstruct timeseries for pressure and velocity associated with each constituent which are then used to calculate the flux associated with each.

At steady state the baroclinic energy equation may be written

$$C - \nabla_H \cdot \mathbf{F} = \epsilon', \tag{3.5}$$

where ϵ' is the dissipation rate of baroclinic energy. Though we are able to directly assess the modeled dissipation rate ϵ_r, we find that it underestimates the difference on the left hand side of equation (3.5) due to the presence of numerical dissipation, which is not accounted for in explicit calculations of dissipation rate. *Kang and Fringer* (2012) performed a series of sensitivity studies in a similar regional tide model, and found that model reported dissipation rates were highly sensitive to parameters of the chosen closure scheme, whilst the inferred dissipation rate, $\epsilon_i = C - \nabla_H \cdot \mathbf{F}$ hardly changed. As such, in what follows we report inferred dissipation rates except where explicitly stated otherwise (*Carter et al.*, 2008; *Kang and Fringer*, 2012; *Buijsman et al.*, 2013).

Modeled conversion at the crest of the ridge in the *K1+M2* simulation is shown in Figure 3.6a. Values are largest near the crest of the ridge where the internal tide is most efficiently generated at a rate of up to $1.5\,\mathrm{Wm}^{-2}$. For

comparison, *Kang and Fringer* (2012) calculate conversions of around $0.2\,\mathrm{Wm}^{-2}$ at the coastal Monterey Canyon, while *Carter et al.* (2008) obtain 1-2 Wm^{-2} at Hawaii, a deep ocean site, and *Buijsman et al.* (2013) calculate peak conversions of $1.5\,\mathrm{Wm}^{-2}$ at the Luzon Strait. Regions of negative conversion occur where the internal tide transfers energy back into barotropic motions, mainly along the steep continental shelf to the north of the ridge.

The distinct natures of the baroclinic K1 and M2 constituents are made clear in Figure 3.6b and c which show the flux associated with each frequency. Fluxes of the M2 constituent are mostly directed outwards from topography with the exception of in the two canyons to the north of the ridge, where fluxes are directed onshore. M2 fluxes reach up to $7.5\,\mathrm{kWm}^{-2}$ in places. Fluxes of the K1 constituent are largest close to the crest of the ridge, where they are directed parallel to bathymetric contours, consistent with a trapped wave propagating anticyclonically along the ridge.

Time averaged dissipation rates from overturns are shown in Figure 3.6d. We show this, rather than inferred dissipation rates as overturns correspond to regions of directly resolved wave breaking, where isopycnal displacements have become sufficiently large and steep to overturn at this resolution, emphasizing phenomena such as tidal lee waves rather than boundary layer effects. Dissipation from overturns is enhanced close to the crest of the ridge, in particular along the flanks where tidal lee waves form (Musgrave *et al.* 2015). Inhomogeneities in dissipation rate along the length of the ridge reflect small scale bathymetric complexity, with enhanced dissipation occurring close to the channel at the ridge crest and at other small scale features.

3.4.3.3 Influence of K1 on q

The expression

$$q = \frac{\text{Nearfield dissipation}}{\text{Conversion}} \times 100\% \tag{3.6}$$

defines the percentage of the energy converted into baroclinic motions that is dissipated locally, contributing to nearfield mixing and water mass modification. The

remaining baroclinic energy radiates into the farfield to affect mixing at remote locations. We define an analysis region, $100 < x < 145\,\mathrm{km}$ and $100 < y < 135\,\mathrm{km}$ (dashed box in Figure 3.6), and calculate conversion, radiating flux, inferred dissipation and q for each of the three simulations (Table 3.1).

Unsurprisingly the *K1-only* simulation has the highest fraction of locally dissipated baroclinic energy as trapped waves generated at the ridge crest do not propagate efficiently out of the domain to the north. Trapped waves are eigenmodes of the bathymetry where they are generated. However, as they propagate away from their generation site along irregular bathymetry they encounter topography where their structure no longer projects onto the local topographic eigenmodes, and their energy dissipates. As such, most (67%) of the baroclinic energy generated by this subinertial K1-tide is dissipated very close to where it is generated.

In contrast, the *M2-only* simulation has the lowest fraction of locally dissipated baroclinic energy, as the radiating waves generated at the ridge crest are eigenmodes of the constant stratification all the way into the open ocean, allowing the efficient radiation of energy out of the domain. In our small analysis domain close to the coast, 25% of the generated baroclinic energy is dissipated in the nearfield, through near ridge processes such as tidal lee waves and hydraulic jumps.

Including both constituents in a single simulation changes the regional energy balance in a nonlinear manner. Both conversion and dissipation are larger (by 15% and 55% respectively) in the *K1+M2* simulation than the sum of the individual constituent runs, indicating that nonlinear interactions between the two constituents plays an important role in the region's tidal energetics. The ratio of locally dissipated energy to conversion lies between the *K1-only* and *M2-only* runs, with a value of 45% - comparable to that found at Monterey Canyon where 58% of baroclinic energy is thought to dissipate locally (*Kang and Fringer* (2012), though this work only considered the M2 tidal frequency), and at the Luzon Strait, where $q = 40\%$ (*Alford et al.*, 2015). At deep ocean sites, such as Hawaii, radiation is much larger than dissipation, and *Carter et al.* (2008) estimate $q = 15\%$.

3.5 Summary

Observations in the vicinity of a channel through the Mendocino Ridge show that tidal lee waves are not associated with every tidal peak. Instead, tidal lee waves form only after the largest peak tide each day (the strong beat of the tide), with lee wave formation suppressed during the weaker peak tide. Using a regional model driven by TPXO barotropic tides at the boundaries, we show that the subinertial tidal constituent generates a trapped wave which propagates anticyclonically around the ridge crest, and generates large transports through the channel. This is consistent with maps of barotropic tidal dissipation made by (*Egbert and Ray*, 2003), who show that our study location is an efficient dissipator of K1 barotropic tidal energy. The trapped wave is locally dissipative, with our single constituent simulation showing that 67% of the barotropic-baroclinic conversion dissipating close to where the wave is generated.

The large, bottom-trapped isopycnal displacements and velocities associated with the trapped wave cause near-bottom flows through the channel to be alternately enhanced and suppressed depending on whether the trapped wave is in phase with the semidiurnal tide, or not. When the constituents are in phase the flow through the channel is bottom intensified and generates a large, turbulent tidal lee wave on the downstream face of the ridge. When the constituents are out of phase, their destructive superposition means that near bottom flows are weak and the full tidal transport is accommodated close to the surface. In this latter case no tidal lee wave forms, and turbulent dissipation rates are small.

The extent to which this process in the channel is applicable to the rest of the ridge is assessed using the model to consider ridge-averaged quantities. Over the 10 day simulation, ridge-averaged turbulent dissipation rates are always diurnally modulated, despite average barotropic velocities being strongly semidiurnal. Observations from atop the crest of the ridge flanking the channel show similar baroclinic structures as within the channel, and we infer that the specific process described for the channel flows is more generally relevant over this ridge.

At this location, therefore, we conclude that the subinertial trapped wave

strongly influences the nearfield dissipation rate and its concomitant mixing, having broader implications on water mass properties and regional scale flows. In our combined *K1+M2* simulation the rate of conversion of energy from barotropic to baroclinic motions increases by 15% and the total nearfield dissipation of baroclinic energy increases by 55% over the sum of conversions and dissipations from single constituent runs. The influence of subinertial tidal constituents on the global distribution of dissipation and mixing is potentially significant, with the impacts of enhanced nearfield mixing being especially important in climactically sensitive regions where the vertical redistribution of heat can directly affect the formation and melt of sea ice, or the basal erosion of glaciers. Our study suggests that understanding the processes leading to tidally driven turbulence and mixing at latitudes where the diurnal tide is subinertial ($> 30°$, 50% of the Earth's surface) requires consideration of both the subinertial and superinertial tidal constituents, with subinertial bottom velocities determining both the magnitude and phase of nearfield dissipation rates.

3.6 Acknowledgments

Ship time was provided by UC Ship Funds. Shaun Johnston, Uwe Send, Janet Sprintall generously loaned instrumentation that made these measurements possible. Thanks to Capt Murline & the crew of the R/V Revelle for their professionalism and skill at sea, and to Paul Chua and 10 UNOLS volunteers for their amazing help gathering this data. Computing was carried out on the Compas cluster at SIO. We acknowledge useful conversations with Myrl Hendershott and thank Uriel Zajaczkovski for his help making the 3D visualizations using Paraview, an open source platform for scientific visualization. RCM is funded by the Office of Naval Research.

Chapter 3 is currently being prepared for submission for publication of the material to the Journal of Physical Oceanography, Musgrave, R C; MacKinnon, J A; Pinkel, R; Waterhouse, A F; Nash, J; Kelly, S. The dissertation author was the primary investigator and author of this paper.

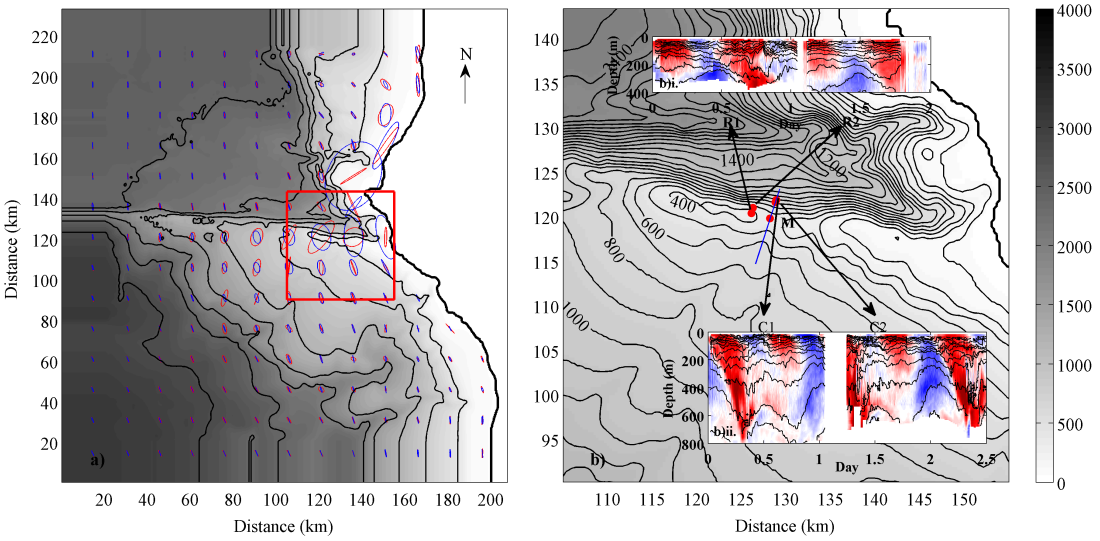

Figure 3.1: a) Bathymetry over full computational domain. The geographic region is the easternmost extent of the Mendocino Ridge in the eastern Pacific, at a latitude of 40°. Blue tidal ellipses are TPXO predictions for the barotropic K1 constituent, and red ellipses are the barotropic K1 constituent from tidal regional model. b) Inset (red box in a) showing the ridge-top channel where observations were taken. Cross-ridge velocity timeseries from four stations are shown in insets, with isopycnals contoured.

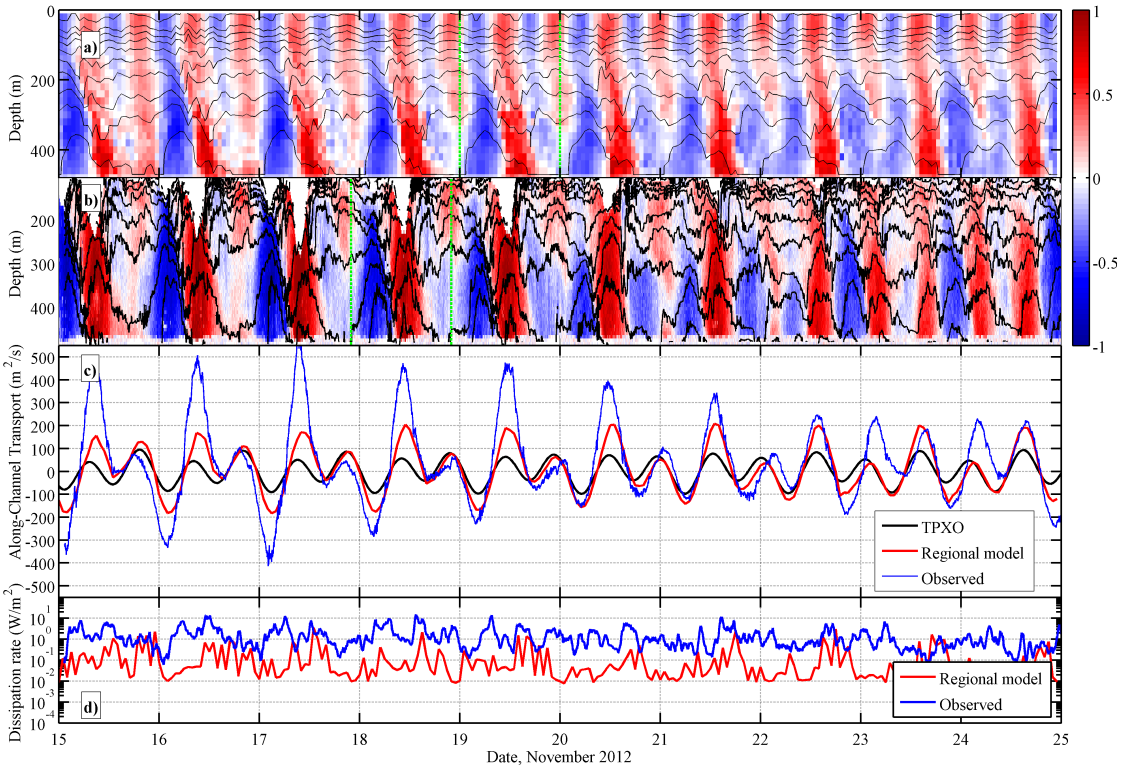

Figure 3.2: Modelled (a) and observed (b) cross-channel velocity timeseries at mooring. Isopycnals contoured. (c) Transports at mooring from observations (blue), regional model (red) and TPXO predictions (black). (d) Depth integrated dissipation rates at mooring from observations (blue) and from overturns in regional model (red).

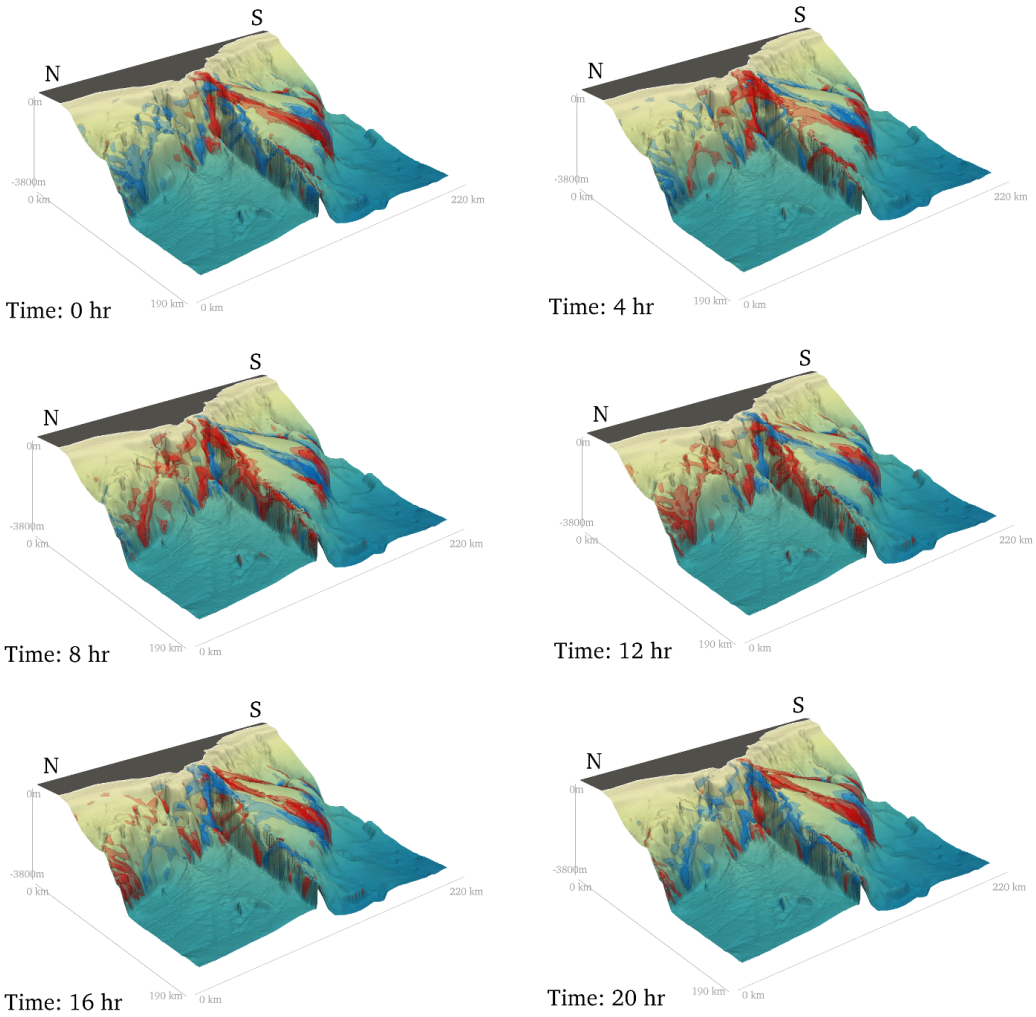

Figure 3.3: 3D view of trapped tides, ±15 m isopycnal displacements are contoured with upward displacements in blue, and downward displacements in red.

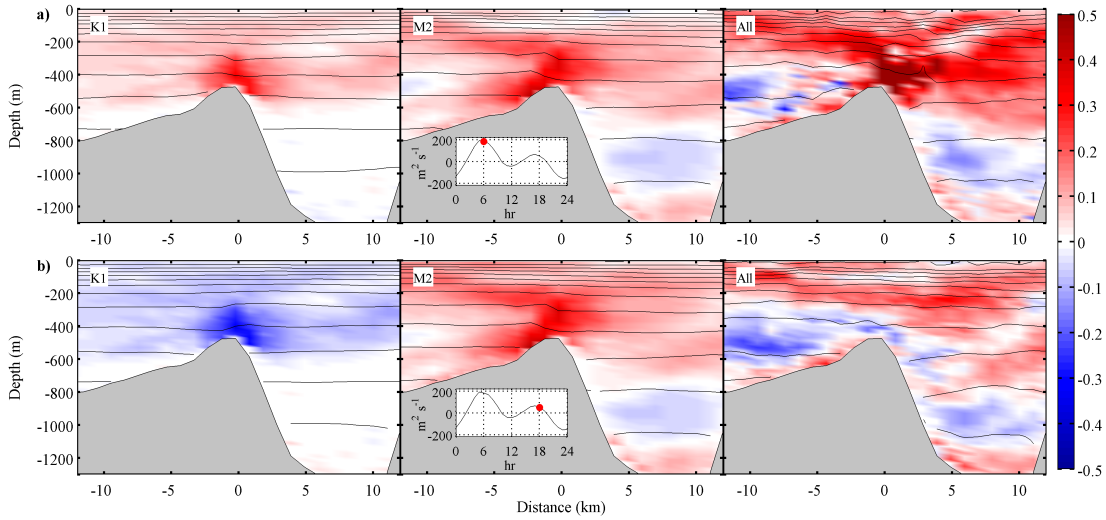

Figure 3.4: K1, M2 and full along-channel velocity component, 12 h apart.

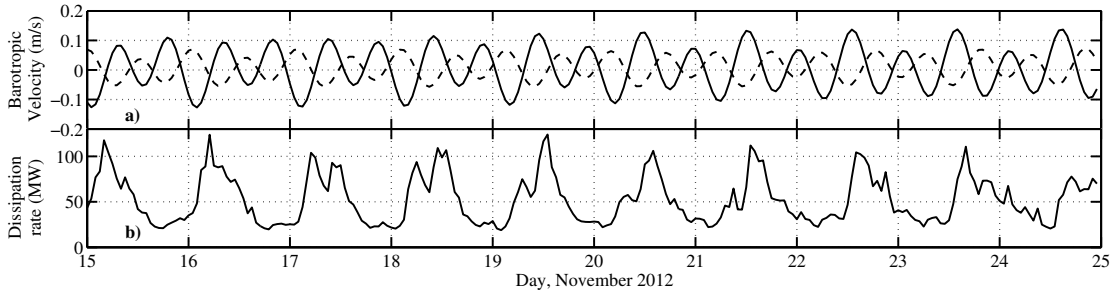

Figure 3.5: Timeseries of a) area averaged barotropic tidal speeds (solid: cross-ridge velocity, dashed: along-ridge velocity) and b) volume integrated dissipation rates for $100 < x < 145\,\text{km}$ and $100 < y < 135\,\text{km}$.

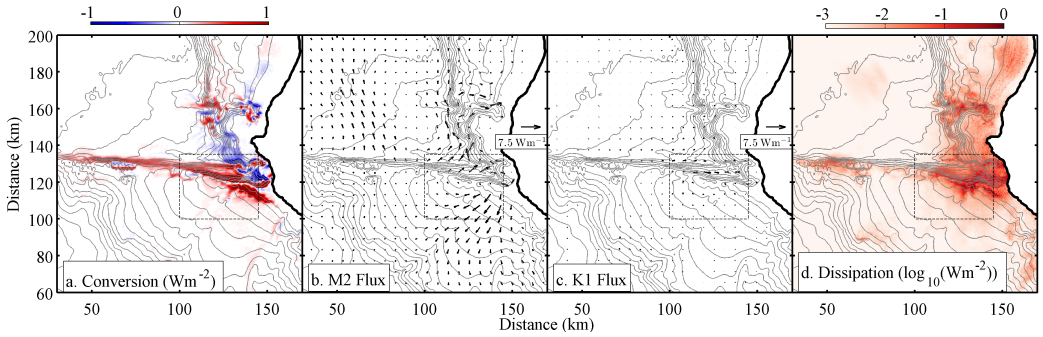

Figure 3.6: Terms in regional energy budget for K1+M2 simulation: a) Barotropic-baroclinic conversion, b) M2 flux, c) K1 flux and d) Time averaged dissipation rate from overturns. Dashed box indicates analysis region for energy budget.

Table 3.1: Terms of baroclinic energy budget in MW for each simulation, integrated over analysis domain.

	$K1-only$	$M2-only$	$K1+M2$
Conversion	58	215	316
Outward Flux	19	161	171
ϵ_{inf}	39	54	145
q	67%	25%	45%

Chapter 4

Stratified tidal flow over a tall ridge above and below the turning latitude

The interaction of the barotropic tide with a tall, two-dimensional ridge is examined analytically and numerically at latitudes where the tide is subinertial, and contrasted to when the tide is superinertial. When the tide is subinertial, the energy density associated with the response grows with latitude as both the oscillatory along-ridge flow and near ridge isopycnal displacement become large. Nonlinear processes lead to the formation of along-ridge jets, which become faster at high latitudes. Dissipation and mixing is larger, and peaks later in the tidal cycle when the tide is subinertial compared to when the tide is superinertial. Mixing occurs mainly on the flanks of the topography in both cases, though a superinertial tide may additionally generate mixing above topography arising from convective breaking of radiating waves.

4.1 Introduction

The ubiquity of internal tides in the ocean has prompted extensive study of their generation at topography, and subsequent radiation (*Bell*, 1975; *Baines*, 1982; *Llewellyn Smith and Young*, 2003). Their role in mixing the stably stratified

ocean as they dissipate is well established (*Munk and Wunsch*, 1998), and global climate models (GCMs) have provided an insight into the remarkable sensitivity of large scale ocean circulation on the distribution and magnitude of the mixing (*Hasumi and Suginohara*, 1999; *Simmons et al.*, 2004; *Jayne*, 2009). As a result, significant effort has been expended developing physically based parameterizations for dissipative processes associated with the superinertial internal tide, i.e. tidal motions with a period of less than one pendulum day (*Green and Nycander*, 2013). These parameterizations are now being implemented in GCMs that are used to inform climate policy (e.g. *Melet et al.* (2013)). In contrast, the mixing associated with subinertial tidal constituents is much less well studied and remains unaccounted for. This is largely because the internal wave dispersion relation disallows radiating internal waves whose period is more than that of the local pendulum day, which means that subinertial tidal constituents do not generate radiating internal tides. Instead, subinertial tides generate a baroclinic response that is evanescent, decaying exponentially away from topography and consequently accounting for less baroclinic energy globally than their superinertial counterparts. Nevertheless, observational and regional modeling studies indicate that the nearfield mixing associated with these trapped tides may be significant (*Nakamura et al.*, 2010; *Osafune and Yasuda*, 2013; *Musgrave et al.*, 2015b). In this paper we present an idealized study that explores in detail the nature of the baroclinic response to subinertial tidal forcing, and contrast the physics and processes leading to mixing to those in the relatively well understood superinertial case.

In the first part of the paper we build on the work of *Llewellyn Smith and Young* (2003), to derive an analytic solution for subinertial trapped tides generated at a tall, infinitely thin ridge. We show that the baroclinic response is evanescent with a decay scale that decreases with increasing latitude. Both the along-ridge velocity and the near-ridge isopycnal displacement of the evanescent response grow with latitude away from the turning latitude (defined as where the tidal frequency matches the local Coriolis frequency). As a result, for a constant amplitude barotropic tide, the total near-ridge energy density (i.e. kinetic plus potential) of the subinertial baroclinic response grows with latitude, in direct contrast

with the superinertial baroclinic response which has a constant energy density at all latitudes.

We explore and verify these predictions in a series of idealized two-dimensional numerical simulations where a 24 hr oscillating tide interacts with a Gaussian ridge at a range of latitudes. Of particular interest is the influence of latitude on the processes leading to turbulence, which not been previously explored. In the two-dimensional simulations presented here, we use mixing as a proxy for turbulence in the three-dimensional ocean. By performing "equivalent" simulations at superinertial and subinertial latitudes, we find that transient hydraulic jumps are the dominant mechanism for mixing in our simulations when the tide is subinertial, and tidal lee waves formed from radiating constituents are additionally important when the tide is superinertial.

We also investigate the generation of tidally rectified along-ridge currents, whose energy is significant in the nearfield and increases with latitude. These have been examined analytically for both unstratified tidal flows (*Huthnance*, 1973; *Loder*, 1980), and stratified tidal flows over weak topography (*Maas and Zimmerman*, 1989b; *Brink*, 2011). The combination of tall topography and stratification places our simulations beyond the parameter regime of prior theory, but nevertheless we find similar qualitative results of strong along-slope flows, and weaker cross-slope and vertical circulations in the Eulerian time mean. The explicit calculation of particle paths show that particles near the ridge-crest undergo looping trajectories along the flanks.

Observations of enhanced subinertial frequency currents around topography have motivated the investigation of trapped topographic waves (*Rhines*, 1970; *Chapman*, 1989; *Brink*, 1990; *Padman et al.*, 1992; *Codiga*, 1997). These arise from a resonance between the free modes associated with a certain topography and background stratification, and an ambient forcing frequency. The solutions presented in this paper are complementary, describing the forced response to subinertial tides which may be expected even in the absence of a resonance. When the forced response projects onto the free modes of a certain topography, a resonant trapped free wave may be expected.

The remainder of this paper is broadly divided into four parts: the first presents theoretical results for subinertial tidal forcing of a stratified fluid over a knife-edge ridge; the second presents a series of numerical experiments over a tall, narrow Gaussian ridge aimed at verifying the theory, and extending the description to larger amplitude, more nonlinear tides; and the third discusses the relevance of this work to more general three-dimensional situations. In the fourth section we present a summary.

4.2 Theory

In this section we extend the results of *Llewellyn Smith and Young* (2003) (hereafter LSY03) to include subinertial tidal forcings. The problem is formulated in two dimensions on an f-plane, with an imposed barotropic tide ($u_b = U_0 \cos \omega t$) oscillating in the x-direction. The total fluid depth is h. At $x = 0$ the tide interacts with an infinitely thin ridge of height z_0, where $z_0 < h$. For simplicity we consider only uniform stratification (N) in this study, though LSY03 additionally presents solutions for the case of slowly varying $N(z)$. In Appendix B we formally derive the linear, hydrostatic, Boussinesq equations that are suitable for this system by considering both the particle excursion length $\varepsilon = U_0/\omega x_0$ (where x_0 is the horizontal length scale of the response), and the topographic Froude number, $F = U_0/Nz_0$ to be small. Dropping the subscript, the leading-order equations are:

$$\begin{aligned} u_t - fv &= -p_x \\ v_t + fu &= 0 \\ p_z &= b \\ b_t + N^2 w &= 0 \\ u_x + w_z &= 0. \end{aligned} \tag{4.1}$$

In (4.52) the density has been written

$$\rho = \rho_0 \left[1 - \frac{N^2 z}{g} - \frac{b}{g} \right], \tag{4.2}$$

and pressure has been scaled by ρ_0. Defining a stream function $(u, w) = (-\psi_z, \psi_x)$, the equations can be combined, and written as

$$\psi_{zztt} + f^2\psi_{zz} + N^2\psi_{xx} = 0. \tag{4.3}$$

Imposing a boundary condition of no-flow through the barrier means

$$\psi(x = 0, z < z_0) = U_0 z \cos(\omega t), \tag{4.4}$$

such that $U_T = u_b + u = U_0 \cos(\omega t) + u = 0$ on the knife-edge ridge.

In the linear limit we look for solutions which are time periodic at the tidal frequency, ω:

$$\psi = U_0 Re\{e^{-i\omega t}\phi\}.$$

Then, (4.3) can be written

$$N^2\phi_{xx} = (\omega^2 - f^2)\phi_{zz} \tag{4.5}$$

with boundary conditions $\phi(x = 0, z < z_0) = z$, and $\phi(x, h) = 0$. For superinertial flows, $\omega^2 > f^2$ and the equation is hyperbolic, however, for subinertial flows, $\omega^2 < f^2$ and the equation is elliptic. The solution is constructed from an infinite sum of the vertical normal modes, defined by

$$\frac{d^2 a_n}{dz^2} + \frac{N^2 a_n}{c_n^2} = 0 \tag{4.6}$$

with $a_n(0) = a_n(h) = 0$, and $\int_0^h a_n(z)a_m(z)\,dz = \frac{h}{2}\delta_{mn}$.

A Green's function solution to equation (4.5) satisfies:

$$N^2 G_{xx} - (\omega^2 - f^2)G_{zz} = G_0\delta(x)\delta(z - z') \tag{4.7}$$

for a point source located at $x = 0$, $z = z'$. The normalization G_0 will be determined shortly for convenience. We write the vertical dependence of the separable solution in terms of an infinite sum of vertical normal modes, $a_n = \sin(nZ)$,

$$G(x, Z, Z') = \sum_{n=1}^{\infty} G_n(x, Z') \sin(nZ) \tag{4.8}$$

where $Z = \frac{\pi z}{h}$.

For modal phase speeds $c_n = hN/n\pi$, we define two real wave numbers corresponding to the superinertial ($\check{}$: below the turning latitude) and subinertial ($\hat{}$: above the turning latitude) cases:

$$\check{k}_n^2 = \frac{\omega^2 - f^2}{c_n^2} \quad \text{and} \quad \hat{k}_n^2 = \frac{f^2 - \omega^2}{c_n^2}. \tag{4.9}$$

The superinertial case is explicitly dealt with in LSY03, so here we concentrate on the subinertial case, for which (4.7) can be written in terms of vertical modes

$$\frac{\partial^2 \hat{G}_n}{\partial x^2} - \hat{k}_n^2 \hat{G}_n = \frac{2}{h} G_0 \delta(x) \sin(nZ') . \tag{4.10}$$

For $x \neq 0$, the solution is

$$\hat{G}_n = A(z') e^{-\hat{k}_n |x|} = \begin{cases} A e^{-\hat{k}_n x}, & x > 0 \\ A e^{\hat{k}_n x}, & x < 0 \end{cases} \tag{4.11}$$

The constant, A, is determined by integrating (4.10) between $x^- < 0$ and $x^+ > 0$ and matching solutions as $x \to 0$, giving

$$A = -\frac{G_0}{\hat{k}_n h} \sin(nZ') . \tag{4.12}$$

The subinertial Green's function solution is

$$\hat{G} = -\frac{G_0}{h} \sum_{n=1}^{\infty} \frac{1}{\hat{k}_n} e^{-\hat{k}_n |x|} \sin(nZ') \sin(nZ) . \tag{4.13}$$

For comparison, LSY03 eq (3.8) is the superinertial Greens Function solution

$$\check{G} = \frac{G_0}{h} \sum_{n=1}^{\infty} \frac{1}{i\check{k}_n} e^{i\check{k}_n |x|} \sin(nZ') \sin(nZ) . \tag{4.14}$$

For consistency with LSY03, we define

$$\check{\mu} = \frac{N}{\sqrt{\omega^2 - f^2}}; \qquad \check{k}_n = \frac{n\pi}{h\check{\mu}},$$
$$\hat{\mu} = \frac{N}{\sqrt{f^2 - \omega^2}}; \qquad \hat{k}_n = \frac{n\pi}{h\hat{\mu}},$$

and we nondimensionalize $X = \pi x/\mu h$. Defining $G_0 = -N^2/\mu$ we write

$$\hat{G}(X, Z, Z') = \sum_{n=1}^{\infty} \frac{e^{-n|\hat{X}|}}{n\pi} \sin(nZ) \sin(nZ'), \tag{4.15}$$

to be compared to LSY03 eq. 3.11 for the superinertial case:

$$\check{G}(X, Z, Z') = \sum_{n=1}^{\infty} \frac{e^{in|\check{X}|}}{n\pi} \sin(nZ) \sin(nZ'). \tag{4.16}$$

The series in (4.15) can be expressed using the real function

$$\bowtie(X, Z, Z') = \frac{\cos(Z + Z') - \cosh|X|}{\cos(Z - Z') - \cosh|X|}, \tag{4.17}$$

and the Green's function becomes

$$\hat{G}(X, Z, Z') = \frac{\ln|\bowtie|}{4\pi}. \tag{4.18}$$

4.2.1 Streamfunction

The subinertial solution to (4.5) is represented in terms of the Green's function as

$$\hat{\phi}(X, Z) = \frac{h}{\pi} \int_0^{Z_0} \Gamma(Z') \hat{G}(X, Z, Z')\, dZ'. \tag{4.19}$$

where $Z_0 = \pi z_0/h$, and $\Gamma(Z')$ is the source density. Evaluated on the knife edge where the boundary condition is $\phi(0, z < z_0) = z$, this becomes

$$Z = \frac{1}{2\pi} \int_0^{Z_0} \Gamma(Z') \ln\left|\frac{\sin(\frac{1}{2}(Z + Z'))}{\sin(\frac{1}{2}(Z - Z'))}\right| dZ'. \tag{4.20}$$

LSY03 demonstrate this may be arranged to a standard form and solved for Γ:

$$\Gamma(Z) = 2\sqrt{\frac{1 - \cos(Z)}{\cos(Z) - \cos(Z_0)}}. \tag{4.21}$$

Substituting equations (4.15) and (4.21) into equation (4.19), and using the identity:

$$\frac{2}{\pi} \int_0^{Z_0} \sin nZ \sqrt{\frac{1 - \cos(Z)}{\cos(Z) - \cos(Z_0)}}\, dZ = P_{n-1}(\cos Z_0) - P_n(\cos Z_0) \equiv PP_n$$

where P_n is the nth Legendre polynomial, gives an expression for the streamfunction, which decays exponentially with distance away from the ridge:

$$\hat{\phi}(X,Z) = \frac{h}{\pi}\sum_{n=1}^{\infty}\frac{e^{-n|\hat{X}|}}{n}PP_n\sin(nZ). \tag{4.22}$$

For comparison, LSY03 gives the super inertial solution:

$$\check{\phi}(X,Z) = \frac{h}{\pi}\sum_{n=1}^{\infty}\frac{e^{in|\check{X}|}}{n}PP_n\sin(nZ). \tag{4.23}$$

4.2.2 Explicit fields and relative phases

The general streamfunction, ψ, may be written

$$\begin{aligned}\psi &= U_0\mathrm{Re}(e^{-i\omega t}\phi)\\ &= U_0\phi_r\cos(\omega t) + U_0\phi_i\sin(\omega t).\end{aligned}$$

Two components of the velocity field are directly evaluated from the streamfunction: $(u,w) = (-\psi_z, \psi_x)$. The remaining fields are derived from equations (4.52). The superinertial fields are:

$$\begin{aligned}
\check{u} &= -U_0\sum_{n=1}^{\infty}PP_n\cos(nZ)\cos\left(n|\check{X}| - \omega t\right),\\
\check{v} &= -\frac{fU_0}{\omega}\sum_{n=1}^{\infty}PP_n\cos(nZ)\sin\left(n|\check{X}| - \omega t\right),\\
\check{w} &= -\operatorname{sgn}(x)\frac{U_0}{\check{\mu}}\sum_{n=1}^{\infty}PP_n\sin(nZ)\sin\left(n|\check{X}| - \omega t\right),\\
\check{b} &= \operatorname{sgn}(x)\frac{N^2U_0}{\omega\check{\mu}}\sum_{n=1}^{\infty}PP_n\sin(nZ)\cos\left(n|\check{X}| - \omega t\right),\\
\check{p} &= -\operatorname{sgn}(x)\frac{N^2U_0h}{\pi\omega\check{\mu}}\sum_{n=1}^{\infty}\frac{PP_n}{n}\cos(nZ)\cos(n|\check{X}| - \omega t).
\end{aligned} \tag{4.24}$$

The subinertial fields are:

$$\begin{aligned}
\hat{u} &= -U_0 \cos(\omega t) \sum_{n=1}^{\infty} e^{-n|\hat{X}|} P P_n \cos(nZ)\,, \\
\hat{v} &= \frac{f U_0}{\omega} \sin(\omega t) \sum_{n=1}^{\infty} e^{-n|\hat{X}|} P P_n \cos(nZ)\,, \\
\hat{w} &= -U_0 \cos(\omega t) \frac{\operatorname{sgn} x}{\hat{\mu}} \sum_{n=1}^{\infty} e^{-n|\hat{X}|} P P_n \sin(nZ), \\
\hat{b} &= \frac{N^2 U_0}{\omega \hat{\mu}} \operatorname{sgn}(x) \sin(\omega t) \sum_{n=1}^{\infty} e^{-n|\hat{X}|} P P_n \sin(nZ), \\
\hat{p} &= -\frac{N^2 U_0 h}{\pi \omega \hat{\mu}} \operatorname{sgn}(x) \sin(\omega t) \sum_{n=1}^{\infty} \frac{e^{-n|\hat{X}|}}{n} P P_n \cos(nZ).
\end{aligned} \tag{4.25}$$

Some important properties of the solutions are apparent by inspection, and are illustrated in Figure 4.2. Subinertial solutions are evanescent and trapped to the ridge crest with a decay scale $1/\hat{k}$ that decreases with latitude. Superinertial solutions are radiating waves with wavenumbers $\check{k}$, and form characteristic internal wave beams at slopes determined by the dispersion relation. Consistent with this trapped vs. radiating response, at $x = 0$ the subinertial buoyancy field has a quadrature phase relationship with the barotropic tide, whilst the superinertial buoyancy field is in phase.

In Appendix A we present an equivalent derivation of shallow water tidal interaction with a vertical wall. The solutions illustrate many of the same important properties as their stratified analogues, but the derivation is much simpler.

4.2.3 Energetics

Using the expressions obtained in the previous section, we evaluate the time and depth mean kinetic and potential energy at the ridge-crest ($x = 0$) using the following definitions appropriate for hydrostatic dynamics:

$$\begin{aligned}
\overline{\mathrm{KE}} &= \frac{\rho_0}{2} \frac{1}{Th} \int_0^T \int_0^h (u^2 + v^2)\, \mathrm{d}z\, \mathrm{d}t \\
\overline{\mathrm{PE}} &= \frac{\rho_0}{2N^2} \frac{1}{Th} \int_0^T \int_0^h b^2\, \mathrm{d}z\, \mathrm{d}t.
\end{aligned} \tag{4.26}$$

The integrals are performed over the full water depth, capturing the energy associated with the response on the flank of the ridge as well as above its crest. The superinertial energies are:

$$\begin{aligned}\overline{\breve{\mathrm{KE}}} &= \frac{1}{8}\rho_0 U_0^2 \left(\frac{\omega^2 + f^2}{\omega^2}\right) \sum_{n=1}^{\infty} PP_n^2, \\ \overline{\breve{\mathrm{APE}}} &= \frac{1}{8}\rho_0 U_0^2 \left(\frac{\omega^2 - f^2}{\omega^2}\right) \sum_{n=1}^{\infty} PP_n^2,\end{aligned} \tag{4.27}$$

and the subinertial energies are:

$$\begin{aligned}\overline{\hat{\mathrm{KE}}} &= \frac{1}{8}\rho_0 U_0^2 \left(\frac{\omega^2 + f^2}{\omega^2}\right) \sum_{n=1}^{\infty} PP_n^2, \\ \overline{\hat{\mathrm{APE}}} &= \frac{1}{8}\rho_0 U_0^2 \left(\frac{f^2 - \omega^2}{\omega^2}\right) \sum_{n=1}^{\infty} PP_n^2.\end{aligned} \tag{4.28}$$

Figure 4.3 illustrates the strong influence of rotation on the ridge-top energies for a 24 hr tide with a fixed tidal amplitude $U = 0.006$ ms^{-1}, a stratification of 1 cph, in a depth of 1000 m for a ridge of height 500 m. Below the turning latitude, the total energy density at the ridge has a fixed value of $2\times$ that of the barotropic tide for this particular choice of parameters. At f_{0° this corresponds to a wavelike response with equipartitioned kinetic and potential energy. At higher latitudes the waves have a reduced potential energy, but an increased kinetic energy due to the along-ridge component whose speed increases with latitude as f/ω. Above the turning latitude the response is evanescent, but the along-ridge oscillatory currents continue to grow with latitude. In contrast to superinertial behavior, the available potential energy of the evanescent response also grows with latitude as isopycnal displacements in the near field become large. The result is that for a fixed amplitude barotropic tide, the ridge-crest energy density of the response increases with latitude once the flow is subinertial.

The increase in energy density with latitude also holds if the near-ridge, rather than ridge-crest, response is considered. Defining "near-ridge" as within a distance of k^{-1} from the crest, we see that the near-ridge region decreases linearly in f. However, the ridge-top energy increases as f^2, causing the total near-ridge energy of the response to increase with latitude.

Despite the elevated near-topographic energy densities above the turning latitude, in this inviscid, 2D analytical model there is no conversion of energy from the barotropic tide to the baroclinic response once the latitude is subinertial. In the absence of dissipation, conversion may only arise by the generation of radiating waves, whose phase averaged energy flux is defined:

$$\mathbf{J} = \frac{1}{T}\int_0^T \int_0^h \mathbf{u}p \, \mathrm{d}z \, \mathrm{d}t. \tag{4.29}$$

In the subinertial solution, pressure and cross-ridge velocity have a quadrature phase relation in time and as a result there is no outward radiating flux, in contrast to the superinertial solution where the pressure and cross-ridge velocity are in phase. However, in the subinertial solution pressure and along-ridge velocity are in phase, suggesting the potential for along-ridge radiation in a three-dimensional solution.

4.3 Numerical simulations

4.3.1 Setup

To test the above theory and explicitly illustrate the effects of changing latitude on tidal flows over topography, we use the MITgcm (*Marshall et al.*, 1997) and solve the full nonlinear, nonhydrostatic equations for 2D tidal flow over a steep Gaussian seamount on an f-plane. For all runs we set the tidal frequency to be 24 hr, and the Gaussian topography to have a height of 500 m in 1000 m of water, and a horizontal e-folding scale of 1000 m. Stratification is constant in depth with a Brunt-Väisälä period of 1 hr. To minimize numerical diffusion, a seventh order monoticity preserving scheme is used for tracer advection (*Daru and Tenaud*, 2004). Momentum advection is by a centered second-order scheme.

For the finite width bathymetries in these simulations, a measure of the linearity of the flow is given by a nondimensional excursion length

$$\epsilon_{rdg} = \frac{U_c}{\omega l_{rdg}} \tag{4.30}$$

which compares the horizontal displacement of a fluid parcel each tidal cycle ($l_{exc} = U_c/\omega$) to a characteristic width of the ridge (l_{rdg}). U_c is the depth mean speed at the crest of the topography. Simulations are divided into two categories: the small excursion length simulations have a very small amplitude barotropic tide ($U_0 = 0.006\,\mathrm{ms}^{-1}$), and the long excursion length simulations have a larger amplitude tide ($U_0 = 0.02\,\mathrm{ms}^{-1}$). generating tidal excursion lengths at the ridge crest of 160 m and 550 m respectively. The width of the ridge is determined at a characteristic depth determined by the vertical length scale $\delta = U_0/N$ from the crest of the topography to be 600 m, suggesting that the small excursion length simulations should be dominantly linear, and the long excursion length simulations should include some nonlinear effects. A second parameter that can influence the linearity of the flow is the topographic Froude number, which is defined

$$Fr = \frac{U_0}{Nz_0}. \tag{4.31}$$

All simulations presented in this study have very small values of Fr, which in the ocean corresponds to tall topography where most of the tidal flow is unable to surmount the crest during all phases of the tide. Much of the tidal transport above the crest is accommodated in a relatively fast, thin, bottom intensified layer (*Winters and Armi*, 2013).

In these simulations the topography is supercritical at all latitudes where the tide is superinertial, meaning that it is steeper than the fundamental frequency internal wave response. The model is forced by the addition of a body force (G_u, G_v) to each of the horizontal momentum equations such that in the absence of topography the flow is rectilinear in the x-direction and oscillatory with frequency ω and amplitude U_0 (*Di Lorenzo et al.*, 2006). Specifically, we set

$$(G_u, G_v) = (-U_0\omega\sin(\omega t), U_0 f\cos(\omega t))\,. \tag{4.32}$$

The inclusion of a more realistic background tidal ellipse does not change the dynamics of these two-dimensional simulations, but it imposes greater computational demand by restricting the time-step. Ten small excursion length simulations are presented with f corresponding to latitudes, $\phi = [0, 10, 20, 25, 35, 40, 50, 60, 70, 80, 90]^\circ$.

We use subscript notation to refer to each simulation, where, for example f_{50° indicates the simulation was performed at a latitude of 50°. Two large excursion length simulations are performed at 3.85° and 44.7°. These latitudes are chosen as the theory of Section 4.2 predicts that the amplitude of near-crest isopycnal displacement, and therefore the available potential energy at the ridge crest, will be the same at each, even though the nature of the response will be fundamentally different. At $\phi = 30^\circ$ we are very close to the turning latitude of a 24 hr tide and the lengthscale, k^{-1}, is too large to fit in the computational domain. Therefore we do not present results from this simulation. Simulations are performed with telescoped horizontal resolution that is highest within 30 km of the ridge. Small excursion length simulations have an isotropic central resolution of 15 m, and large excursion length simulations have an isotropic central resolution of 5 m. As a check on the convergence of our numerical solutions, two of the small excursion length simulations (f_{10° and f_{50°) are repeated with identical parameters but doubled resolutions to ensure that our solutions are not quantitatively resolution dependent. Evaluation of the kinetic energy budget in the double resolution simulations reveal differences of less than 3% in the dominant terms, giving us confidence in the quantitative results of our standard resolution simulations. Time mean residuals in the energy balance are approximately 5 times smaller than the smallest term in the kinetic energy budget (the dissipation rate), and arise from spatial and temporal discretization errors in our post-simulation assessment of the budget, in addition to numerical diffusion by the model numerical schemes. In all cases, the domain has a total width of 300 km with periodic horizontal boundary conditions. Baroclinic signals that reach the boundaries reflect back into the domain, and as such we define an analysis region within ±4 km of the ridge crest, and perform all analysis before the reflected signals reach the boundaries of this domain, which occurs at a time easily identified using Hovmöller type diagrams at fixed depth. The fastest wave speeds in these simulations are approximately $0.5\,\mathrm{ms}^{-1}$, though this varied a little with latitude according to the dispersion relation for linear internal waves. As such we present analysis of these simulations between hours 120 and 144, 5 periods after the simulation starts. Background viscosities are 2×10^{-3} ms^{-2} cor-

responding to Reynolds numbers between 1500 and 5000, though the simulations are non-turbulent. Diffusivities are 8×10^{-4} ms^{-2} for all simulations, and no-slip boundary conditions are enforced at the topography.

4.3.2 Small excursion length simulations

4.3.2.1 Flow snapshots

Widefield snapshots of cross-ridge flow at 120 hr are presented in figure 4.4 for the simulations at latitudes of 10° and 50°. In this and all subsequent snapshot figures the spatially constant background tide, u_b, has been removed. Parameters are the same as used in the linear analytic solution presented in figure 4.2, enabling a direct comparison of linear theory with model output. In the f_{10° simulation, the forcing frequency is superinertial and the domain is filled with baroclinic energy associated with energetic radiating internal tides. Beams are present, formed from the superposition of linear internal wave modes. Their angles are dependent upon wave frequency according to the internal wave dispersion relation. Harmonics of the forcing frequency are visible at steeper angles, arising due to advection by the background tide (*Bell*, 1975). In contrast, the subinertial f_{50° simulation has much less energy in the far field as energy at the forcing frequency is unable to radiate at this latitude. Beams at angles corresponding to harmonics of the fundamental frequency are present, indicating the generation of some radiating energy, however, their energy content is small.

Nearfield snapshots of the simulations at 6 hr intervals between 120-144 hr are shown in figures 4.5 and 4.6. Cross-ridge velocity, u, is presented in the upper panel, and along-ridge velocity, v, in the lower panel. Consistent with the linear solution, velocities in the along-ridge direction have an amplitude of fU_0/ω and are therefore much smaller at 10° (figure 4.5) than at 50° (figure 4.6). In the f_{50° simulation, the quadrature phase relation between displacement and cross-ridge velocity is evident as large isopycnal displacements occur with a 6 hr lag behind cross-ridge flows. In agreement with the theory of Section 4.2, both along- and cross-ridge velocities are baroclinic away from topography. Time mean along-ridge

jets form along the flanks of the ridge and are most clearly visible at hours 0 and 12 of the snapshots, and are discussed in detail in the next section.

4.3.2.2 Phase averaged flows

Despite the small amplitudes of the tide in these simulations, nonlinear effects generate significant rectified along-ridge flows near the crest of the ridge whose magnitude increases with latitude. In the deep ocean, tidally rectified flows arise under the combined influence of a Stokes drift, associated with the Coriolis turning of a fluid parcel as it changes its water depth, and an Eulerian mean current (*Huthnance*, 1973; *Loder*, 1980). In the shallow water near the ridge crest, continuity and Coriolis turning cause the tidal ellipse to be larger than in deeper water. The tidal Stokes drift of the fluid arises as fluid parcels advected between deep and shallow water each tidal cycle experience asymmetric along-ridge flows, leading to a mean Stokes drift along the ridge (in the northern hemisphere the drift is with shallow water to the left). Dynamic considerations require an Eulerian mean flow such that fluid parcels experience no time mean drag, as in shallow water the depth mean frictional influence of the bottom boundary is larger than in deeper water. The Eulerian mean current is directed in the opposite sense to the Stokes drift such that along-ridge parcel velocity is enhanced in low friction (deeper) regions relative to high friction (shallower) regions. The resulting mean Lagrangian current is in the same sense as the Eulerian current (shallow water to the right, in the northern hemisphere), but has a magnitude that is smaller by the mean Stokes velocity. The generation of these flows has been studied for a stratified fluid over small amplitude topography in some detail (*Maas and Zimmerman* (1989a) and *Maas and Zimmerman* (1989b), hereafter MZ88a and MZ88b respectively). MZ88b find that stratification causes the rectified flows to be bottom trapped, and associated with Eulerian mean cross-isobath circulations. In this section we illustrate these flows in our simulations from both the Eulerian and Lagrangian reference frame and find good qualitative agreement between the small amplitude topography theory presented in MZ88b, and the rectified flows occurring in these finite amplitude topography simulations.

Eulerian time-mean along-ridge currents (color), $x-z$ streamfunction (grey contours) and isopycnal displacements (black contours) from the analysis period for the simulations at f_{10° and f_{50° are shown in figure 4.7 a) and b). The Eulerian mean streamfunction is computed by integrating the time mean cross-ridge component in z, with the integration constant set to ensure continuity over the ridge. In all simulations a mean flow develops that is predominantly composed of a pair of along-ridge jets with anticyclonic vertical vorticity at the ridge crest, with a general trend that the jets become faster as latitude increases (Figure 4.7 c). Peak jet speeds in the f_{50° simulation are in excess of $3U_0$ and are located at around the depth of the crest of the topography (note that at this latitude the oscillatory along-ridge response has a magnitude of $fU_0/\omega = 1.5U_0$). As predicted in MZ88b, these Eulerian time-means exhibit secondary circulations in the $x-z$ plane: jet-centered cells with peak downwards velocities of around $0.25U_0$ at the crest, and weaker upward velocities near the outside of each of the jets. The phase mean along-ridge jets in the f_{10° simulation are weaker and extend further in the horizontal.

We compute the Eulerian mean momentum balance by performing a Reynolds decomposition of the fields such that they are composed of three parts: an Eulerian phase averaged component (angle brackets), the oscillatory baroclinic response component (primes), and, in the case of the cross-ridge velocity, the spatially uniform background tide (u_b):

$$\begin{gathered} u = \langle u \rangle + u' + u_b \quad ; \quad v = \langle v \rangle + v' \quad ; \quad w = \langle w \rangle + w' \\ p = \langle p \rangle + p' \quad ; \quad b = \langle b \rangle + b'. \end{gathered} \tag{4.33}$$

These expressions are substituted into the nonlinear equations of motion, and

averaged over one tidal period:

$$\begin{aligned}
\langle u\rangle_t + \langle p\rangle_x - f\langle v\rangle - \nu\nabla^2\langle u\rangle &= -(\langle u_b u'\rangle_x + \langle u'u'\rangle_x + \langle w'u'\rangle_z + \langle u\rangle\langle u\rangle_x + \langle w\rangle\langle u\rangle_z)\\
\langle v\rangle_t + f\langle u\rangle - \nu\nabla^2\langle v\rangle &= -(\langle u_b v'\rangle_x + \langle u'v'\rangle_x + \langle w'v'\rangle_z + \langle u\rangle\langle v\rangle_x + \langle w\rangle\langle v\rangle_z)\\
\langle w\rangle_t + \langle p\rangle_z - \langle b\rangle - \nu\nabla^2\langle w\rangle &= -(\langle u_b w'\rangle_x + \langle u'w'\rangle_x + \langle w'w'\rangle_z + \langle u\rangle\langle w\rangle_x + \langle w\rangle\langle w\rangle_z)\\
\langle b\rangle_t + N^2\langle w\rangle - \kappa\nabla^2\langle b\rangle &= -(\langle u_b b'\rangle_x + \langle u'b'\rangle_x + \langle w'b'\rangle_z + \langle u\rangle\langle b\rangle_x + \langle w\rangle\langle b\rangle_z)\\
\langle u\rangle_x + \langle w\rangle_z &= 0.
\end{aligned} \tag{4.34}$$

The advective terms are grouped on the right hand side of the equations, and represent forcing terms for the Eulerian mean fields. Three types of nonlinear interaction can give rise to a momentum flux into the Eulerian mean: a) self interaction of the primed fields (Reynolds stresses), b) self interaction of the mean fields, and c) interaction of the barotropic tide with the primed fields. Terms making up the momentum and buoyancy budgets were computed at the beginning of the 5th period for the double resolution simulation at f_{50° in a region close to the crest of the ridge. The across-ridge momentum and buoyancy budgets and are shown in Figure 4.8, where the top panels show the dominant terms and budget residual. All the nonlinear terms are included in $\langle Du/Dt\rangle$ and $\langle Db/Dt\rangle$, respectively.

Consistent with the expected balance for tidally rectified flows (e.g. *Loder* (1980)), the across-ridge (x) momentum balance for the Eulerian mean flow is predominantly in geostrophic balance (figure 4.8 a)i. pale blue dashed, and grey solid lines), with a residual supported by nonlinear terms. The terms corresponding to the rate of change of the mean cross-ridge flow and viscous diffusion of mean x-momentum were found to be negligibly small compared to the other terms and are not shown. The nonlinear terms are broken down in panels ii. and iii., and show that the dominant contribution comes from Reynolds stresses, shown in figure 4.8 a)ii.

Terms in the Eulerian buoyancy budget are shown in figure 4.8 b). Panel i. illustrates the balance between nonlinear terms and the Eulerian vertical velocity. Once again, the time derivative and diabatic terms are small compared to the others and are not shown. The smallness of the diffusive term confirms that despite

the relatively large Eulerian vertical velocities, fluid parcels do not cross isopycnals in the time mean, underscoring the importance of a Lagrangian frame of reference when considering time mean fluid motion in oscillatory flows. Eulerian mean vertical velocities are mainly supported by Reynolds stresses (figure 4.8 b)ii.), and to a lesser extent by interactions of the Eulerian mean fields (figure 4.8 b)iii.).

Whilst the diabatic and unsteady terms are negligibly small in the across-ridge momentum and buoyancy budgets, they are small but nonzero in the along-ridge (y) momentum balance (not shown), indicating that the jets are slowly accelerating at the time that the budget was diagnosed. Mixing results in a volume of intermediate density fluid close to the crest of the ridge that slowly increases over the course of the simulation (see Section 4.3.3). *Chen and Beardsley* (1995) found similar processes to be occurring in their simulations of stratified tidal flow over a shallow 2D ridge where it generated a tidal mixing front, which, through Rossby adjustment, became associated with a frontal jet. The generation of mixed fluid in our simulations provides a small but steadily increasing contribution to the rectified flows generated by Coriolis turning and friction.

Individual particle trajectories were computed over one period for the flow as a post processing step by integrating the 10 minute output fields using a Runge-Kutta fourth order scheme. Paths are dependent on the phase of the tide at which the particles were seeded, and figure 4.9 shows nine paths initiated at slack tide before eastward flow. Particles close to the crest exhibit looping trajectories along the ridge, as they move under the combined influence of Stokes drift and the Eulerian mean flow, spending less time in shallower water (higher friction) than in deeper water (lower friction) such that they experience no net drag. Short wavelength oscillations are apparent in some tracks as particles pass through nonlinear lee waves. Further away from the crest, particles exhibit tracks that are much more elliptical, and close to those expected from the zero-order linear solution.

4.3.2.3 Energetics

Tidal averages of kinetic and available potential energies in the region above the topography are shown in figure 4.10. The finite width of the model ridge makes

a precise comparison to theory impossible, as such we present the spatial average in a region 2 km wide and centered at the crest of the ridge. For comparison with the theoretical results shown in figure 4.3, the kinetic energy is computed from only the velocity field arising from the presence of the topography, i.e. with the time-dependent but spatially constant background tide, u_b, removed.

Consistent with theory, average ridge-crest energy is approximately constant below the turning latitude, but increases with latitude where the barotropic tide is subinertial. Where the tide is superinertial, the radiated wave field has a constant energy density as the distance from the ridge crest increases, and compares well to the energy densities predicted by theory. However, when the tide is subinertial the response decays exponentially away from topography, and in this case the spatial average causes the measured energy density to be much smaller than that predicted for the knife-edge ridge.

Kinetic and potential energies associated with the Eulerian time mean flow are shown in thin lines in figure 4.10. Even though the phase averaged flows have velocities comparable to the tidal amplitude, they constitute much less energy than their time dependent counterparts due to their limited spatial extent. Their energy tends to increase with latitude up to 70° and is roughly constant above that (figure 4.7).

4.3.3 Long excursion length simulations

Nearfield mixing can arise through both breaking tidal lee waves and transient hydraulic jumps (*Musgrave et al.*, 2015b), influencing the overall tide- topography energy budget by dissipating energy in the nearfield, and reducing the radiated internal wave flux (*Klymak et al.*, 2010a; *Rapaka et al.*, 2013). In this section we present the results of two simulations having relatively long excursion lengths ($l_{exc} \approx l_{rdg}$), and contrast the development of nearfield mixing when the tide is subinertial, then superinertial. The tidal amplitudes of these flows are $0.02\,\mathrm{ms}^{-1}$, which is small, even in the deep ocean. Though the cross-ridge kinetic energy of the response is the same at all latitudes, the along-ridge kinetic energy and available potential energy depends on latitude. These simulations were per-

formed at latitudes of 3.85° and 44.7°, where theory predicts that the amplitude of the ridge-top buoyancy anomaly (potential energy) will be the same, enabling as close to an equivalent comparison as possible.

Snapshots of the flow at 6 hr intervals during the 5th period of the simulation are shown in figures 4.11 (superinertial) and 4.12 (subinertial). As in the small excursion length simulations, the superinertial tide generates radiating energy at the fundamental frequency and its harmonics which forms beams at characteristic slopes emanating from the topographic crest. Close to the crest, the wavefield constructively superposes during peak cross-ridge flow to form tidal lee waves: time dependent beam-like features that have slopes that change with the tide as the composite frequencies disperse (*Bell*, 1975; *Musgrave et al.*, 2015b). The subinertial simulation has some energy at harmonics, but the response at the fundamental frequency is trapped and associated with large amplitude along-ridge flows. The quadrature phase relation between ridge-top flow and isopycnals is more obvious in these large-amplitude simulations, with the subinertial simulation having large isopycnal displacements during slack tide (hours 6 and 18). In hours 0 and 12, isopycnals very close to the crest of the ridge on its upstream side exhibit vertical displacements that are not predicted by the linear theory in Section 4.2, and are associated with the phase averaged jets.

Area integrated dissipation rates within ±4 km of the ridge crest are presented for each simulation during the 5th period in Figure 4.13a. In these two-dimensional simulations, computed dissipation rates do not represent the dissipation associated with fully turbulent, three-dimensional flows at high Reynolds number. Nevertheless, their relative values and timings provide insight on which of the two simulations are more dissipative, and when during the tidal cycle the dissipation occurs. Dissipation rates take larger values and peak later in the tidal cycle for the subinertial simulation compared to the superinertial simulation. In the superinertial simulation tidal transport is in phase with isopycnal displacement at the ridge crest, and peak dissipation lags peak tidal flow by around an eighth of a period as dissipative processes in the hydraulic jump continue to grow even once the cross-ridge tidal transport starts to decrease. In the subinertial simulation

isopycnal displacement lags tidal transport by a quarter period at the ridge crest, and peak dissipation rates are both larger than in the superinertial simulation, and lag peak tidal flow by almost a quarter of a period, occurring significantly later in the tidal cycle than in the superinertial case. As the cross-ridge transport relaxes, the combination of upward moving isopycnals on the upstream side, and downward moving isopycnals on the lee side causes the near-bottom, hydraulically controlled jet to persist for longer, with the hydraulic jump developing in a region of relatively low stratification (associated with large isopycnal displacement) and generating a more dissipative hydraulic jump than in the superinertial case. In the latter situation, the relaxing tidal transport is associated with increasing downstream stratification.

We assess the vertical distribution of mixing in each simulation within the analysis domain (± 4 km of the ridge crest) by defining an evenly spaced set of temperature classes, then computing the volume of fluid occupied by each temperature class at the beginning of the simulation, and at 120 hr of the simulation. Figure 4.13b shows the volume of fluid occupied by each temperature class, nondimensionalized by its initial volume for both the sub- and superinertial simulations. Volumes different than one indicate that diabatic processes have mixed fluid into or out of that temperature class. Both simulations show distinct mixing peaks at depths of $\sim$500 m, corresponding to relatively weakly stratified fluid that develops close to the peak. Adjacent temperature classes occupy a reduced volume of fluid, resulting in relatively high stratifications surrounding the mixed fluid. The superinertial simulation has a second, smaller peak at around 430 m depth. The temperature classes which have grown (nondimensional volumes greater than one) are outlined in green contours in Figures 4.11 and 4.12. *Musgrave et al.* (2015b) distinguish between mixing arising from hydraulic jump like features which occur on the flanks of topography, and mixing arising from convective instability of the radiating lee wave component, which occurs at shallower depths - mainly above the ridge crest. The lack of a second, shallower peak in the subinertial simulation is consistent with the evanescent (non-radiating) fundamental frequency response, and consequently a much smaller radiating component than in the superinertial

case. The dominant mixing mechanism here is a transient hydraulic jump of the bottom trapped cross-ridge jet, forming on the flanks of the ridge each tidal cycle. In the superinertial simulation, the constructive interference of the fundamental and harmonic responses is of large enough amplitude to generate breaking and mixing in a radiating tidal lee wave, forming a second, smaller peak in mixing above the top of the ridge. It is notable that the subinertial simulation is more dissipative, despite the relative contribution from the radiating component being much smaller in this case.

4.4 Trapped internal tides in three-dimensions

The distinctly different nature of the evanescent compared to the radiating response results in changes not only to the magnitude and spatial distribution of tidal energy near topography, but also the timing, structure and evolution of nearfield tidally driven mixing. In addition, nonlinear effects generate fast along-ridge time mean currents, even when tidal amplitudes are small. A natural question that arises is to what extent these idealized two-dimensional results apply in a more general three-dimensional setting, and whether additional phenomena may become important.

Our imposition of two-dimensional solutions excludes *a priori* features with along-ridge variation, including trapped topographic waves, which have been observed at several high latitude locations (*Padman et al.*, 1992; *Kunze and Toole*, 1997). The structure of these trapped waves can be determined for specific topographies and stratifications by numerically solving an eigenvalue problem whose eigenmodes correspond to the resonant modes of the topography (*Huthnance*, 1978; *Brink*, 1989; *Codiga*, 1997). Trapped modes have discrete subinertial frequencies, and propagate anticyclonically around bathymetry. When the eigenfrequencies of the trapped modes are close to that of a tidal constituent, trapped tides at that frequency may be resonantly excited, generating relatively large amplitude tidal currents close to the topography (*Chapman*, 1989). Unlike the two-dimensional forced solutions discussed in this paper, the eigenmodes corresponding to trapped

tides are constructed such that they individually satisfy a boundary condition of no-flow through the boundary. Conversely, in the forced tidal problem, solutions are required to add to the background tide such that there is no flow through the boundary, which means that the solutions themselves have a component perpendicular to the boundary. Despite this distinction, we note that in the subinertial solution, the phase relation between displacement and along-ridge flow is consistent with propagation along the ridge (if along-ridge variation was allowed). As a result, the forced response described in this paper will resonantly excite the trapped eigenmodes of the topography if the topographic length scales and ambient stratification are such that the eigenfrequencies of the topography are close to the forcing frequency. The potential for this resonance suggests a much higher sensitivity of three-dimensional topographic features to subinertial than to superinertial tidal constituents.

Even in the absence of a resonance between the forced response and the eigenmodes of the topography, we expect that the characteristics of the subinertial forced solutions described here are relevant in three-dimensions, generating strong along-ridge flows that are phase locked with the background tide and having displacements and velocities that increase, and off-ridge length scales that decrease at higher latitudes.

4.5 Discussion and Conclusions

In this paper we have examined the two dimensional response of a stratified ocean to subinertial tidal forcing, and contrasted it to the relatively well-studied response to superinertial tidal forcing. Analytic solutions for a tall, infinitely thin barrier predict a latitudinal increase in the energy density at the ridge-crest when the tide is subinertial, arising from large along-ridge flows and isopycnal displacements. This is confirmed in a series of numerical simulations, which additionally illustrate the distinctive evanescent nature of the response. The elevated energy density of near ridge subinertial tidal flows may strongly influence regional mixing at high latitudes, affecting critical climate processes including ice melt and

ocean-atmosphere heat exchange.

All simulations with $f \neq 0$ generate along-ridge rectified currents, demonstrating the importance of nonlinearity in these flows. The speed of the Eulerian mean currents increase with latitude, with peak speeds reaching $4u_0$ at latitudes of 80°, though the jet speeds continue to increase during our simulations. The time mean flows are primarily associated with the Coriolis mechanism described by *Huthnance* (1973), where gradients in frictional drag associated with depth changes cause fluid parcels to acquire relative vorticity each tidal cycle. Additional routes for nearfield dissipation may be associated with these currents in three-dimensions, either by interaction with along-bathymetric features which could lead to along-ridge hydraulic processes, or even via the generation of Kelvin-Helmholtz type instabilities. Using the Eulerian mean field at f_{50°, and with $N = 1\,\mathrm{cph}$, we estimate a vertical shear of $\sim 9 \times 10^{-4}\,\mathrm{s}^{-1}$, which results in a Richardson number of around 3.7. However, the influence of nearfield mixing on locally reducing stratification, combined with time-dependent changes in shear and stratification has the potential to reduce the Richardson number during some phases of the tide such that instabilities in the along-ridge may play an important role. In addition, the Lagrangian transport associated with these jets may be important for high latitude coastal processes, transporting and mixing water masses across the shelf-break and providing a pathway for the regional transport of tracers and biological material (*Flexas et al.*, 2015).

A pair of simulations with larger amplitude tides ($0.02\,\mathrm{ms}^{-1}$) at latitudes that are superinertial and subinertial for the 24 hr tide show that, like for like, the subinertial simulation is relatively more dissipative, with the dissipation occurring around an eighth of a period later in the tidal cycle than in the superinertial case due to the influence of the time-dependent downstream stratification on the developing hydraulic jump. The vertical distribution of mixing in both simulations is similar, though the superinertial simulation has more mixing higher in the water column, associated with the radiating lee wave response. In both simulations, most of the mixing occurs on the near-crest flanks of the ridge, and is associated with hydraulic control of a bottom intensified cross-ridge jet.

In the ocean, the generation of subinertial topographically trapped waves via a resonance between the tide and the eigenfrequencies of the topography may result in large velocities and isopycnal displacements close to topography, and consequently lead to significantly more nearfield dissipation and mixing than when the tide is superinertial. As a result, parametrizing the dissipation of subinertial tidal constituents may prove more complicated than their superinertial counterparts.

4.6 Acknowledgements

We thank Nicolas Grisourd for helpful discussions relating to this work, and Maxim Nikurashin for help setting up the numerical model. Computing was performed on the Yellowstone Supercomputer, NSF award number ANT-0961218. RCM is funded by the Office of Naval Research and the National Science Foundation.

Chapter 4, in full, has been submitted for publication of the material as it may appear in the Journal of Fluid Mechanics, 2015, Musgrave, R C; Pinkel, R; MacKinnon, J A; Mazloff, M; Young, W R. The dissertation author was the primary investigator and author of this paper.

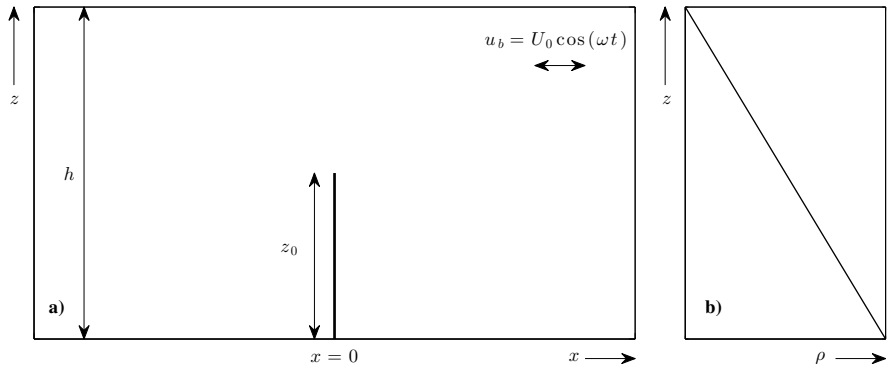

Figure 4.1: Definition sketch. a) The barotropic tide oscillates over a tall, narrow ridge. b) Density, ρ, increases uniformly with depth.

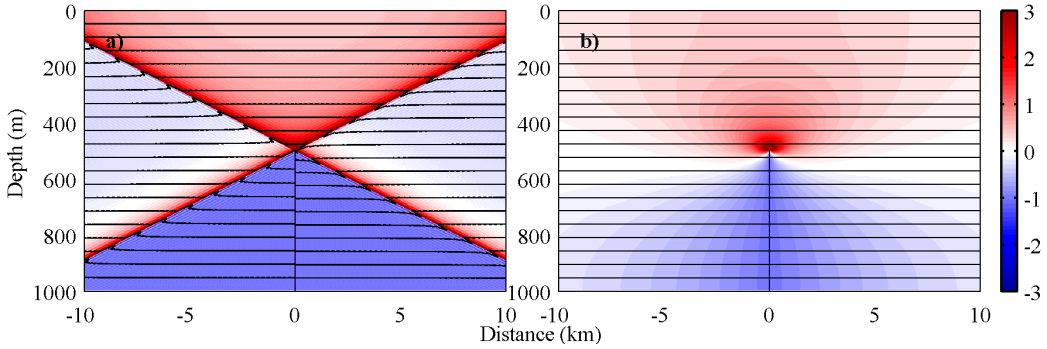

Figure 4.2: Horizontal velocities nondimensionalized by U_0 (color) and isopycnals (contours) at $t = 0$ for the superinertial (a) and subinertial (b) solutions.

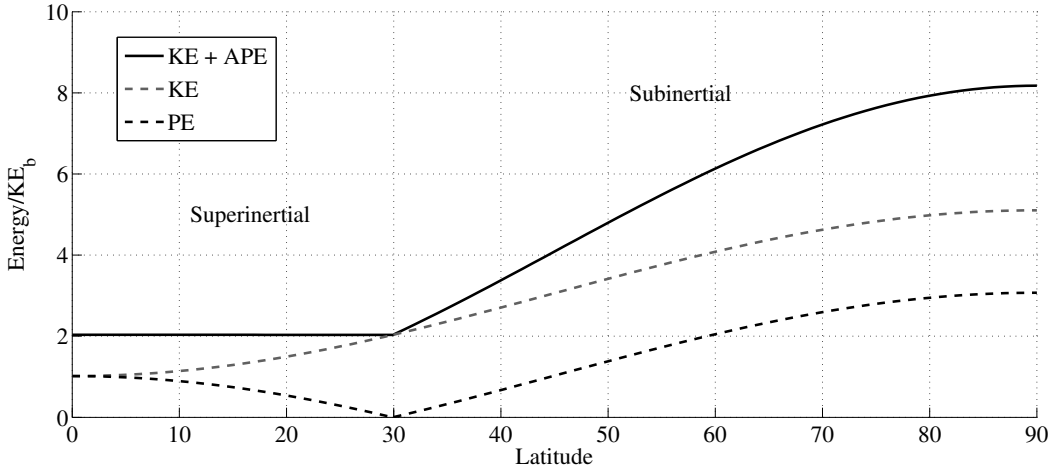

Figure 4.3: Depth and time averaged kinetic and available potential energies at $x = 0$ as a function of latitude, from theory.

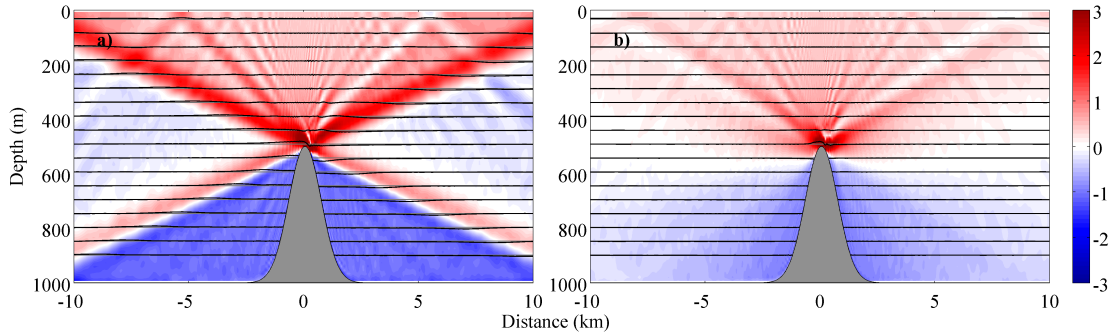

Figure 4.4: Widefield snapshots of u, with isopycnals contoured, for small excursion length simulation at a) f_{10}, where the fundamental frequency response is radiating, and b) f_{50} where the fundamental frequency response is evanescent. Spatially constant background tide, u_b, has been removed. Nondimensionalized by U_0.

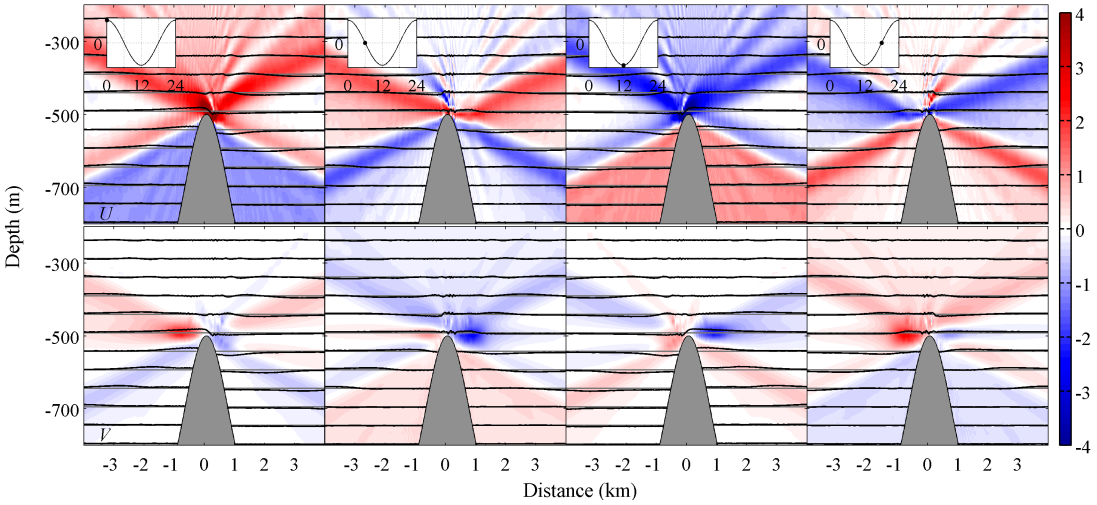

Figure 4.5: Snapshots of u (upper panel) and v (lower panel) with isopycnals (contoured) for small excursion length simulation at f_{10}, where the fundamental frequency response is radiating. Background tide, u_b, has been removed. Nondimensionalized by U_0.

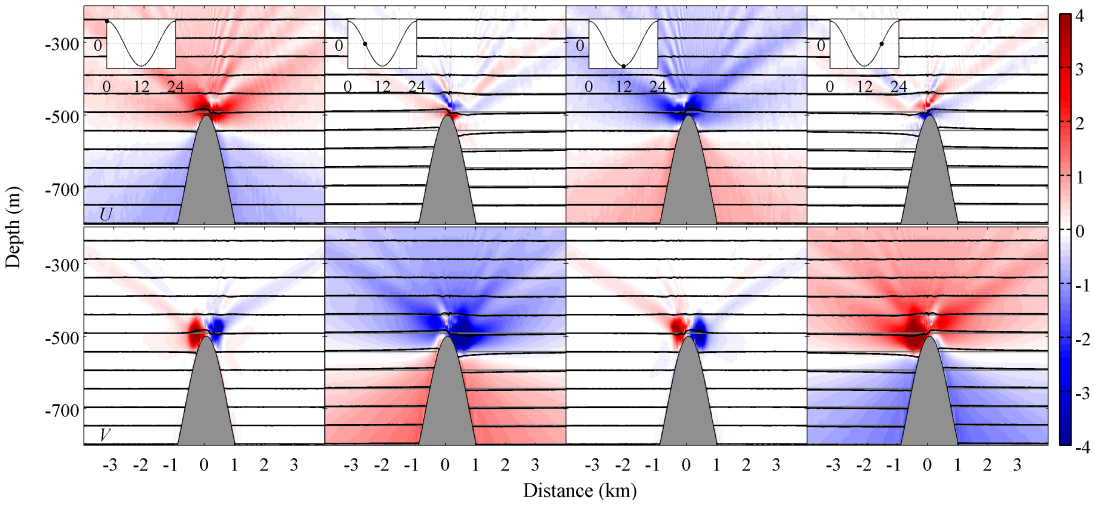

Figure 4.6: Snapshots of u (upper panel) and v (lower panel) with isopycnals (contoured) for small excursion length simulation at f_{50}, where the fundamental frequency response is evanescent. Background tide, u_b, has been removed. Nondimensionalized by U_0.

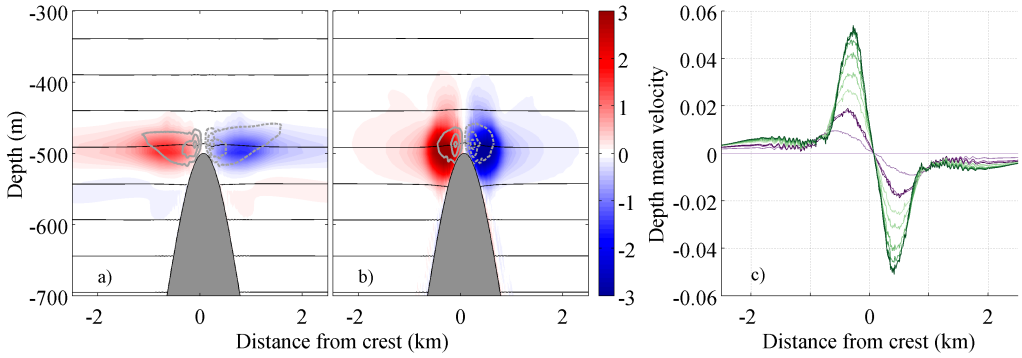

Figure 4.7: Eulerian mean along-ridge velocities normalized by U_0 at a) f_{10°, and b) f_{50°. Grey contours are $x-z$ streamfunction. c) Depth mean along-ridge velocities from all small excursion length simulations. Higher latitudes are darker, with purples indicating superinertial latitudes, and greens indicating subinertial latitudes.

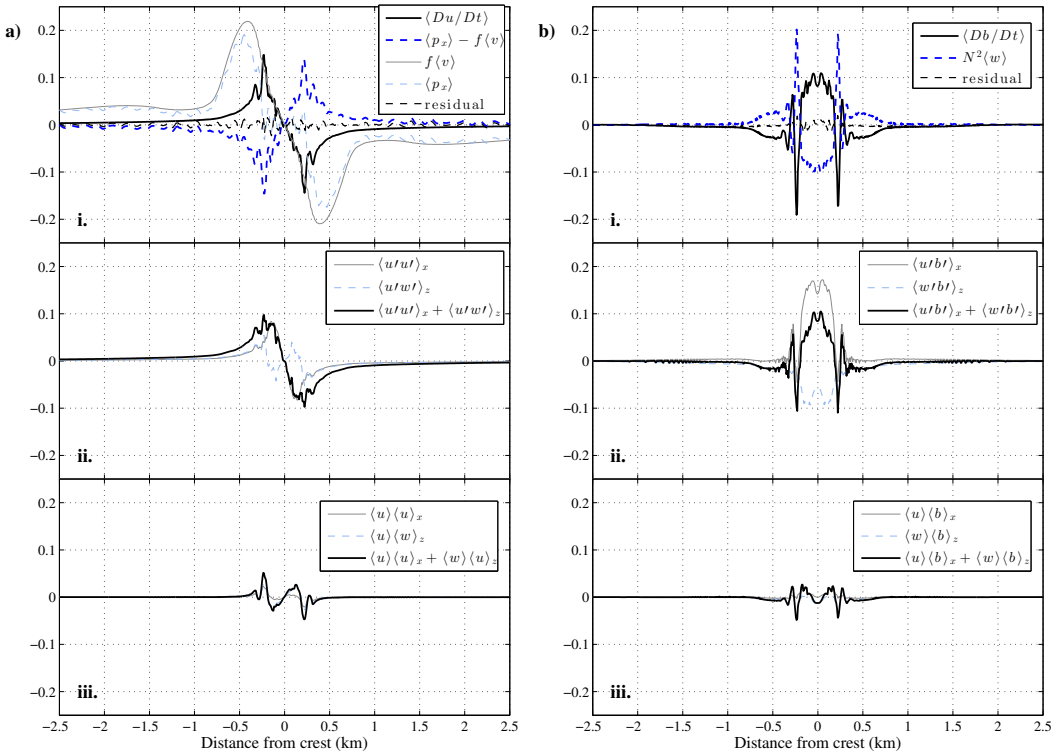

Figure 4.8: Depth mean near-ridge a) x-momentum budget (nondimensionalized by fU_0), and b) buoyancy budget (nondimensionalized by w_0N^2) for f_{50°. Thick lines in upper panels indicate the dominant balance in the equations. Lower panels break down the advective terms into perturbations and means.

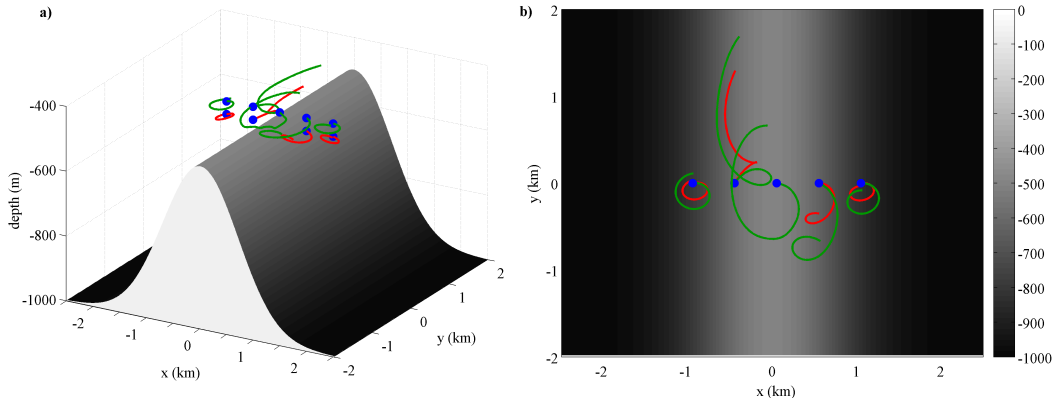

Figure 4.9: Particle trajectories over one period for 9 particles seeded at 120 hr in f_{50° simulation. Green tracks are for particles seeded at -480m , red tracks are particles seeded at -520 m. Blue dots indicate starting positions. a) Side view, b) plan view.

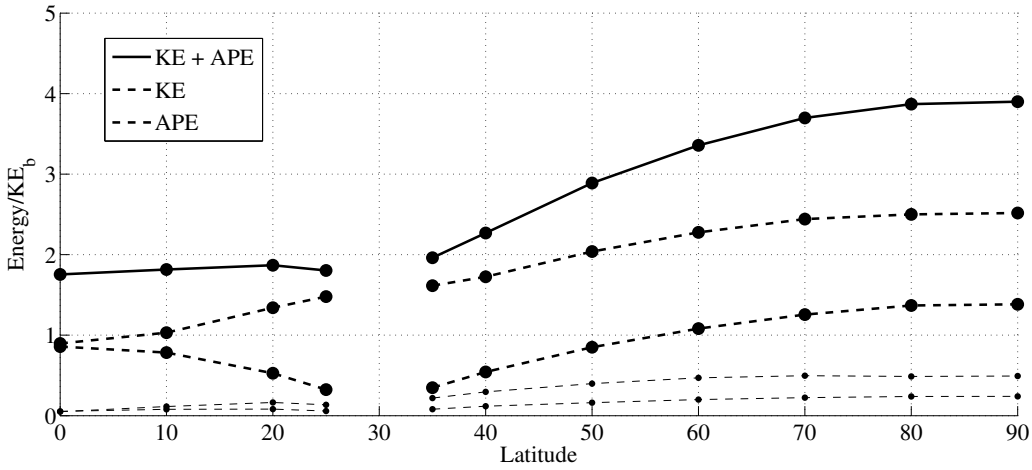

Figure 4.10: Thick lines: time mean kinetic (grey dashed), available potential (black dashed) and total energy averaged over 2km region at ridge crest. Thin lines: kinetic (grey dashed) and available potential (black dashed) energy in the time mean flow.

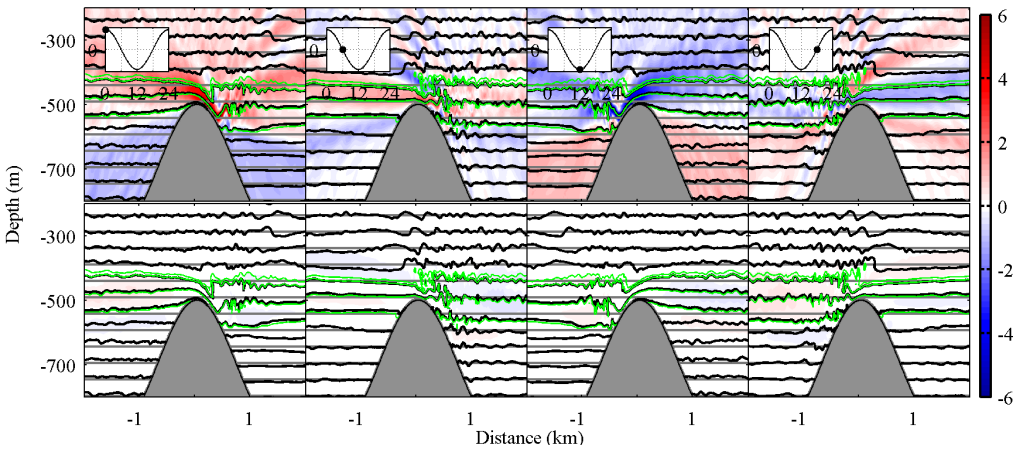

Figure 4.11: Snapshots of cross-ridge velocity, u (upper panel) and along-ridge velocity, v (lower panel) with isopycnals (contoured) for nonlinear simulation ($U_0 = 0.02$ ms^{-1}) at $f = 3.85°$, where the fundamental frequency response is radiating. Green contours indicate temperature classes which have increased in volume through mixing.

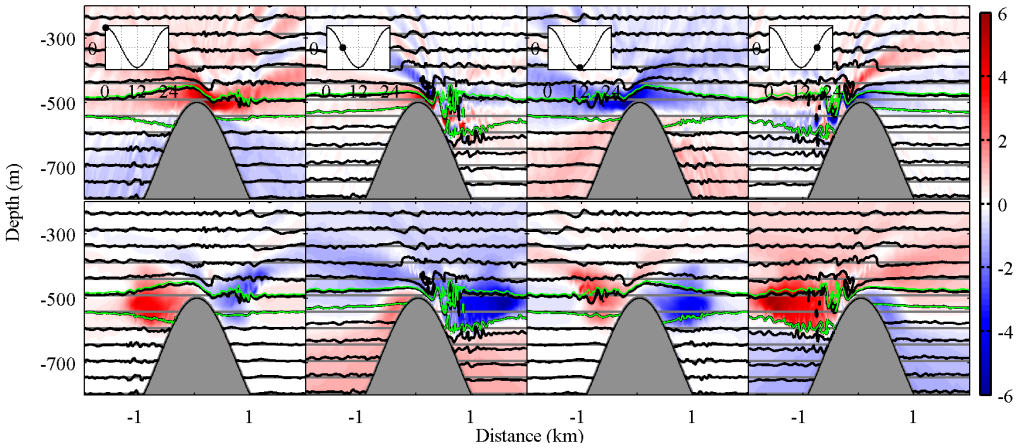

Figure 4.12: Snapshots of cross-ridge velocity, u (upper panel) and along-ridge velocity, v (lower panel) with isopycnals (contoured) for nonlinear simulation ($U_0 = 0.02$ ms^{-1}) at $f = 44.7°$, where the fundamental frequency response is evanescent. Green contours indicate temperature classes which have increased in volume through mixing.

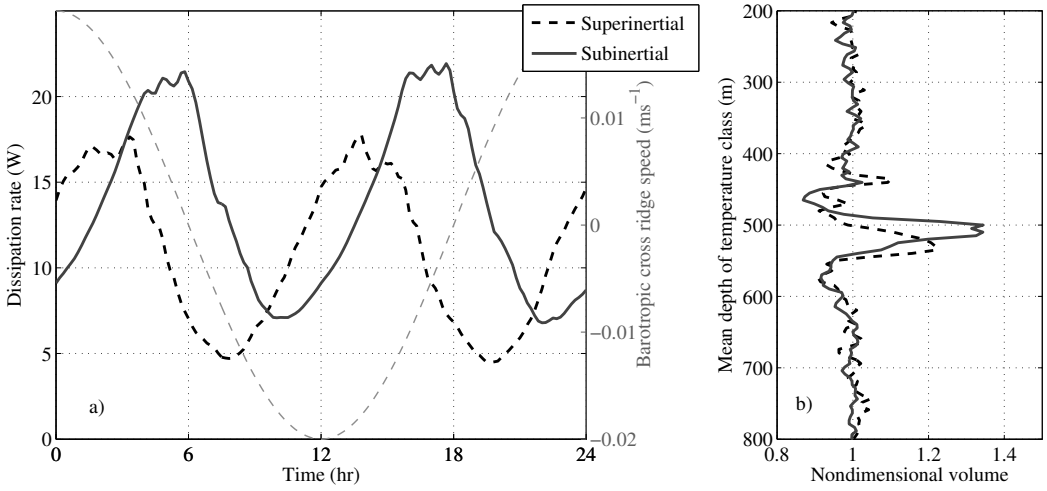

Figure 4.13: a) Integrated dissipation rate within ±4 km of the crest vs. time during 5th period. Thin dashed line is background tide, u_b. b) Volume of fluid occupied by given temperature class at 120 hr, nondimensionalized by volume occupied at 0 hr.

Appendix A: A shallow water analogy for internal tide generation at a vertical wall

Some intuition for the radiating and evanescent solutions can be gained by consideration of a much simpler system. Here we consider a semi-infinite ocean basin that is filled with unstratified fluid and has a vertical wall at $x = 0$. Far from the wall in the ocean interior, a single frequency rectilinear barotropic tide has the form $u = -U_0 \cos \omega t$. The equations of motion become

$$u_t - fv = -g\eta_x + U_0 \omega \sin \omega t \tag{4.35}$$

$$v_t + fu = -U_0 f \cos \omega t \tag{4.36}$$

$$u_x = -\frac{1}{H}\eta_t, \tag{4.37}$$

where the forcing terms mimic the astronomical potential, and in an infinite domain would provide a rectilinear, oscillatory flow in the x direction.

We define a background and perturbation current: $u = u_b + u'$, $v = v_b + v'$ with $u_b = -U_0 \cos \omega t$, $v_b = 0$, substitute into the above equations to obtain perturbation equations

$$u'_t - fv' = -g\eta_x \tag{4.38}$$

$$v'_t + fu' = 0 \tag{4.39}$$

$$u'_x = -\frac{1}{H}\eta_t, \tag{4.40}$$

which can be combined to form a single equation in u:

$$u'_{tt} + f^2 u' = Hgu'_{xx}. \tag{4.41}$$

If we assume solutions are wavelike, then $u' = \hat{u}e^{i(kx-\omega t)}$, and we obtain the Poincaré wave dispersion relation $\omega^2 - f^2 = gHk^2$.

The wall at $x = 0$ imposes a boundary condition that $u = u_b + u' = 0$ at $x = 0$, which means $u'(x = 0) = \hat{u}e^{-i\omega t} = U_0 \cos \omega t$. We now consider the solutions when the tidal frequency is superinertial and subinertial.

Superinertial, $\omega > f$

In this case

$$k^2 = \frac{\omega^2 - f^2}{gH} \tag{4.42}$$

and k is real. Then the solutions are simply radiating Poincaré waves

$$u' = U_0 \cos(kx - \omega t) \tag{4.43}$$

$$v' = \frac{fU_0}{\omega} \sin(kx - \omega t) \tag{4.44}$$

$$\eta = \frac{HU_0 k}{\omega} \cos(kx - \omega t) \tag{4.45}$$

Subinertial, $\omega < f$

In this case it's convenient to define $k = ik_R$, where k_R is real:

$$k_R = \sqrt{-\frac{\omega^2 - f^2}{gH}}. \tag{4.46}$$

Now the solutions are evanescent

$$u' = U_0 e^{-k_R x} \cos \omega t \tag{4.47}$$

$$v' = -\frac{fU_0}{\omega} e^{-k_R x} \sin \omega t \tag{4.48}$$

$$\eta = \frac{k_R H U_0}{\omega} e^{-k_R x} \sin \omega t \tag{4.49}$$

Some observations

These simple, shallow water solutions illustrate the important characteristics of the more complex stratified case described in Section 4.2. In the super inertial case u' is in phase with the surface displacement whilst in the sub inertial

case the displacement lags by $\pi/2$. Near wall energetics display the same behavior with increasing latitude as a result of the increased energy associated with oscillatory along-ridge flows.

$$(\overline{\mathrm{KE}} + \overline{\mathrm{PE}})_{\omega>f} = \frac{1}{2}\rho H U_0^2 \tag{4.50}$$

$$(\overline{\mathrm{KE}} + \overline{\mathrm{PE}})_{\omega<f} = \frac{1}{2}\rho H U_0^2 \frac{f^2}{\omega^2}. \tag{4.51}$$

As expected for Poincaré waves, the amplitude of the surface displacement tends to zero and the horizontal wavelength to infinity as the forcing frequency approaches the turning latitude. Conversely, as $|\omega^2 - f^2|$ becomes large in either direction away from the turning latitude the horizontal wavelength becomes small, and the interface displacement amplitude large.

Appendix B: A formal expansion of the equations of motion in the Froude number and excursion length

In this section we present a perturbation expansion of the Navier-Stokes equations for this problem, and explicitly demonstrate the equivalence of the topographic Froude number and the excursion length in the knife-edge problem. We also show how mean flows and harmonics are generated at higher order. We start

with the fully nonlinear equations

$$\begin{aligned}
\frac{\partial u}{\partial t} + \mathbf{u}\cdot\nabla u - fv &= -p_x \\
\frac{\partial v}{\partial t} + \mathbf{u}\cdot\nabla v + fu &= 0 \\
\frac{\partial w}{\partial t} + \mathbf{u}\cdot\nabla w &= -p_z + b \\
\frac{\partial b}{\partial t} + \mathbf{u}\cdot\nabla b + wN^2 &= 0 \\
\nabla\cdot\mathbf{u} &= 0,
\end{aligned} \tag{4.52}$$

and nondimensionalize with U_0, the amplitude of the background tide; ω, its frequency; x_0, the length scale of the linear response; z_0, the height of the ridge; and N, the Brunt Väisälä frequency:

$$u = U_0\hat{u}; \quad t = \frac{\hat{t}}{\omega}; \quad f = \hat{f}\omega; \quad x = \hat{x}x_0; \quad z = \hat{z}z_0; \quad w = \hat{w}\frac{z_0U_0}{x_0}$$
$$p = \hat{p}U_0\omega x_0; \quad b = \hat{b}\frac{z_0U_0N^2}{x_0\omega}.$$

We have chosen to nondimensionalize buoyancy so that to leading order it is linear, rather than hydrostatic so that the role of the topographic Froude number will be made clear. The equations become

$$\begin{aligned}
\frac{\partial u}{\partial t} + \varepsilon\mathbf{u}\cdot\nabla u - fv &= -p_x \\
\frac{\partial v}{\partial t} + \varepsilon\mathbf{u}\cdot\nabla v + fu &= 0 \\
\frac{\partial w}{\partial t} + \varepsilon\mathbf{u}\cdot\nabla w &= \frac{x_0^2}{z_0^2}\left(-p_z + Fr^{-2}\varepsilon^2 b\right) \\
\frac{\partial b}{\partial t} + \varepsilon\mathbf{u}\cdot\nabla b + w &= 0 \\
\nabla\cdot\mathbf{u} &= 0,
\end{aligned} \tag{4.53}$$

Where $\varepsilon = U_0/(\omega x_0)$ is the nondimensional particle excursion length and $Fr = U_0/(Nz_0)$ is the topographic Froude number. If x_0^2/z_0^2 is large, then for hydrostatic balance,

$$Fr \approx \varepsilon, \tag{4.54}$$

which is consistent for the small excursion length, small Froude number flows under consideration.

We perform a perturbation expansion in terms of ε (or equivalently Fr), setting $u = u_0 + \varepsilon u_1 + \varepsilon^2 u_2 + ...$, and other variables similarly. We explicitly show expansions of the first few orders below.

Order ε^0

$$\begin{aligned} \frac{\partial u_0}{\partial t} - f v_0 + p_{0x} &= 0 \\ \frac{\partial v_0}{\partial t} + f u_0 &= 0 \\ p_{0z} + b_0 &= 0 \\ \frac{\partial b_0}{\partial t} + w_0 &= 0 \\ \nabla \cdot \mathbf{u_0} &= 0, \end{aligned} \tag{4.55}$$

These are the equations solved in section 4.2. To leading order, solutions have the form $e^{\pm i\omega t}$. Time averaged equations at this order are zero.

Order ε^1

$$\begin{aligned} \frac{\partial u_1}{\partial t} - f v_1 + p_{1x} &= -u_0 u_{0x} - w_0 u_{0z} \\ \frac{\partial v_1}{\partial t} + f u_1 &= -u_0 v_{0x} - w_0 v_{0z} \\ p_{1z} + b_1 &= 0 \\ \frac{\partial b_1}{\partial t} + w_1 &= -u_0 b_{0x} - w_0 b_{0z} \\ \nabla \cdot \mathbf{u_1} &= 0, \end{aligned} \tag{4.56}$$

This is the lowest order that first harmonic and time mean solutions are generated, as the equations are forced by terms having the form e^0, or $e^{\pm 2i\omega t}$.

Order ε^2

$$\begin{aligned} \frac{\partial u_2}{\partial t} - f v_2 + p_{2x} &= -u_1 u_{0x} - w_1 u_{0z} - u_0 u_{1x} - w_0 u_{1z} \\ \frac{\partial v_2}{\partial t} + f u_2 &= -u_1 v_{0x} - w_1 v_{0z} - u_0 v_{1x} - w_0 v_{1z} \\ p_{2z} + b_2 &= 0 \\ \frac{\partial b_2}{\partial t} + w_2 &= -u_1 b_{0x} - w_1 b_{0z} - u_0 b_{1x} - w_0 b_{1z} \\ \nabla \cdot \mathbf{u_2} &= 0, \end{aligned} \tag{4.57}$$

At this order solutions have the form $e^{\pm 3i\omega t}$, and, as at ε^0, time averaged equations are zero.

Chapter 5

Bibliography

Abe, S. and Nakamura, T. (2012). Processes of Breaking of Large-Amplitude Unsteady Lee Waves Leading to Turbulence. *Journal of Geophysical Research*.

Alford, M. H. (2010). Sustained, Full-Water-Column Observations of Internal Waves and Mixing near Mendocino Escarpment. *Journal of Physical Oceanography*, 40(12):2643–2660.

Alford, M. H., MacKinnon, J. A., Nash, J. D., Simmons, H. L., Pickering, A., Klymak, J., Pinkel, R., Sun, O., Rainville, L., Musgrave, R. C., Beitzel, T., Fu, K., and Lu, C. (2011). Energy Flux and Dissipation in Luzon Strait: Two Tales of Two Ridges. *Journal of Physical Oceanography*, 41(11):2211–2222.

Alford, M. H., Peacock, T., MacKinnon, J. A., Nash, J. D., Buijsman, M. C., Centuroni, L. R., Chao, S.-Y., Chang, M.-H., Farmer, D. M., Fringer, O. B., Fu, K.-H., Gallacher, P. C., Graber, H. C., Helfrich, K. R., Jachec, S. M., Jackson, C. R., Klymak, J. M., Ko, D. S., Jan, S., Johnston, T. M. S., Legg, S., Lee, I.-H., Lien, R. C., Mercier, M. J., Moum, J. N., Musgrave, R. C., Park, J.-H., Pickering, A. I., Pinkel, R., Rainville, L., Ramp, S. R., Rudnick, D. L., Sarkar, S., Scotti, A., Simmons, H. L., St Laurent, L. C., Venayagamoorthy, S. W., Wang, Y.-H., Wang, J., Yang, Y. J., Paluszkiewicz, T., and David Tang, T.-Y. (2015). The formation and fate of internal waves in the South China Sea. *Nature*, 521(7550):65–69.

Althaus, A., Kunze, E., and Sanford, T. B. (2003). Internal tide radiation from Mendocino Escarpment. *Journal of Physical Oceanography*, 33:1510–1527.

Baines, P. G. (1982). On internal tide generation models. *Deep Sea Research Part A. Oceanographic Research Papers*, 29(3):307–338.

Baines, P. G. and Hoinka, K. (1985). Stratified flow over two-dimensional topography in fluid of infinite depth: A laboratory simulation. *Journal of Atmospheric Sciences*, 42(15):1614–1630.

Balmforth, N. J. and Peacock, T. (2009). Tidal Conversion by Supercritical Topography. *Journal of Physical Oceanography*, 39(8):1965–1974.

Bell, T. H. (1975). Lee waves in stratified flows with simple harmonic time dependence. *Journal of Fluid Mechanics*, 67(4):705–722.

Brink, K. H. (1989). The effect of stratification on seamount-trapped waves. *Deep Sea Research Part A. Oceanographic Research Papers*, 36(6):825–844.

Brink, K. H. (1990). On the generation of seamount-trapped waves. *Deep Sea Research Part A. Oceanographic Research Papers*, 37(10):1569–1582.

Brink, K. H. (2011). Topographic rectification in a stratified ocean. *Journal of Marine Research*, 69:483–499.

Buijsman, M. C., Klymak, J. M., Legg, S., Alford, M. H., Farmer, D., MacKinnon, J. A., Nash, J. D., Park, J.-H., Pickering, A., and Simmons, H. L. (2013). Three-Dimensional Double-Ridge Internal Tide Resonance in Luzon Strait. *Journal of Physical Oceanography*, 44(3):850–869.

Cacchione, D., Pratson, L. F., and Ogston, A. S. (2002). The Shaping of Continental Slopes by Internal Tides. *Science*, 296:724–727.

Carter, G. S., Merrifield, M. A., Becker, J. M., Katsumata, K., Gregg, M. C., Luther, D. S., Levine, M. D., Boyd, T. J., and Firing, Y. L. (2008). Energetics of M2Barotropic-to-Baroclinic Tidal Conversion at the Hawaiian Islands. *Journal of Physical Oceanography*, 38(10):2205–2223.

Chapman, D. C. (1989). Enhanced subinertial diurnal tides over isolated topographic features. *Deep Sea Research Part A. Oceanographic Research Papers*, 36(6):815–824.

Chen, C. and Beardsley, R. C. (1995). A Numerical Study of Stratified Tidal Rectification over Finite-Amplitude Banks. Part 1: Symmetric Banks. *Journal of Physical Oceanography*, 25:2090–2110.

Christodoulidis, D. C., Smith, D. E., Williamson, R. G., and Klosko, S. M. (1988). Observed Tidal Braking in the Earth/Moon/Sun System. *Journal of Geophysical Research*, 93(B6):6216–6236.

Codiga, D. L. (1997). Physics and observational signatures of free, forced, and frictional stratified seamounttrapped waves. *Journal of Geophysical Research: Oceans (1978–2012)*, 102(C10):23009–23024.

Codiga, D. L. and Eriksen, C. C. (1997). Observations of lowfrequency circulation and amplified subinertial tidal currents at Cobb Seamount. *Journal of Geophysical Research: Oceans (1978–2012)*, 102(C10):22993–23007.

Cole, S. T., Rudnick, D. L., Hodges, B. A., and Martin, J. P. (2009). Observations of Tidal Internal Wave Beams at Kauai Channel, Hawaii. *Journal of Physical Oceanography*, 39(2):421–436.

Daru, V. and Tenaud, C. (2004). High order one-step monotonicity-preserving schemes for unsteady compressible flow calculations. *Journal of Computational Physics*, 193(2):563–594.

Di Lorenzo, E., Young, W. R., and Llewellyn Smith, S. G. (2006). Numerical and analytical estimates of M 2 tidal conversion at steep oceanic ridges. *Journal of Physical Oceanography*, 36(6):1072–1084.

Dillon, T. (1982). Vertical overturns: A comparison of Thorpe and Ozmidov length scales. *Journal of Geophysical Research*.

Egbert, G. and Erofeeva, S. Y. (2002). Efficient Inverse Modeling of Barotropic Ocean Tides. *Journal of Atmospheric and Oceanic Technology*, 19:183–204.

Egbert, G. and Ray, R. D. (2000). Significant dissipation of tidal energy in the deep ocean inferred from satellite altimiter data. *Nature*, 405:775–778.

Egbert, G. D. and Ray, R. D. (2003). Semi-diurnal and diurnal tidal dissipation from TOPEX/Poseidon altimetry. *Geophysical Research Letters*, 30(17).

Farmer, D. M. and Smith, J. D. (1980). Tidal interaction of stratified flow with a sill in Knight Inlet. *Deep Sea Research Part A. Oceanographic Research Papers*, 27(3-4):239–246, IN5–IN10, 247–254.

Flexas, M. M., Schodlok, M. P., Padman, L., Menemenlis, D., and Orsi, A. H. (2015). Role of tides on the formation of the Antarctic Slope Front at the Weddell-Scotia Confluence. *Journal of Geophysical Research: Oceans*, pages n/a–n/a.

Galbraith, P. S. and Kelley, D. E. (1995). Identifying Overturns in CTD Profiles. *Journal of Atmospheric and Oceanic Technology*, 13:688–702.

Gargett, A. E. and Garner, T. (2008). Determining Thorpe Scales from Ship-Lowered CTD Density Profiles. *Journal of Atmospheric and Oceanic Technology*, 25(9):1657–1670.

Gayen, B. and Sarkar, S. (2011). Direct and large-eddy simulations of internal tide generation at a near-critical slope. *Journal of Fluid Mechanics*, 681:48–79.

Gill, A. E. (1982). *Atmosphere-Ocean Dynamics*. Academic Press.

Green, J. A. M. and Nycander, J. (2013). A Comparison of Tidal Conversion Parameterizations for Tidal Models. *Journal of Physical Oceanography*, 43(1):104–119.

Hasumi, H. and Suginohara, N. (1999). Effects of locally enhanced vertical diffusivity over rough bathymetry on the world ocean circulation. *Journal of Geophysical Research*, 104(C10):23367–23374.

Hibiya, T., Nagasawa, M., and Niwa, Y. (2002). Nonlinear energy transfer within the oceanic internal wave spectrum at mid and high latitudes. *Journal of Geophysical Research*, 107(C11):28–1–28–8.

Huthnance, J. M. (1973). Tidal Current Asymmetries over the Norfolk Sandbanks. *Estuaries and Coastal Marine Science*, 1:89–99.

Huthnance, J. M. (1974). On the diurnal tidal currents over Rockall Bank. *Deep-Sea Research*, 21(1):23–35.

Huthnance, J. M. (1978). On coastal trapped waves: Analysis and numerical calculation by inverse iteration. *Journal of Physical Oceanography*, 8(1):74–92.

Ivey, G., Winters, K. B., and Koseff, J. (2008). Density stratification, turbulence, but how much mixing? *Annual Reviews of Fluid Mechanics*.

Jayne, S. R. (2009). The Impact of Abyssal Mixing Parameterizations in an Ocean General Circulation Model. *Journal of Physical Oceanography*, 39(7):1756–1775.

Jayne, S. R. and St Laurent, L. C. (2001). Parameterizing tidal dissipation over rough topography. *Geophysical Research Letters*, 28(5):811–814.

Johnston, T. M. S. and Merrifield, M. A. (2003). Internal tide scattering at the Line Islands Ridge. *Journal of Geophysical Research*, 108(C11):3365.

Kang, D. and Fringer, O. B. (2012). Energetics of Barotropic and Baroclinic Tides in the Monterey Bay Area. *Journal of Physical Oceanography*, 42(2):272–290.

Kelly, S. M., Jones, N. L., Nash, J. D., and Waterhouse, A. F. (2013). The geography of semidiurnal mode-1 internal-tide energy loss. *Geophysical Research Letters*, 40:1–5.

Kelly, S. M., Nash, J. D., and Kunze, E. (2010). Internal-tide energy over topography. *Journal of Geophysical Research*, 115(C6):C06014.

Khatiwala, S. (2003). Generation of internal tides in an ocean of finite depth: analytical and numerical calculations. *Deep-Sea Research Part I*, 50:1–19.

Klymak, J. and Legg, S. (2010). A simple mixing scheme for models that resolve breaking internal waves. *Ocean Modelling*, 33(3-4):224–234.

Klymak, J., Legg, S., Alford, M. H., Buijsman, M., Pinkel, R., and Nash, J. D. (2012). The Direct Breaking of Internal Waves at Steep Topography. *Oceanography*, 25(2):150–159.

Klymak, J., Legg, S., and Pinkel, R. (2010a). A simple parameterization of turbulent tidal mixing near supercritical topography. *Journal of Physical Oceanography*, 40:2059–2074.

Klymak, J., Legg, S., and Pinkel, R. (2010b). High-mode stationary waves in stratified flow over large obstacles. *Journal of Fluid Mechanics*, 644:321.

Klymak, J., Pinkel, R., and Rainville, L. (2008). Direct Breaking of the Internal Tide near Topography: Kaena Ridge, Hawaii. *Journal of Physical Oceanography*, 38(2):380–399.

Kunze, E. and Toole, J. M. (1997). Tidally Driven Vorticity, Diurnal Shear, and Turbulence atop Fieberling Seamount. *Journal of Physical Oceanography*, 27:2663–2693.

Legg, S. and Klymak, J. (2008). Internal Hydraulic Jumps and Overturning Generated by Tidal Flow over a Tall Steep Ridge. *Journal of Physical Oceanography*, 38(9):1949–1964.

Llewellyn Smith, S. G. and Young, W. R. (2002). Conversion of the barotropic tide. *Journal of Physical Oceanography*, 32:1554–1566.

Llewellyn Smith, S. G. and Young, W. R. (2003). Tidal conversion at a very steep ridge. *Journal of Fluid Mechanics*, 495:175–191.

Loder, J. W. (1980). Topographic Rectification of Tidal Currents on the Sides of Georges Bank. *Journal of Physical Oceanography*, 10:1399–1416.

Maas, L. R. M. and Zimmerman, J. T. F. (1989a). Tide-topography interactions in a stratified shelf sea. I. Basic equations for quasi-nonlinear internal tides. *Geophysical & Astrophysical Fluid Dynamics*, 45:1–36.

Maas, L. R. M. and Zimmerman, J. T. F. (1989b). Tide-topography interactions in a stratified shelf sea. II. Bottom trapped internal tides and baroclinic residual currents. *Geophysical & Astrophysical Fluid Dynamics*, 45:37–69.

MacKinnon, J. A. and Winters, K. B. (2005). Subtropical catastrophe: Significant loss of low-mode tidal energy at 28.9 °. *Geophysical Research Letters*, 32(15).

Marshall, J., Adcroft, A., Hill, C., Perelman, L., and Heisey, C. (1997). A finitevolume, incompressible Navier Stokes model for studies of the ocean on parallel computers. *Journal of Geophysical Research: Oceans (1978–2012)*, 102(C3):5753–5766.

Melet, A., Venayagamoorthy, S. W., Legg, S., and Polzin, K. L. (2013). Sensitivity of the Ocean State to the Vertical Distribution of Internal-Tide-Driven Mixing. *Journal of Physical Oceanography*, 43(3):602–615.

Müller, M. (2013). On the space-and time-dependence of barotropic-to-baroclinic tidal energy conversion. *Ocean Modelling*, 72:242–252.

Munk, W. H. (1966). Abyssal recipes I. *Deep Sea Research and Oceanographic Abstracts*, 13:707–730.

Munk, W. H. and Wunsch, C. (1998). Abyssal recipes II: energetics of tidal and wind mixing. *Deep-Sea Research*, pages 1977–2010.

Musgrave, R. C., MacKinnon, J. A., Pinkel, R., Waterhouse, A. F., and Nash, J. D. (2015a). The influence of diurnal trapped tides on near-ridge turbulence at the Mendocino Ridge: Observations and Modeling. *in prep*.

Musgrave, R. C., MacKinnon, J. A., Pinkel, R., Waterhouse, A. F., and Nash, J. D. (2015b). Tidally driven processes leading to nearfield turbulence in a channel at the crest of the Mendocino Escarpment. *Under review for Journal of Physical Oceanography*.

Musgrave, R. C., Mazloff, M., MacKinnon, J. A., and Pinkel, R. (2015c). Stratified tidal flow over a tall ridge above and below the turning latitude. *Under review for Journal of Fluid Mechanics*.

Nakamura, T., Isoda, Y., Mitsudera, H., Takagi, S., and Nagasawa, M. (2010). Breaking of unsteady lee waves generated by diurnal tides. *Geophysical Research Letters*, 37(L04602).

Nash, J. D., Alford, M. H., and Kunze, E. (2005). On Estimating Internal-Wave Energy Fluxes in the Ocean. *Journal of Atmospheric and Oceanic Technology*, 22(10):1551–1570.

Osafune, S. and Yasuda, I. (2013). Remote impacts of the 18.6 year period modulation of localized tidal mixing in the North Pacific. *Journal of Geophysical Research: Oceans*, 118:3128–3137.

Osborn, T. R. and Cox, C. S. (1972). Oceanic fine structure. *Geophysical & Astrophysical Fluid Dynamics*.

Padman, L., Plueddemann, A. J., Muench, R. D., and Pinkel, R. (1992). Diurnal Tides Near the Yermak Plateau. *Journal of Geophysical Research*, 97(C8):12639–12652.

Peltier, W. (1979). The Evolution and Stability of Finite Amplitude Mountain Waves. Part II- Surface Wave Drag and Severe Downslope Windstorms. *Journal of the Atmospheric Sciences*, 36:1498–1529.

Pétrélis, F., Llewellyn Smith, S. G., and Young, W. R. (2006). Tidal conversion at a submarine ridge. *Journal of Physical Oceanography*.

Phillips, O. M. (1971). On spectra measured in an undulating layered medium. *Journal of Physical Oceanography*, 1(1):1–6.

Platzman, G. W. (1991). An Observational Study of Energy Balance in the Atmospheric Lunar Tide. *Pure and Applied Geophysics*, 137(1-2):1–33.

Rapaka, N. R., Gayen, B., and Sarkar, S. (2013). Tidal conversion and turbulence at a model ridge: direct and large eddy simulations. *Journal of Fluid Mechanics*, 715:181–209.

Ray, R. D., Eanes, R. J., and Chao, B. F. (1996). Detecton of tidal dissipation in the solid Earth by satellite tracking and altimetry. *Nature*, 381:595–597.

Ray, R. D. and Mitchum, G. T. (1997). Surface manifestation of internal tides in the deep ocean: observations from altimetry and island guages. *Progress in Oceanography*, 40:135–162.

Rhines, P. B. (1970). Edge, bottom, and Rossby waves in a rotating stratified fluid. *Geophysical & Astrophysical Fluid Dynamics*, 1(3-4):273–302.

Sheen, K. L., Brearley, J. A., Naveira Garabato, A. C., Smeed, D. A., St Laurent, L. C., Meredith, M. P., Thurnherr, A. M., and Waterman, S. (2015). Modification of turbulent dissipation rates by a deep Southern Ocean eddy. *Geophysical Research Letters*, 42:1–8.

Simmons, H. L., Jayne, S. R., St Laurent, L. C., and Weaver, A. J. (2004). Tidally driven mixing in a numerical model of the ocean general circulation. *Ocean Modelling*, 6(3-4):245–263.

St Laurent, L. C., Simmons, H. L., and Jayne, S. R. (2002). Estimating tidally driven mixing in the deep ocean. *Geophysical Research Letters*, 29(23):2106.

Tanaka, T., Yasuda, I., Tanaka, Y., and Carter, G. S. (2013). Numerical study on tidal mixing along the shelf break in the Green Belt in the southeastern Bering Sea. *Journal of Geophysical Research: Oceans*, 118:6525–6542.

Taylor, G. I. (1919). Tidal friction in the Irish Sea. *Proceedings of the Royal Society of London. Series A. Mathematical and Physical Sciences*, 96:330.

Thorpe, S. A. (1977). Turbulence and mixing in a Scottish loch. *Philosophical Transactions for the Royal Society of London. Series A, Mathematical and Physical Sciences*, pages 125–181.

van Haren, H., Cimatoribus, A., and Gostiaux, L. (2015). Where large deep-ocean waves break. *Geophysical Research Letters*, 42:2351–2357.

Visbeck, M. (2002). Deep Velocity Profiling Using Lowered Acoustic Doppler Current Profilers: Bottom Track and Inverse Solutions. *Journal of Atmospheric and Oceanic Technology*, 19:794–807.

Waterhouse, A. F., MacKinnon, J. A., Nash, J. D., Alford, M. H., Kunze, E., Simmons, H. L., Polzin, K. L., St Laurent, L. C., Sun, O. M., Pinkel, R., Talley, L. D., Whalen, C. B., Huussen, T. N., Carter, G. S., Fer, I., Waterman, S., Naveira Garabato, A. C., Sanford, T. B., and Lee, C. M. (2014). Global Patterns of Diapycnal Mixing from Measurements of the Turbulent Dissipation Rate. *Journal of Physical Oceanography*, 44(7):1854–1872.

Winters, K. B. and Armi, L. (2012). Hydraulic control of continuously stratified flow over an obstacle. *Journal of Fluid Mechanics*, pages 1–12.

Winters, K. B. and Armi, L. (2013). The response of a continuously stratified fluid to an oscillating flow past an obstacle. *Journal of Fluid Mechanics*, 727:83–118.

Wunsch, C. and Ferrari, R. (2004). Vertical Mixing, Energy and the General Circulation of the Oceans. *Annual Reviews of Fluid Mechanics*, 36(1):281–314.

Zhang, Y. and Moum, J. N. (2010). Inertial-Convective Subrange Estimates of Thermal Variance Dissipation Rate from Moored Temperature Measurements. *Journal of Atmospheric and Oceanic Technology*, 27(11):1950–1959.

Zhao, Z. and Alford, M. H. (2009). New Altimetric Estimates of Mode-1 M2 Internal Tides in the Central North Pacific Ocean. *Journal of Physical Oceanography*, 39(7):1669–1684.